แบบจำลองพลาสมอนของคู่ทรงกลมนาโนที่อสมมาตร

นายรักชาติ กลิ่นกล้า

วิทยานิพนธ์นี้เป็นส่วนหนึ่งของการศึกษาตามหลักสูตรปริญญาวิทยาศาสตรดุษฎีบัณฑิต
สาขาวิชาฟิสิกส์ ภาควิชาฟิสิกส์
คณะวิทยาศาสตร์ จุฬาลงกรณ์มหาวิทยาลัย
ปีการศึกษา 2556

PLASMON MODEL OF AN ASYMMETRIC NANOSPHERE PAIR

Mr. Rakchat Klinkla

A Dissertation Submitted in Partial Fulfillment of the Requirements
for the Degree of Doctor of Philosophy Program in Physics
Department of Physics
Faculty of Science
Chulalongkorn University
Academic Year 2013

Thesis Title	PLASMON MODEL OF AN ASYMMETRIC NANOSPHERE PAIR
By	Mr. Rakchat Klinkla
Field of Study	Physics
Thesis Advisor	Associate Professor Udomsilp Pinsook, Ph.D.

Accepted by the Faculty of Science, Chulalongkorn University in Partial Fulfillment of the Requirements for the Doctoral Degree

..... Dean of the Faculty of Science
(Professor Supot Hannongbua, Dr.rer.nat.)

THESIS COMMITTEE

..... Chairman
(Associate Professor Mayuree Natenapit, Ph.D.)

..... Thesis Advisor
(Associate Professor Udomsilp Pinsook, Ph.D.)

..... Examiner
(Associate Professor Nakorn Phaisangittisakul, Ph.D.)

..... Examiner
(Assistant Professor Surachate Limkumnerd, Ph.D.)

..... External Examiner
(Sornthep Vannarat, Ph.D.)

รักชาติ กลิ่นกล้า : แบบจำลองพลาสมอนของคู่ทรงกลมนาโนที่อสมมาตร. (PLASMON MODEL OF AN ASYMMETRIC NANOSPHERE PAIR) อ.ที่ปรึกษาวิทยานิพนธ์หลัก : รศ.ดร.อุดมศิลป์ ปิ่นสุข, 80 หน้า.

การศึกษานี้มีวัตถุประสงค์เพื่อศึกษาผลของการเสียสมมาตรต่อเรโซแนนซ์ของพลาส-มอนพื้นผิวเฉพาะถิ่น (LSPR) ของคู่ทรงกลมนาโนในบริเวณที่มีอันตรกิริยารุนแรง โดยเริ่มจากศึกษาหลักเกณฑ์พื้นฐานของการเสียสมมาตรของขนาดอนุภาคและชนิดวัสดุของอนุภาคแยกกัน จากนั้นจึงศึกษาผลของการเสียสมมาตรทั้งสองอย่างพร้อมกัน พลังงานของ LSPR คำนวณโดยการหาผลเฉลยของสมการลาปลาซในระบบพิกัดแบบทรงกลมคู่ การใช้การคำนวณเชิงเมทริกซ์ทำให้ได้เงื่อนไขทั่วไปสำหรับการเกิดเรโซแนนซ์ของโหมดพื้นผิวในรูปแบบของปัญหาค่าไอเกนไม่เชิงเส้น รูปแบบนี้ทำให้ตีความการเกิด LSPR ในคู่ทรงกลมไม่สมมาตรได้ว่าเสมือนเป็นผลจากอันตรกิริยาของคู่ทรงกลมสมมาตรของอนุภาคที่เป็นองค์ประกอบในคู่ทรงกลมไม่สมมาตร พลังงาน LSPR ของคู่ทรงกลมนาโนได้ถูกคำนวณและการวิเคราะห์ลำดับของโหมดที่ถูกกระตุ้นได้ถูกบัญญัติขึ้น ผลของการคำนวณแสดงให้เห็นว่า ในกรณีที่คู่ทรงกลมเสียสมมาตรเนื่องจากชนิดของวัสดุ LSPR โหมดพลังงานต่ำสุดมีลักษณะเป็นโหมดเชื่อมต่อและมีพลังงานอยู่ระหว่างพลังงานของโหมดเชื่อมต่อของคู่ทรงกลมสมมาตรของอนุภาคองค์ประกอบ ขณะที่โหมดพลังงานต่ำสุดลำดับที่สองมีลักษณะแบบโหมดเชื่อมต่อในบริเวณที่อนุภาคมีระยะห่างระหว่างกันน้อยๆและมีลักษณะแบบโหมดต้านเชื่อมต่อในบริเวณที่อนุภาคมีระยะห่างระหว่างกันมากๆ โดยมีการเปลี่ยนคุณลักษณะของโหมดที่ระยะห่างค่าหนึ่งซึ่งถูกนิยามว่าเป็นจุดสลับโหมด ในกรณีที่คู่ทรงกลมเสียสมมาตรเนื่องจากขนาดของอนุภาค โหมดพลังงานต่ำสุดมีลักษณะเป็นโหมดเชื่อมต่อและมีพลังงานเพิ่มขึ้นเมื่ออัตราส่วนระหว่างขนาดของอนุภาคองค์ประกอบเพิ่มขึ้นโดยมีพลังงาน LSPR ต่ำสุดของทรงกลมเดี่ยวเป็นขอบเขตบน ความโค้งของเส้นโค้งพลังงาน LSPR ต่ำสุดลำดับที่สองลดลงเมื่ออัตราส่วนขนาดอนุภาคเพิ่มขึ้นโดยมีพลังงาน LSPR ต่ำสุดของทรงกลมเดี่ยวเป็นขอบเขตล่าง ในกรณีที่ทรงกลมเสียสมมาตรทั้งสองอย่าง พลังงาน LSPR ต่ำสุดของคู่ทรงกลมไม่สมมาตรไม่ถูกกักโดยพลังงานต่ำสุดของคู่ทรงกลมสมมาตรและจุดสลับโหมดมีค่าลดลงเมื่อสัดส่วนขนาดของอนุภาคมีค่าเพิ่มขึ้น

ภาควิชา ฟิสิกส์ ..... ลายมือชื่อนิสิต .....

สาขาวิชา ฟิสิกส์ ..... ลายมือชื่อ อ.ที่ปรึกษาวิทยานิพนธ์หลัก .....

ปีการศึกษา 2556 .....

4972451123 : MAJOR PHYSICS
KEYWORDS: LOCALIZED SURFACE PLASMON COUPLING/SYMMETRY BREAKING/NANOPARTICLES/ASYMMETRIC NANOPAIR

RAKCHAT KLINKLA: PLASMON MODEL OF AN ASYMMETRIC NANOSPHERE PAIR. ADVISOR: ASSOC. PROF. UDOMSILP PINSOOK, Ph.D., 80 pp.

This study focuses on the effects of symmetry breaking to the localized surface plasmon resonance (LSPR) energy of coupled nanospheres in the strongly interacting regime. First, the fundamental roles of size asymmetry and material type asymmetry are investigated separately. Then, the symmetry breaking in both particle sizes and material types are studied. The LSPR energies are obtained within the quasistatic approximation by solving the Laplace equation in bispherical coordinate system. By applying the matrix calculation, the general condition for surface mode resonance is derived in terms of nonlinear eigenvalue problem. This allows us to interpret the LSPR coupling in the asymmetric nanosphere pair as the coupling between two images of symmetric nanosphere pairs of the constituent particles. The LSPR energies of the nanosphere pairs are calculated and the excited mode order analysis for the excited mode identifying in optical measurement is established. The results show that in the case of symmetry breaking due to material type, the lowest LSPR energy has bonding mode character and is bounded by the lowest LSPR energy of the bonding symmetric pair image states. The second lowest LSPR energy has bonding (antibonding) mode character at small (large) separation distance and changes its mode character at a particular separation distance defined as mode switching point. In the case of symmetry breaking due to particle sizes, the lowest LSPR energy has bonding mode character. The energy increases as the size ratio increases and has the lowest LSPR energy of the single sphere as the upper bound. The curvature of the second lowest LSPR energy curve decreases as the size ratio increases and has the lowest LSPR energy of the single sphere as the lower bound. In the case asymmetry in both of material type and particle sizes, the lowest LSPR energy is unbounded and the value of mode switching points decrease with increasing size ratio.

Department:.....Physics.....Student's Signature .....

Field of Study:.....Physics.....Advisor's Signature .....

Academic Year:.....2013.....

ACKNOWLEDGEMENTS

I would like to express my sincere thanks to my advisor, Assoc. Prof. Dr. Udomsilp Pinsook, for his always being kindness towards me during Ph.D. Program and for his useful advices to make this dissertation complete. I highly thank Asst. Prof. Dr. Thiti Bovornratanaraks for his encouragement and financial support during my last 5 years of Ph.D. Program. I would like to thank Assoc. Prof. Dr. Mayuree Natenapit, Assoc. Prof. Dr. Nakorn Phaisangittisakul, Asst. Prof. Dr. Surachate Limkumnerd, and Dr. Sornthep Vannarat for their time to examine my thesis. I would like to thanks Asst. Prof. Dr. Sutee Boonchui and Mr. Porncharoen Palotaidamkerng for all their invaluable help and support. Especially, I would like to express my special thanks to Asst. Prof. Dr. Sutee Boonchui for his contribution in interpretation of my results. I would not have achieved this far and this dissertation would not have been completed without all the help and support that I have always received from them. I want to thank the Ratchadaphiseksomphot Endowment Fund of Chulalongkorn University (RES560530180-AM) and financial support from the Thailand Center of Excellence in Physics (ThEP), and the 90^{th} Anniversary of Chulalongkorn University Fund from Graduate School, Chulalongkorn University. This dissertation was partially supported by the National Research Council of Thailand (NRCT).

Finally, I most gratefully acknowledge my parents, sister and ECPRL members for their constant encouragement without which this assignment would not be possible.

CONTENTS

page

page

LIST OF TABLES

Table **page**

LIST OF FIGURES

Figure **page**

LIST OF SYMBOLS

Symbol	Meaning	SI Unit
ε_0	Vacuum permittivity	$\mathrm{F} \cdot \mathrm{m}^{-1}$
μ_0	Vacuum permeability	$\mathrm{N} \cdot \mathrm{A}^{-2}$
ε	Relative permittivity	—
μ	Relative permeability	—
$\mathbf{E}$	Electric field	$\mathrm{V} \cdot \mathrm{m}^{-1}$
$\mathbf{H}$	Magnetic field	$\mathrm{A} \cdot \mathrm{m}^{-1}$
$\mathbf{D}$	Dielectric displacement	$\mathrm{C} \cdot \mathrm{m}^{-2}$
$\mathbf{B}$	Magnetic induction	T
$\mathbf{J}$	Current density	$\mathrm{A} \cdot \mathrm{m}^{-2}$
$\mathbf{P}$	Polarization	$\mathrm{C} \cdot \mathrm{m}^{-2}$
$\mathbf{M}$	Magnetization	$\mathrm{A} \cdot \mathrm{m}^{-1}$
α_e	Polarizability	$\mathrm{C} \cdot \mathrm{m}^2 \cdot \mathrm{V}^{-1}$
ρ	Charge density	$\mathrm{C} \cdot \mathrm{m}^{-3}$
χ_e	Electric susceptibility	—
σ (Ch. II)	Electric conductivity	$\mathrm{S} \cdot \mathrm{m}^{-1}$
α_B	Absorption coefficient	m^{-1}
δ	Skin dept	m^{-1}
ω_p	Plasma frequency	$\mathrm{Rad} \cdot \mathrm{s}^{-1}$
ω_sp	Surface plasmon frequency	$\mathrm{Rad} \cdot \mathrm{s}^{-1}$
τ	Relaxation time	s
E_F	Fermi energy	J
c	Speed of light	$\mathrm{m} \cdot \mathrm{s}^{-1}$
e	Elementary charge	C
m	Electron mass	kg
β	Surface plasmon polariton wave vector	s
σ_ext	Extinction cross section	m^2
σ_sca	Scattering cross section	m^2
σ_abs	Absorption cross section	m^2

Symbol	Meaning	SI Unit
α	Particle size ratio	—
ξ	Scaled separation distance	—
(γ, η, ϕ)	Bispherical coordinates	—
$\delta_{i,j}$	Kronecker delta function	—
σ (Ch. V)	Sigma bonding mode	—
σ^*	Sigma antibonding mode	—
π	Pi bonding mode	—
π^*	Pi antibonding mode	—
κ_σ	Mode switching point for sigma mode	—
κ_π	Mode switching point for pi mode	—
χ	Mode crossing point	—

Chapter I

Introduction

The novel optical properties of the small metallic particle have been recognized since the age of Roman. The Lycurgus cup (4^{th} century A.D.) is the most famous example and is an evidence of the use of metallic nanoparticles in the early age. This cup appears in different colours under different conditions. It appears green when the light source is in front of it (reflected light) but appears red when the light source is inside (transmitted light) as shown in Fiq. 1.1.

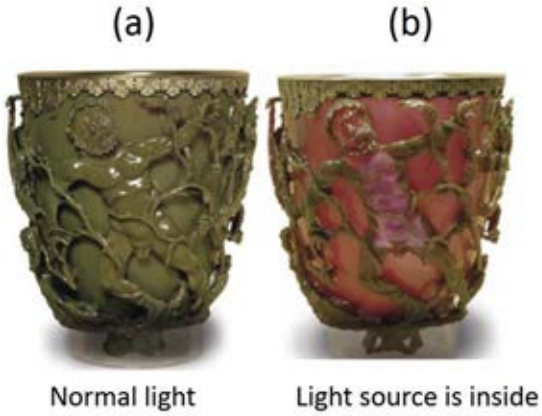

Figure 1.1: The Lycurgus cup when the light source is (a) in front of and (b) inside the cup [1].

The optical properties of the metallic nanoparticles are dominated by the collective oscillations of the conduction electron at the particle surface called surface plasmons (SPs). There are two categories of SPs. The first once exists on the large surface (or interface). This mode can couple to the radiation field and propagate along the surface called surface plasmon polaritons (SPPs). The other mode is the localized mode which is a nonpropagating mode. The subwavelength particle cannot support the propagating mode due to its size. The great interest in the localized mode excitation is the field enhancement confined in a small region close to the particle surface. The key feature of this localized surface mode

is that it can be excited by light. Thus, it can easily be detected. This has attracted the great interest over the last decade since it provides a wide range of promising applications. For example, bioimaging and photothermal therapy [2, 3], biomedical [4], surface-enhanced Raman spectroscopy (SERS) [5], solar cell [6, 7], nanoantenna [8], biosensor [9, 10, 11, 12, 13] and plasmon ruler [14].

The extensive studies have been paid for the isolated nanoparticles, especially gold nanoparticle [15, 16, 17]. More interesting is that when the particles are placed at small separation to one another. They are electromagnetically coupled to each other. The field enhancement produced by the coupled particles is much stronger than that produced by the isolated single particle due to the interaction between the plasmon modes of each particle. Moreover, the enhanced field is confined in a gap between the particles. The field enhancement and confinement are strongly dependent on shape, size, material type, dielectric environment and interparticle distance. This enables a way to trap or to manipulate light at subwavelength scales [18, 19, 20, 21]. The coupling of localized surface plasmons (LSPs) have been discussed since 1982 by Batson [22] and Ruppin [23]. Recently, a number of publications have been devoted to the topic of surface plasmon coupling, for example, field enhancement and laser-induced force [24, 25], surface plasmon enhanced optical force [26] and plasmonic bonding and antibonding forces [27]. Most of previous works are numerical studies. However, Klimov and Guzatov [28] have recently derived the analytical expressions for the resonant permittivity of the nearly touching identical spheres. Furthermore, the most interesting coupled nanostructures are an asymmetric NP pair. There have recently been intensive study both theoretically [27, 29, 30] and experimentally on this asymmetric structures [31, 32, 33, 34]. These studies have reported a dramatic change in plasmonic features of the structures such as optical active of dark plasmon modes and Fano resonance [35, 36]. As far as we know from literature review, the most intuitive description for plasmon coupling is that of plasmon hybridization model. This model describes that the plasmon coupling between two NPs can be interpreted as the hybridization of the single NPs analogous to the molecular hybridization of single atoms. That is when the single NP is placed close enough to the other they will interact to each other and form two possible hybridization states. One is the *bonding* mode which is the in-phase hybridization with lower energy, and another one is *antibonding* mode which is the out-of-phase hybridization with higher energy. This model can easily be applied to describe the LSP coupling of complex structures [37, 38, 39, 40, 41]. Recently, Sheikholeslami et al [34] have reported the experimental scattering spectra of light from the metallic nanosphere

pairs. They have found that, in case of the pair loss symmetry in both material type and particle size, the observed scattering spectra were in contrast to what would be expected from the hybridization model. Thus, it is important to investigate the effect of the symmetry breaking to the localized surface plasmon in the coupled nanostructures. This could improve our understanding and technological applications of coupled-localized surface plasmons.

In this dissertation, the introduction is given here in chapter I. The reviews of electrodynamics of solid and models of dielectric function are provided in chapter II. In chapter III, the validity of the method is discussed. The terms surface plasmon, surface plasmon polariton and localized surface plasmon resonance (LSPR) are also introduced in this chapter. In addition, the LSPR on single metallic sphere surface within the framework of Mie theory and quasistatic approximation is briefly reviewed. In chapter IV, the hybridization model of LSPR coupling is briefly introduced and discussed in detail for the quasistatic approximation method. The effects of symmetry breaking due to the internal property and geometrical property, and the excited mode order analysis are discussed in chapter V. Finally, the conclusion is given in chapter VI.

Chapter II

Optical properties of solids

Optical properties of solids are the macroscopic phenomena that result from the interaction of solids with light at the microscopic level. For instance, reflection, absorption, and scattering of light by solids. These reveal how the constituent particles of the material response to the incident electromagnetic radiation. Maxwells theory completely governs the macroscopic electromagnetic phenomena that we can observe, while details of the interactions in material are governed by quantum mechanics. However, which theory should be applied belongs to the situation we are concerning with. Hence, it is worthwhile to start with the macroscopic optical properties of solids and follows by the quantum description at the microscopic level

2.1 Electrodynamics of solids

Interaction of electromagnetic fields with matter macroscopically be described by Maxwells equations. In this theory, the material property which describes how the material responds to the perturbing field electromagnetically enters to the Maxwells equation as phenomenological parameters (ε, μ). These parameters describe the change of electric and magnetic fields in material respectively. The macroscopic Maxwells equations are given in SI units as follows:

$$\nabla \cdot \mathbf{D} = \rho, \tag{2.1a}$$

$$\nabla \cdot \mathbf{B} = 0, \tag{2.1b}$$

$$\nabla \times \mathbf{E} = -\frac{\partial \mathbf{B}}{\partial t}, \tag{2.1c}$$

$$\nabla \times \mathbf{H} = \mathbf{J} + \frac{\partial \mathbf{D}}{\partial t}, \tag{2.1d}$$

where $\mathbf{D}$, $\mathbf{E}$, $\mathbf{H}$, $\mathbf{B}$, ρ and $\mathbf{J}$ are the dielectric displacement, the electric field, the magnetic field, magnetic induction, external charge density, and external current

density respectively. Furthermore, these four macroscopic fields are linked through polarization $\mathbf{P}$ and magnetization $\mathbf{M}$ by

$$\mathbf{D} = \varepsilon_0 \mathbf{E} + \mathbf{P}, \tag{2.2}$$

$$\mathbf{H} = \frac{1}{\mu_0}\mathbf{B} - \mathbf{M}, \tag{2.3}$$

where ε_0 and μ_0 are electric permittivity and magnetic permeability of vacuum respectively. The polarization $\mathbf{P}$ is related to $\mathbf{E}$ by

$$\mathbf{P} = \varepsilon_0 \chi_\mathrm{e} \mathbf{E} \tag{2.4}$$

where χ_e is the macroscopic susceptibility of the material. In general, χ_e is a function of $\mathbf{E}$ (optical nonlinearily). However, if the exciting field strength is small ($E \lesssim 100\ \mathrm{V/m}$) [42] the relation between $\mathbf{P}$ and $\mathbf{E}$ is linear. This is the linear respond regime. In an isotropic and homogeneous material, χ_e is scalar that depends on the perturbing field frequency. In this regime the relation between $\mathbf{M}$ and $\mathbf{H}$ is also linear. In this dissertation, we focus on the nonmagnetic materials. Thus, we will only consider the electric response by assuming the relative magnetic permeability of the material is unity. From Eq. 2.3 and Eq. 2.4, we can write

$$\mathbf{D} = \varepsilon_0(1 + \chi_\mathrm{e})\mathbf{E} = \varepsilon_0 \varepsilon \mathbf{E}, \tag{2.5}$$

where $\varepsilon = 1 + \chi_\mathrm{e}$ is the dielectric constant which in general is a function of frequency and wave vector (sometimes referred to as permittivity). Within the linear response regime, we also assume that the material obeys Ohms law $\mathbf{J} = \sigma \mathbf{E}$. Collecting all these relations along with Eq. 2.1, it is easy to show that

$$\nabla(\nabla \cdot \mathbf{E}) - \nabla^2 \mathbf{E} = -\mu_0 \sigma \frac{\partial \mathbf{E}}{\partial t} - \mu_0 \frac{\partial^2}{\partial t^2}(\varepsilon \mathbf{E}). \tag{2.6}$$

Now, we look for the *ansatz* solution of Eq. 2.6 in form of time-harmonic plane wave such as

$$\mathbf{E}(\mathbf{r}, t) = \mathbf{E}_0 e^{i(\mathbf{k}\cdot\mathbf{r} - \omega t)}. \tag{2.7}$$

Substituting Eq. 2.7 into Eq. 2.6, we obtain two dispersion relations. First for transverse wave, that is

$$k^2 = \mu_0(\varepsilon\omega^2 + i\sigma\omega) = \frac{\omega^2}{c^2} N^2, \tag{2.8}$$

where $N = n + i\kappa = \sqrt{\tilde{\varepsilon}}$, and $\tilde{\varepsilon} = \frac{\varepsilon}{\varepsilon_0} + i\frac{\sigma}{\varepsilon_0 \omega} = \varepsilon_1 + i\varepsilon_2$ are complex refractive index and complex dielectric function respectively. The second for the longitudinal wave, that is

$$\varepsilon(\mathbf{k}, \omega) = 0. \tag{2.9}$$

Let us assume that the wave propagates in the z direction. Substituting the complex wave vector yields

$$\mathbf{E}(\mathbf{r},t) = \mathbf{E}_0 e^{i(\frac{\omega}{c}nz-\omega t)} \cdot e^{-(\frac{\omega}{c}\kappa z)}. \tag{2.10}$$

One can see that the imaginary part of the complex refraction index plays the role in absorption and it is linked to the absorption coefficient of Beers law ($I(x) = I_0 e^{-\alpha_B x}$) by

$$\alpha_B(\omega) = \frac{2\omega K(\omega)}{c} = \frac{2}{\delta} \tag{2.11}$$

where $\delta = \frac{c}{\omega\kappa}$ is the skin depth defined as the characteristic distance that the electromagnetic fields can penetrate into metals. Another measurable optical quantity is the reflection coefficient of reflectivity which is given in the case of normal incident by [43]

$$R = \frac{(n-1)^2+\kappa^2}{(n+1)^2+\kappa^2} \tag{2.12}$$

Since $\varepsilon^2 = N$, keeping this in mind, the optical properties of solids can be extracted from the study of dielectric function. Thus it is termed as the optical constant of solids. This macroscopic viewpoint of the optical properties of solids can be linked to the microscopic viewpoint by the model of dielectric function as will be discussed in the following sections.

2.2 Models of dielectric function

2.2.1 Lorentz oscillator

Before the discovery of quantum theory, Hendrik Antoon Lorentz, the late 19$^{\text{th}}$ century physicist, attempted to describe the interaction between atoms and electric fields using the classical mechanics and electromagnetic theory. He modeled the atom as a massive particle (Nucleus) connected to the a very small mass particle (electron) by a spring as schematically shown in Fig 2.1

The spring represents the binding force which bounds the electron in an atom. He postulated that this force obeys Hook's law. Consequently, when the electron is displaced from its equilibrium position by the perturbing external field, this system forms a harmonic oscillator as is called Lorentz oscillator. Assume that the Lorentz oscillator is exposed in the time harmonic electric field $\mathbf{E} = \mathbf{E}_0 e^{-i\omega t}$. The equation of motion of an electron is given by

$$m\frac{\partial^2 \mathbf{r}}{\partial t^2} + m\gamma\frac{\partial \mathbf{r}}{\partial t} + m\omega_0^2\mathbf{r} = -e\mathbf{E}, \tag{2.13}$$

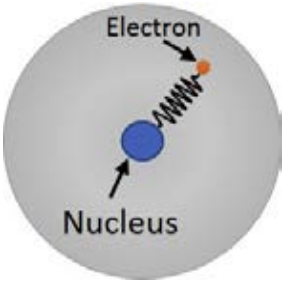

Figure 2.1: An electron attached to the Nucleus by spring force.

where $\mathbf{r}, \gamma$ and $m\omega_0$ are their electron displacement, damping constant, and restoring (binding) force respectively. The solution of Eq. 2.13 is $\mathbf{r}(t) = \frac{-(e/m)\mathbf{E}}{\omega_0^2 - \omega^2 - i\omega\gamma}$. The macroscopic polarization is given by $\mathbf{P} = n(-e\mathbf{r}) = \frac{\left(ne^2/m\right)\mathbf{E}}{\omega_0^2 - \omega^2 - i\omega\gamma}$. From Eq. 2.3, Eq. 2.4, and Eq. 2.5, we obtain

$$\epsilon(\omega) = 1 + \frac{\omega_{\mathrm{p}}^2}{\omega_0^2 - \omega^2 - i\omega\gamma} \tag{2.14}$$

where $\omega_{\mathrm{p}} = \frac{ne^2}{\varepsilon_0 m}$ is plasma frequency. This model can be extended to the system that is a collection of different oscillators by summing over all contributions from each oscillator.

2.2.2 Drude free electron

In 1900, just three years after Thomsons discovery of electrons, Paul Karl Ludwig Drude established the microscopic theory of thermal and electrical conduction [44, 45]. In this model, the metal composes of nearly free valence electron gases immersed by the stationary ion core which is the combination of the tightly bound inner core electron and nucleus. The model is shown schematically in Fig 2.2

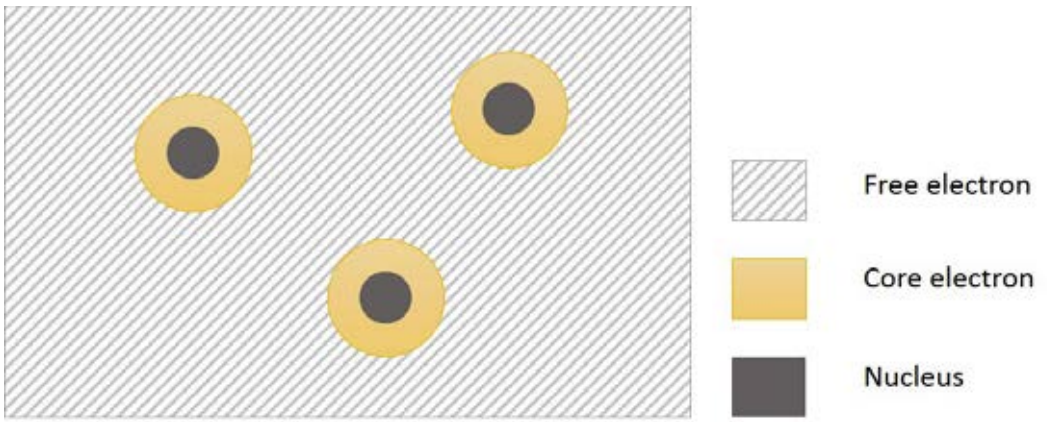

Figure 2.2: Model of the electrons in metal. (figure adapted from Ref.[46]).

With this simple model, he applied the classical kinetic theory of the dilute gases to the highly dense conduction electron gas in metal with a few assumptions as follows [46]:

1. The interaction of a given electron both with the others and with ions are neglected. The electrons move under the influence of the external field only and they obey Newton's laws of motion.

2. The electron-electron collision is neglected. Only the electron-ion core collision is taken into account as shown in Fig 2.3.

3. The probability of an electron undergoing a collision in the infinitesimal time interval dt is $\frac{dt}{\tau}$. The time τ is referred to as the relaxation time which is the average time interval that an electron moves freely before its next collision since its last collision.

4. Electrons equilibrate by means of collision.

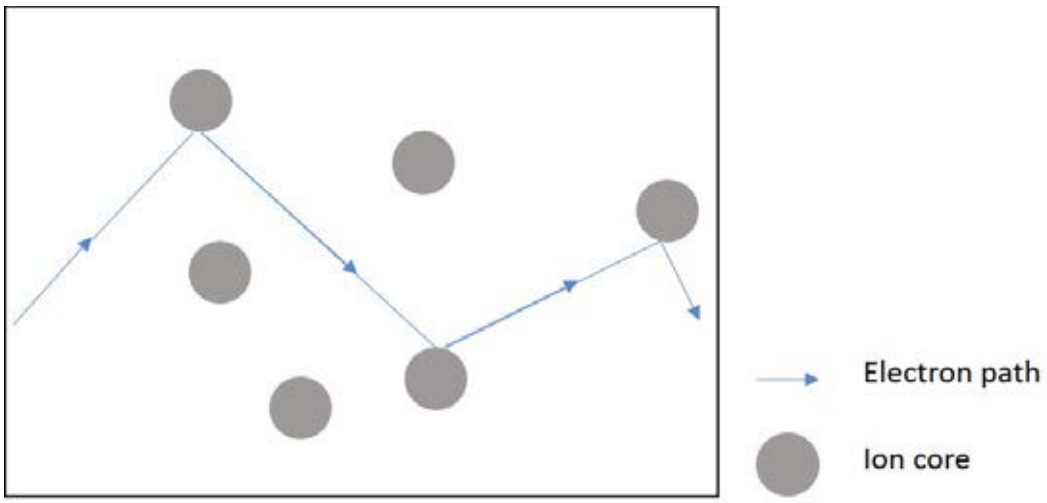

Figure 2.3: Electron motion in Drude metal. (the figure modified from Ref.[46]).

With these assumptions the equation of motion of an electron under the influence of the external force can be obtained by considering the average momentum change per electron. Suppose $\mathbf{p}(t)$ is an average momentum per electron at time t and $\mathbf{p}(t+dt)$ is an average momentum per electron at time $t+dt$. The major contribution to $\mathbf{p}(t+dt)$ comes from the electrons that do not experience the collision in the time interval dt. The probability that the electrons do not undergo the collision is $\left(1-\frac{dt}{\tau}\right)$. If these electrons are moving under the influence of the

external force $\mathbf{f}(t)$ their momentum at time $t + dt$ is

$$\begin{aligned}\mathbf{P}(t+dt) &= \left(1 - \frac{dt}{\tau}\right)[\mathbf{p}(t) + \mathbf{f}(t)dt + O(dt)^2] \\ &= \mathbf{p}(t) - \frac{dt}{\tau}\mathbf{p}(t) + \mathbf{f}(t)dt + O(dt)^2. \end{aligned} \tag{2.15}$$

By neglecting terms of orders higher than dt and taking the limit as $dt \to 0$, we obtain

$$\frac{d\mathbf{p}}{dt} = -\frac{\mathbf{p}}{\tau} + \mathbf{f}(t). \tag{2.16}$$

This is the Drude equation of motion which introduce the effect of individual electron scattering by the ion cores into the equation through the damping constant $\left(\frac{1}{\tau}\right)$. Next, consider the response of the conduction electron to a monochromatic electric field $\mathbf{E} = \mathbf{E}_0 e^{-i\omega t}$. From Eq. 2.16, the equation of motion becomes

$$\frac{d\mathbf{p}}{dt} + \frac{\mathbf{p}}{\tau} = -e\mathbf{E}_0 e^{-i\omega t}. \tag{2.17}$$

or

$$m\frac{d^2\mathbf{r}}{dt^2} + \frac{m}{\tau}\frac{\mathbf{r}}{dt} = -e\mathbf{E}. \tag{2.18}$$

Similarly to the Lorentz model, the solution is

$$\mathbf{r}(t) = \frac{(e/m)\,\mathbf{E}}{\omega^2 + \frac{i\omega}{\tau}}, \tag{2.19}$$

which yields the complex dielectric function as

$$\varepsilon(\omega) = \varepsilon_1 + i\varepsilon_2 = 1 - \frac{\omega_p^2}{\omega^2 + i\frac{\omega}{\tau}} \tag{2.20}$$

As one can see from Eq. 2.14 and Eq. 2.20, in the case $\omega_0 = 0$, the Lorentz dielectric function equivalent to Drude dielectric function. The Drude dielectric function can be obtained by neglecting the effect of bound electron. On the other hand, Drude model describes physics at the Lorentz damping constant which, at that time, is added into the equation of motion as a phenomenological parameter. The Lorentz damping constant is related to the Drude relaxation time by $\gamma_{\text{Lorentz}} \equiv \frac{1}{\tau_{\text{Drude}}}$. Hence, sometime, the free electron dielectric function is referred to as Drude-Lorentz dielectric function.

2.2.3 Hubbard model

This model is the quantum mechanical description of the linear response of the electronic system by considering the electron density fluctuation due to a small

perturbation. The behavior of the electronic system under the small perturbation can be investigated by considering the average density fluctuation $\langle \delta n(\mathbf{r},t)\rangle$ is related to the perturbing external potential, $\Phi_{\rm ext}$, by [47]

$$< \delta n(\mathbf{r},t) >= -e \int d\mathbf{r}' \int dt'\, \eta(\mathbf{r},\mathbf{r}',t-t')\Phi_{\rm ext}(\mathbf{r}',\mathbf{t}). \tag{2.21}$$

where

$$\eta(\mathbf{r},\mathbf{r}',t-t') = -\frac{i}{\hbar}\Theta(t-t') < [n(\mathbf{r}),n(\mathbf{r}')] > \tag{2.22}$$

is the autocorrelation function, and $\Theta(t-t')$ is the Heaviside step function. The fluctuation density induces the additional potential $\Phi_{\rm ind}$. Hence, the electrons are moving under the total potential

$$\Phi_{\rm t}(\mathbf{r},t) = \Phi_{\rm ext}(\mathbf{r},t) + \Phi_{\rm ind}(\mathbf{r},t) \tag{2.23}$$

The fields $\mathbf{D}$ and $\mathbf{E}$ can be written as the negative gradient of $\Phi_{\rm ext}$ and $\Phi_{\rm t}$ respectively. These relations in Fourier space read

$$\mathbf{D}(\mathbf{k},\omega) = \varepsilon_0 \mathbf{k}\Phi_{\rm ext}(\mathbf{k},\omega), \tag{2.24}$$

$$\mathbf{E}(\mathbf{k},\omega) = \mathbf{k}\Phi_{\rm t}(\mathbf{k},\omega), \tag{2.25}$$

and

$$\mathbf{D}(\mathbf{k},\omega) = \varepsilon_0\varepsilon(\mathbf{k},\omega)\mathbf{E}(\mathbf{k},\omega), \tag{2.26}$$

Substituting Eq.(2.23), Eq.(2.24), and Eq.(2.25) into Eq.(2.26) yields

$$\frac{1}{\varepsilon(\mathbf{k},\omega)} = 1 + \frac{\Phi_{\rm ind}}{\Phi_{\rm ext}} \tag{2.27}$$

From Poissons equation and Eq.(2.21) in the Fourier space, Eq.(2.27) becomes

$$\frac{1}{\varepsilon(\mathbf{k},\omega)} = 1 + \frac{e^2}{\varepsilon_0 k^2}\eta(\mathbf{k},\omega). \tag{2.28}$$

Therefore, the problem of dielectric function calculation becomes the autocorrelation function calculation. For the simple homogeneous electron gas, it is given by

$$\eta^0(\mathbf{k},\omega) = \frac{2}{V}\sum_{k'} \frac{f(E_k) - f(E_{k+k'})}{\hbar\omega + i\Delta + E_k - E_{k+k'}} \tag{2.29}$$

with

$$E_{\rm k} = \frac{\hbar^2 k^2}{2m} \tag{2.30}$$

where $f(E_{\rm k})$ is the Fermi distribution function, V is the volume of the electron gas, and Δ is an infinitesimal positive real number. However, using this simple autocorrelation function for the dielectric function, Eq. 2.28, of the interacting

electron gas is not a good approximation. The modification is performed by using $\Phi_{\rm t}$ instead of $\Phi_{\rm ext}$ in Eq. 2.21 since the electron located in the total field and by adding the exchange and correlation terms. The resulting dielectric function is given by (for the detail of calculation, see Ref.[47])

$$\varepsilon(\mathbf{k},\omega) = 1 - \frac{e^2}{\varepsilon_0 k^2}\frac{\eta^0}{1+\frac{e^2}{\varepsilon_0 k^2}G^0(\mathbf{k})\eta^0} \tag{2.31}$$

where $G^0(\mathbf{k})$ is the exchange and correlation terms and is proposional to k^2 for small k and converges to constant for large k. This dielectric function is known as Hubbard dielectric function. By neglecting the exchange and correlation effects, which is the case in random phase approximation (RPA), the dielectric function reduces to the simple form

$$\varepsilon^{\rm RPA} = 1 - \frac{e^2}{\varepsilon_0 k^2}\eta^0(\mathbf{k},\omega). \tag{2.32}$$

This is also known as Lindhard dielectric function. In limit $k \to 0$, it can be showed that [48]

$$\lim_{k\to 0}\varepsilon^{\rm RPA}(\mathbf{k},\omega) = 1 - \frac{\omega_{\rm p}^2}{\omega^2} = \epsilon^{\rm Drude} \tag{2.33}$$

And for $k \neq 0$ the long wave length regime is given by [49]

$$\varepsilon^{\rm RPA}(\mathbf{k},\omega) = 1 - \frac{\omega_{\rm p}^2}{\omega^2}\left(1 + \frac{6}{5}\frac{E_{\rm F}k^2}{m\omega^2}\right) \tag{2.34}$$

where $E_{\rm F}$ is Fermi energy. In this model, even in the simple approximation, the dielectric function is the consequence of the excitation of the electronic system as one can see from Eq.(2.31) and Eq.(2.29). Now, let us discuss the optical response of metals using the simple free electron model. According to Drude dielectric function, we can divide the frequency domain into three regimes corresponding to their physically distinct, as shown in Fiq. 2.4. The first frequency regime is the absorbing regime, $0 < \omega\tau \lesssim 1$, In this frequency range, the metal absorbs the incident electromagnetic field, because

$$n \approx \kappa \approx \sqrt{\frac{\tau\omega_{\rm p}^2}{2\omega}} \tag{2.35}$$

The second frequency regime is the reflecting regime, $1 < \omega\tau < \omega_{\rm p}\tau$. In this regime,

$$n \approx \frac{\omega_{\rm p}^2}{2\tau\omega^2\sqrt{\omega_{\rm p}^2-\omega^2}}, \quad \kappa \approx \sqrt{\frac{\omega_{\rm p}^2}{\omega^2}-1}. \tag{2.36}$$

Furthermore, $n \ll k$. Thus, from Eq. 2.12, almost all incident electromagnetic wave will be reflected. The last regime lies in the frequency range $\omega \geq \omega_{\rm p}$. This is

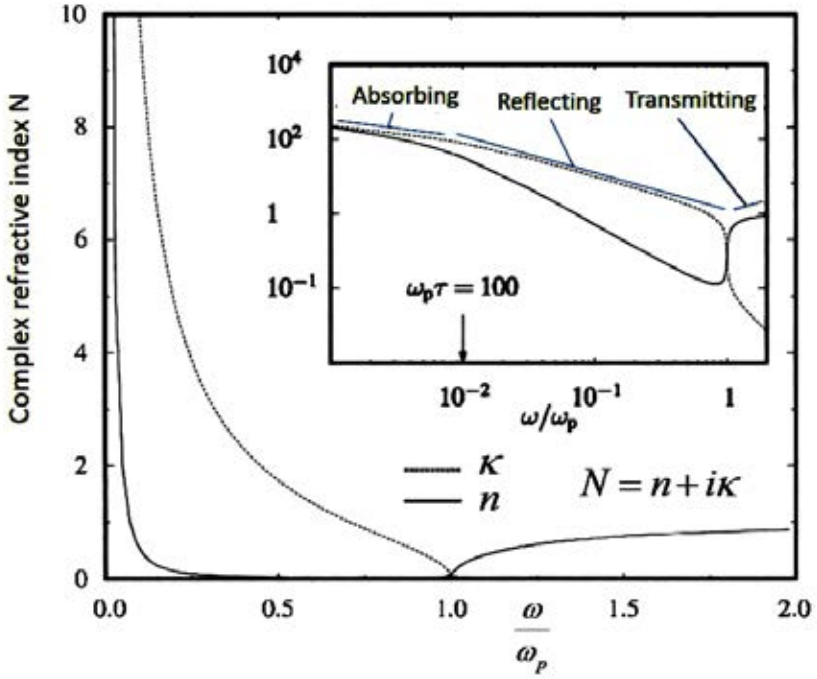

Figure 2.4: Real and imaginary parts of the complex index of refraction for Drude metal with $\omega_p\tau = 100$.[49]

the transparent regime, because n is positive and much larger than κ as given by

$$n \approx \sqrt{1 - \frac{\omega_{\mathrm{p}}^2}{\omega^2}}, \quad \kappa \approx \frac{\omega_{\mathrm{p}}^2}{2\tau\omega^2\sqrt{\omega_{\mathrm{p}}^2 - \omega^2}}. \tag{2.37}$$

2.2.4 Volume plasmons

In this section, we will discuss the dispersion relation of the electromagnetic wave traveling through the metal. By using the free electron model. The dispersion relation for transverse wave can be obtained from Eq.(2.8) and Eq.(2.20) as

$$\omega^2 = \omega_{\mathrm{p}}^2 + k^2c^2 \tag{2.38}$$

A plot of this dispersion relation is shown in Fiq. 2.5. The shaded region is the forbidden region (forbidden frequency gab) for electromagnetic wave propagation in metal. Hence, only the transverse electromagnetic wave with $\omega > \omega_{\mathrm{p}}$ can propagate through the metal. Furthermore, there is another excitation satisfying Eq. 2.9 which is the longitudinal excitation of the electron gas. For $k = 0$, this excitation condition is satisfied at $\omega = \omega_{\mathrm{p}}$. The intuitive physical interpretation of ω_{p} can be found in Ref.[49] by considering the motion of a slab of the free electron gas immersed in the fixed position ion core (Jellium model) as schematically illustrated in Fig. 2.6 Suppose that the whole slab of electrons are displaced

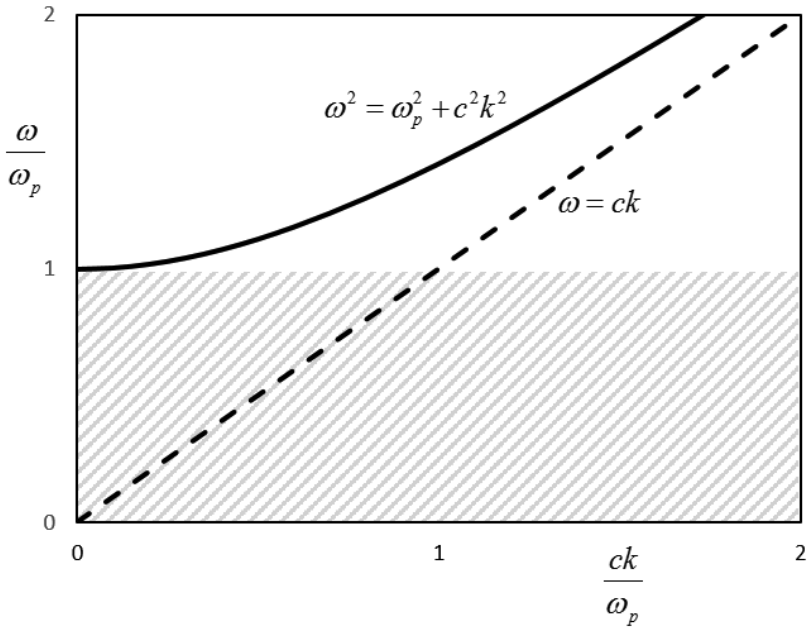

Figure 2.5: The dispersion relation for the transverse electromagnetic wave in free electron gas. The shaded region is the forbidden frequency gap.

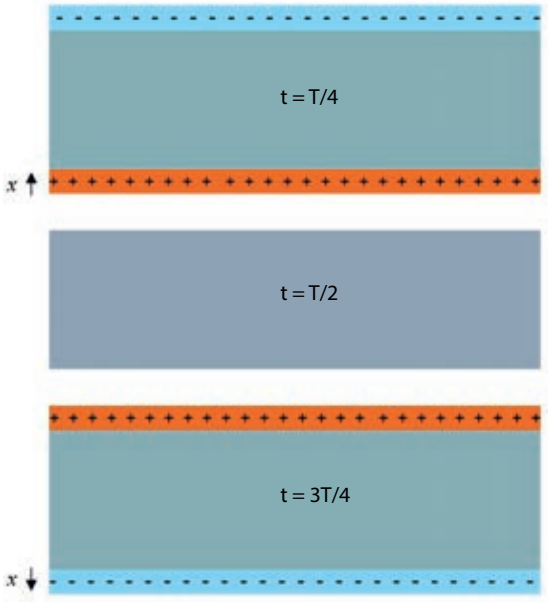

Figure 2.6: Schematically illustration of the collective motion of the free (conduction) elections in a metal at time $t = \frac{T}{4}, \frac{T}{2}, \frac{3T}{4}$ respectively where T is an oscillation period.

Material	ω_{p} (eV)
Li	7.12[1]
Na	5.71[1]
K	3.72[1]
Mg	10.6[1]
Al	12.7[2]
Ag	9.2[2]
Au	8.9[2]
Cu	8.7[2]

Table 2.1: Plasmon energy of typical metals. [1]Ref.[50], [2]Ref.[51]

from its equilibriums with the collective displacement x as indicated in the figure. This develops the surface charge density $\pm nex$ at each slab boundaries. Thus, the uniform electric field $E = \frac{nex}{\varepsilon_0}$ is developed between such slab boundaries and the collective electrons experience a restoring force density $f = -neE$. In this situation, Newtons second law yields the following equation of motion

$$nm\ddot{x} = -\frac{n^2e^2\mu}{\varepsilon_0} \tag{2.39}$$

or

$$\ddot{x} + \omega_{\mathrm{p}}^2 x = 0 \tag{2.40}$$

which describes the collective oscillations of the electrons with natural frequency ω_{p}. Therefore, this longitudinal excitation at $k = 0$ is the (longitudinal) collective oscillations and their quanta are called *bulk plasmons* or *volume plasmons* or *Plasmon resonance*. Furthermore, the bulk plasmons can not only exist at $k = 0$ but also at finite k. For examples in the long wave length limits the dielectric function is given in Eq. 2.34 which leads to the Plasmon dispersion relation as

$$\omega^2 = \omega_{\mathrm{p}}^2 + \frac{6}{5}\frac{E_{\mathrm{F}}k^2}{m\omega^2}. \tag{2.41}$$

The experimental observation of the Plasmon excitations can be performed by the electron energy loss spectroscopy (EELS) whereby the energy losses of the electrons passed though the thin metallic foils corresponding to the Plasmon excitations are measured. The Plasmon energy of typical metals are given in Table. 2.1

Chapter III

Surface plasmon resonance

In chapter II, we discussed the interaction between light and metal which inaugurates the bulk plasma oscillation. The quantization of this excitation is called plasmon, more specifically volume/bulk plasmon, which was described quantum mechanically by Pines and Bohm [52] in 1952 when they analyzed the energy loss spectrum of fast electrons passing through the thin metal foils. They showed that this excitation is an elementary excitation of solids using the quasiparticle concept. In their analysis, volume of the electron gas is assumed to be very large. Thus, there is no boundary effect included in their description of the bulk plasmon excitation. In 1957, Ritchie extended the work of Pines and Bohm by introducing the effect of the foils boundary surfaces [53]. He found that the presence of boundary surfaces induces the new excitation modes due to the *surface collective oscillations*. He termed this new excitations as *surface plasmon* (SP). The existence of SPs was demonstrated experimentally in 1960 by Stern and Ferrell [54].

In addition, there are a variety of names used to refer to the SPs such as [55] *surface plasmon polariton* (SPP) which emphasizes the coupling of electronic excitation in the metals with the exciting electromagnetic fields, *surface plasma waves* (SPWs), *surface plasma oscillations* (SPOs), *surface electromagnetic wave* (SEWs). The other names of SPs which emphasize the non-propagating and field enhancement natures of SPs are *localized surface plasmons* (LSPs) and *localized surface plasmon resonance* (LSPR). In this dissertation, we will focus on the non-propagating LSPR and the others will be discussed as the introduction survey.

3.1 Validity of the classical description

Plasmons and/or SPs are the quantum (quasi) particles with definite energies and momenta (for propagating plasmons). One might argue that their properties should be described in the context of quantum mechanics rather than the classical electrodynamics. This argument is discussed by Bohren and Huffman [56], and

Sarid and Challener [55] in their text books. It is worth showing here a Bohren and Huffman paragraph, that is:

> The choice of quantum-mechanical or classical language to describe modes in small particles is dictated more by taste than by necessity. However, there is an unfortunate tendency among physicists to consider that "Quantum mechanics is intrinsically better than classical mechanics, and that classical mechanics is something real physicists ought to grow out of"; we agree with Pipard (1987, p.3) that this is a "disputable proposition". Indeed, much mischief has been done—and still being done—by incorrectly applying quantum theory to "explain" the strange optical behavior of small particles. Surface modes in small particles are adequately and economically described in their essentials by simple classical theories. Even, however, in the classical description, quantum mechanics is larking unobtrusively in the background; but it has all been rolled up into a handy, ready-to-use form: the dielectric function, which contains all the required information about the collective as well as the individual particle excitations. The effect of a boundary, which is, after all, a macroscopic concept, is taken care of by classical electromagnetic theory.

Sarid and Challener add to this argument that this statement is not valid only for small particles but also all the plasmonic system. They state that the classical description is generally adequate as long as the particles supporting SPs are large enough that they can be described by the macroscopic a dielectric functions. In practice, the bulk dielectric function can be accurately used to describe the particle with size down to $\lesssim$ 10 nm. Below this the dielectric function has to be modified as a size-dependent dielectric function and it is acceptable for the particle size down to $\lesssim$ 1-2 nm. In this dissertation, we strictly concern with the particles with sizes larger than 10 nm and much smaller than the visible optical wave length. Therefore, the classical electrodynamics description is adequate in our case.

3.2 Surface plasmon polaritons

Surface plasmon polaritons (SPPs) are the propagating SP modes sustaining at the dielectric/metal interface. For simplicity, let us consider the time-harmonic

electromagnetic wave propagating along the planar interface (at $z = 0$). In the absence of the external sources, $\rho = 0$ and $\mathbf{J} = 0$, the Maxwells equations (2.1) yield

$$\nabla^2\mathbf{E} - \frac{\varepsilon}{c^2}\frac{\partial^2\mathbf{E}}{\partial t^2} = 0 \tag{3.1}$$

Where $c^2 = \frac{1}{\mu_0\varepsilon_0}$. We assume that $\mathbf{E}$ is a time-harmonic function,

$$\mathbf{E}(\mathbf{r}, t) = \mathbf{E}(\mathbf{r})e^{-i\omega t}. \tag{3.2}$$

Substituting Eq. 3.2 into Eq. 3.1 yields

$$\nabla^2\mathbf{E} + k_0^2\varepsilon\mathbf{E} = 0, \tag{3.3}$$

where $k_0^2 = \frac{\omega^2}{c^2}$. In the case that wave propagating along the x-axis, it time-independent part can be described by

$$\mathbf{E}(\mathbf{r}) = \mathbf{E}(z)e^{i\beta x}, \tag{3.4}$$

where β is the complex wave vector in the propagating direction. By substituting Eq. 3.4 into Eq. 3.3, we obtain

$$\frac{\partial^2\mathbf{E}(z)}{\partial z^2} + (k_0^2\varepsilon - \beta^2)\mathbf{E} = 0. \tag{3.5}$$

This is the Helmholtz equation for determining the z-dependence of the field amplitude. Similarly, One can obtain the same expression for $\mathbf{H}$ field by applying the same manner as the preceding procedures. Now, let we turn to the curl equations, Eq. 2.1c and Eq. 2.1d. For the time-harmonic fields, these two equations yield

$$\begin{pmatrix} \frac{\partial E_z}{\partial y} - \frac{\partial E_y}{\partial z} \\ \frac{\partial E_x}{\partial z} - \frac{\partial E_z}{\partial x} \\ \frac{\partial E_y}{\partial x} - \frac{\partial E_x}{\partial y} \end{pmatrix} = i\omega\mu_0 \begin{pmatrix} H_x \\ H_y \\ H_z \end{pmatrix} \tag{3.6}$$

and

$$\begin{pmatrix} \frac{\partial H_z}{\partial y} - \frac{\partial H_y}{\partial z} \\ \frac{\partial H_x}{\partial z} - \frac{\partial H_z}{\partial x} \\ \frac{\partial H_y}{\partial x} - \frac{\partial H_x}{\partial y} \end{pmatrix} = -i\omega\varepsilon_0\varepsilon \begin{pmatrix} E_x \\ E_y \\ E_z \end{pmatrix} \tag{3.7}$$

From Eq. 3.4, Eq. 3.6 and Eq. 3.7 reduce to

$$\begin{pmatrix} \frac{\partial E_y}{\partial z} \\ \frac{\partial E_x}{\partial z} i\beta E_z \\ i\beta E_y \end{pmatrix} = i\omega\mu_0 \begin{pmatrix} H_x \\ H_y \\ H_z \end{pmatrix} \tag{3.8}$$

and

$$\begin{pmatrix} \frac{\partial H_y}{\partial z} \\ \frac{\partial H_x}{\partial z} i\beta H_z \\ i\beta H_y \end{pmatrix} = -i\omega\varepsilon_0\varepsilon \begin{pmatrix} E_x \\ E_y \\ E_z \end{pmatrix} \tag{3.9}$$

There are two sets of solutions of the system of coupled equations, Eq. 3.8 and Eq. 3.9, depending on the polarization of the traveling waves. For simplicity let us consider the case of single planar interface which the upper half infinite space ($z > 0$) is filled by the dielectric medium with real dielectric constant ε_2 and the lower half infinite space ($z < 0$) is filled by the conducting medium (metal) with the dielectric function ε_1 as illustrated in Fig. 3.1. First we look for the solutions

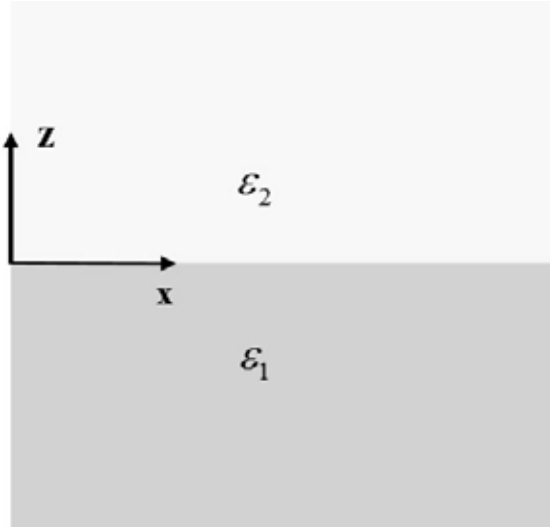

Figure 3.1: The single dielectric/metal interface. The upper half space is filled by dielectric ε_2 and the lower half space is filled by metal ε_1.

in case of the traveling waves are the transverse magnetic (TM) modes. For this polarization, the solutions are given by

$$\mathbf{H}(\mathbf{r}) = (0, A_j, 0)e^{i\beta x} \cdot e^{k_j|z|}, \tag{3.10a}$$

$$\mathbf{E}(\mathbf{r}) = \left((-1)^j i A_j k_j, 0, -A_j\beta\right) \frac{e^{i\beta x} \cdot e^{-k_j|z|}}{\omega\varepsilon_0\varepsilon_j}, \tag{3.10b}$$

where $j = 1, 2$ for lower half and upper half spaces respectively, $k_j\sqrt{\beta^2 k_0^2 \varepsilon_j}$ is the component of wave vector in z-direction in the region j, and A_j are arbitrary constants will be determined by the boundary conditions. By applying the boundary conditions, H_y and $\varepsilon_j E_z$ are continuous across the interface, it is required that

$$A_1 = A_2, \tag{3.11}$$

and

$$\frac{k_2}{k_1} = -\frac{\varepsilon_2}{\varepsilon_1}. \tag{3.12}$$

From Eq. 3.12, the propagating wave vector can be derived as

$$\beta = k_0 \sqrt{\frac{\varepsilon_1 \varepsilon_2}{\varepsilon_1 + \varepsilon_2}}, \tag{3.13}$$

and, furthermore, k_j can be rewritten in the following form

$$k_j = k_0 \sqrt{\frac{-\varepsilon_j^2}{\varepsilon_1 + \varepsilon_2}}. \tag{3.14}$$

Next, let us consider the transverse electric (TE) modes. The solutions of these modes are given by

$$\mathbf{E}(\mathbf{r}) = (0, A_j, 0) e^{i\beta x} \cdot e^{k_j |z|}, \tag{3.15a}$$

$$\mathbf{H}(\mathbf{r}) = \left((-1)^{j-1} i A_j k_j, 0, A_j \beta\right) \frac{e^{i\beta x} \cdot e^{-k_j |z|}}{\omega \mu_0}. \tag{3.15b}$$

By applying the boundary conditions which are the continuity of E_y and H_x at the interface,

$$A_1 = A_2, \tag{3.16}$$

and

$$A_1 (k_1 + k_2) = 0. \tag{3.17}$$

Finally, we discuss the properties of the main results. It is obvious from Eq. 3.10, and Eq. 3.15 that β describes wave propagating along the interface while k_j describes the field confinement in each side of the interface. The electromagnetic fields will be confined in the vicinity of the interface if and only if $\mathrm{Re}[k_1] > 0$ and $\mathrm{Re}[k_2] > 0$. Furthermore, we can define the characteristic attenuation length as the distance from the interface in the perpendicular direction that the field amplitude fall off by the factor e^{-1} by $l_i = \frac{1}{\mathrm{Re}[k_i]}$ for $i = 1, 2$. It is clear that, for TM modes, the dielectric/metal interface fulfill the confinement condition (Eq. 3.12). In contrast, for TE modes. Eq. 3.16 and Eq. 3.17 imply that the confinement condition can be satisfied only if $A_1 = A_2 = 0$. Therefore, only the TM polarization electromagnetic waves can couple to the collective surface mode excitations. Strictly speaking, surface plasmon polariton can only be excited by the TM wave. The electric field associated with the SPPs excitation is schematically illustrated in Fig. 3.2 and the plots of l_is in each side of the Drude metal/vacuum interface as a function of SPPs wave vector are shown in Fig. 3.3.

At small wave number, the field on the vacuum side extend over the wavelength whereas the attenuation length on the metal side approaches a constant known as the skin depth. Interestingly, in the large wave number region, the field

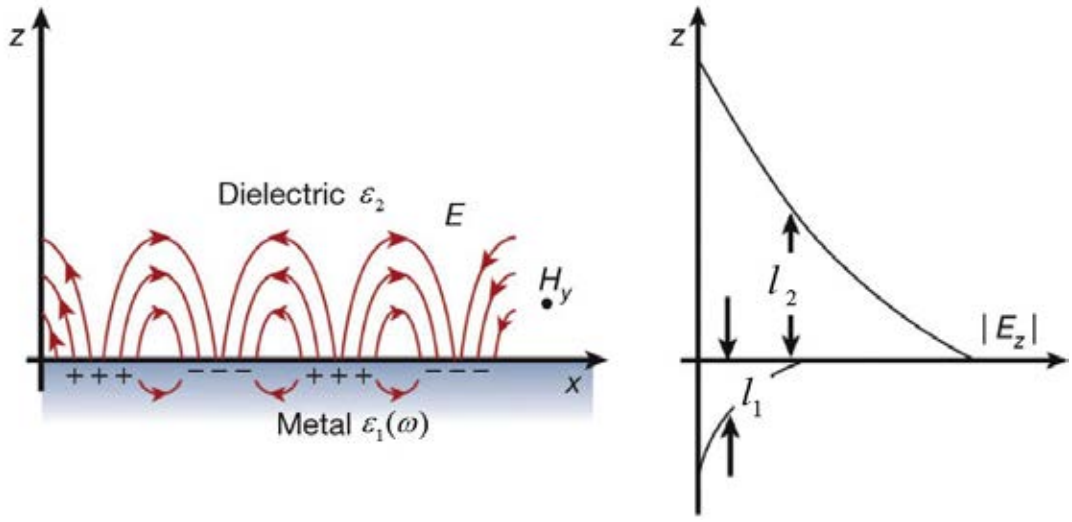

Figure 3.2: The schematically illustration of the electric field associated with the SPPs [57].

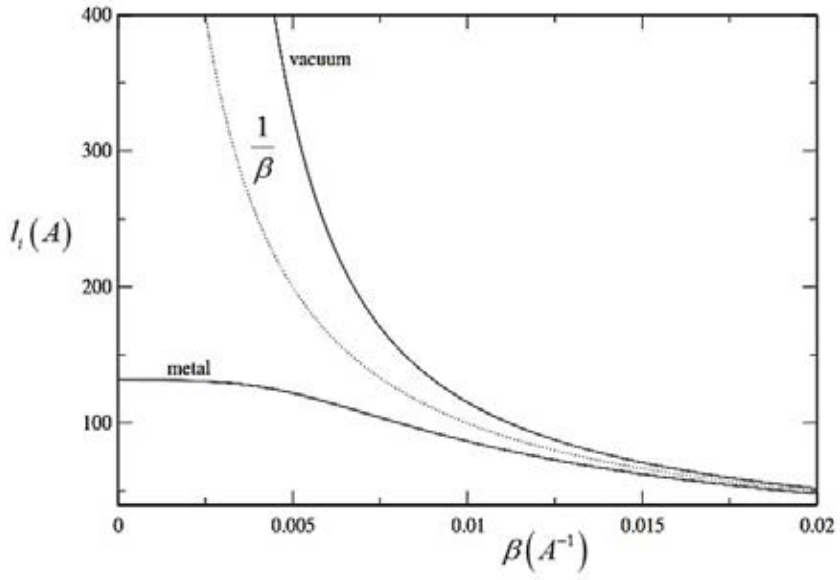

Figure 3.3: The attenuation length of the electric fields in vacuum and in Drude metal with $\omega_p = 15$ eV compared with SPPs wave length $\frac{1}{\beta}$ (dotted line) [58].

has a strong concentration in the vicinity of the surface, $l_i \sim \frac{1}{\beta}$, and the condition $\varepsilon_1 + \varepsilon_2 = 0$ is fullfilled as one can see in Eq. 3.13. To investigate more properties of this surface mode excitation, we look for the dispersion relations of SPPs on the interface of lossless Drude metal and air which can be derived from Eq. 3.13 as

$$\omega^2(\beta) = \frac{\omega^2}{2} + c^2\beta^2 \pm \sqrt{\frac{\omega_{\mathrm{p}}^4}{4} + c^4\beta^4}, \tag{3.18}$$

Eq. 3.18 with minus sign on the right hand side corresponding to the surface mode whereas the plus sign corresponding to the volume mode. Fig. 3.4 shows the plots of these dispersion relations.

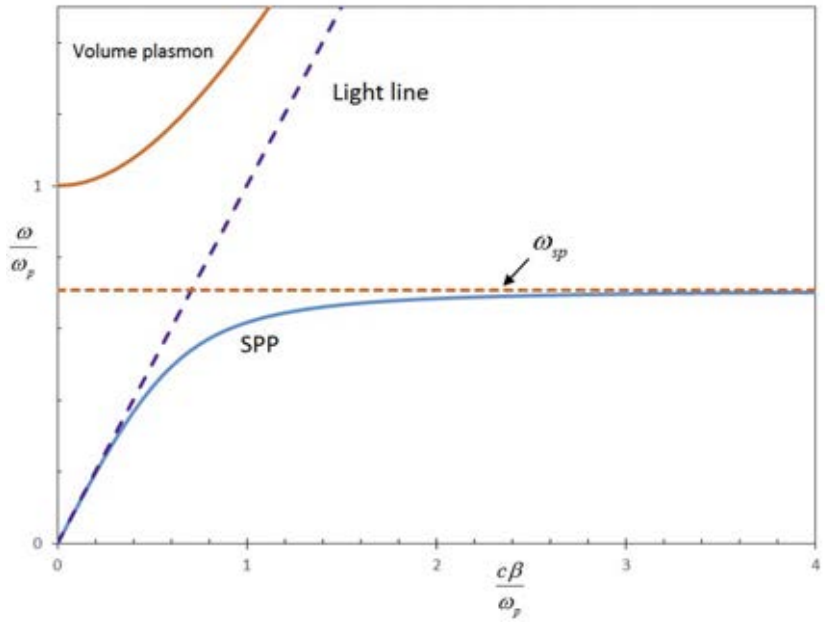

Figure 3.4: The dispersion relation of plasmon excitations in the lossless Drude metal-air system (solid line) and of light in air (dashed line).

Here, we focus on the surface mode dispersion relation since the upper branch is in the transparency regime discussed in chapter II. The SPPs line is on the right of the light line. Thus, the additional momentum is acquired to excite the SPPs. This can be done by the phase-matching techniques described in Ref.[59]. However, Elson and Ritchie found that photon can coupling to surface plasmon by introducing the surface roughness[60]. For the large wave number regime, The SPPs frequency approaches a specific value which is termed as surface plasmon frequency (ω_{sp}). For the Drude metal-air (or vacuum) system, ω_{p} is given by

$$\omega_{\mathrm{sp}} = \frac{\omega_{\mathrm{p}}}{\sqrt{2}}. \tag{3.19}$$

In this asymptotic limit of β, the SPPs group velocity $v_{\mathrm{g}}^{\mathrm{SPP}} \to 0$ as $\omega \to \omega_{\mathrm{SP}}$. Thus the SPPs acquire the localized (electrostatic) character whose properties can be described by the Laplace equation. SPP at ω_{SP} is also known as *surface plasmon*. This surface mode has a strong field concentration near the surface, as one can see in Fig. 3.3, since $\beta \to \infty$ as $\omega \to \omega_{\mathrm{SP}}$. Additionally, $l_1 \approx l_2 \approx \frac{1}{\beta}$ which implies that $k_1 \approx k_2$. This results can also be obtained by solving the Laplace equation and, then, applying the boundary conditions at the inter face. This is the case that in some limit the simpler method can yield approximately the same results as the more complicated method depending on the problem we are concerning with.

3.3 Localized surface plasmon resonance

In the preceding section, we have discussed the surface plasmon on the planar surface (interface). This structure support both propagating surface mode (SPP) and non-propagating surface mode which is known as localized surface plasmon (LSP). These excitations are due to the collective oscillations of the quasi-two dimensional conductive electrons at the metal surface, or metal-dielectric interface. Moreover, the quasi-one dimensional nanostructures such as metallic nanowires and nanotubes with small diameter can also support these two surface modes. In contrast, for more dimensional confinement structures, the quasi-zero dimensional structures which are called nanoparticles (NPs) or nanoclusters (NCs) support only the localized mode. Note that NPs that support SPs are also called plasmonic particles. This is due to the surface confinement of an electron gas. The collective displaced electrons experience the effective restoring force leading to the localized collective oscillations. Thus, the resonance can arise at the natural frequencies of the plasmonic particle. This resonance in called *localized surface plasmon resonance* (LSPR). For simplicity, we use the spherical particle to demonstrate this as in Fig. 3.5.

In contrast to the propagating surface mode, the localized mode can be excited directly by electromagnetic wave. Additionally, the resonance frequencies of Ag and Au nanoparticles are in the visible range of the electromagnetic wave. This resonance causes the enhancement of the light scattering and absorption resulting in the bright image of the nanoparticles. Fig. 3.6 shows the microscopic image of silver nanoparticles, for example. Moreover, the fields associated with LSPR are amplified, both inside and outside the particle, and highly concentrated near the particle surface. Generally, the LSPR frequencies are size, shape and

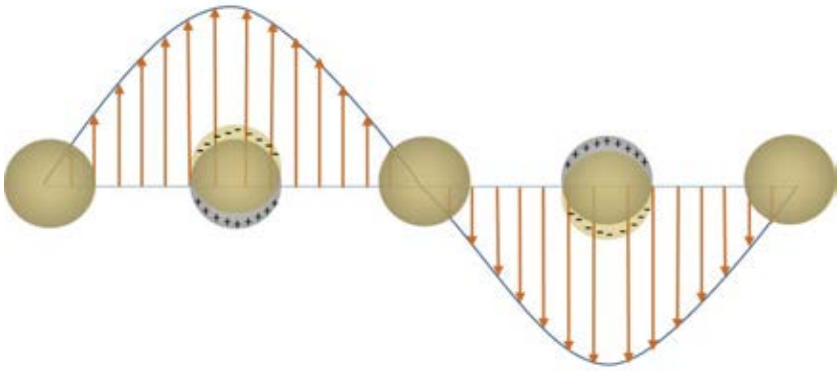

Figure 3.5: The localized collective oscillation at the spherical surface versus the external electromagnetic field.

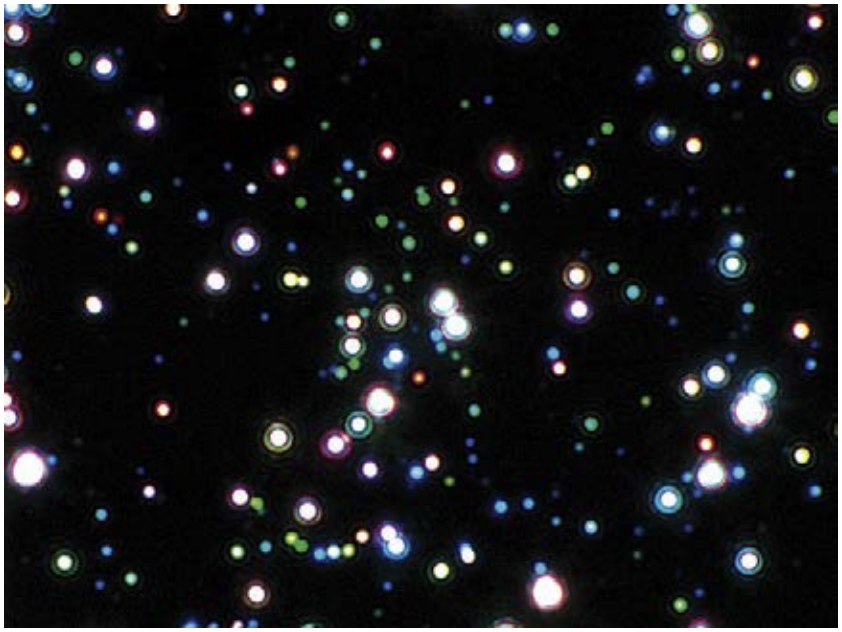

Figure 3.6: Dark-field optical image of light scatted from Ag nanoparticles [61].

dielectric environment dependent [62, 63, 64, 65, 66] as shown for examples in Fig. 3.7 and Fig. 3.8.

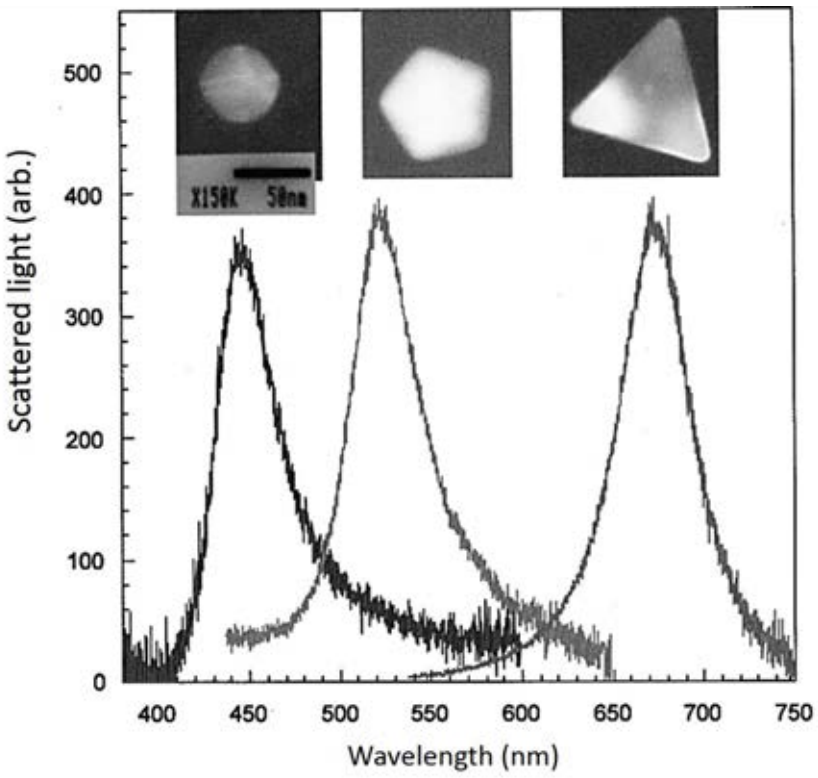

Figure 3.7: Dark-field scattering spectra of silver nanoparticles of different shapes [67].

The most interesting feature of LSPR is the coupling of plasmonic particles. The coupled LSPR can produce much more field enhancement than that of the isolated particle. These coupling effects will be discussed in detail in the next chapter. There are a number of different analytical and numerical methods for investigating the LSPR properties. For examples, Mie theory, quasistatic approximation, finite element, finite difference time-domain (FDTD), and discrete dipole approximation (DDA). In the following sections, we will investigate the LSPR properties using the first two methods since they can provide us with the underlying physical concepts at the analytical level.

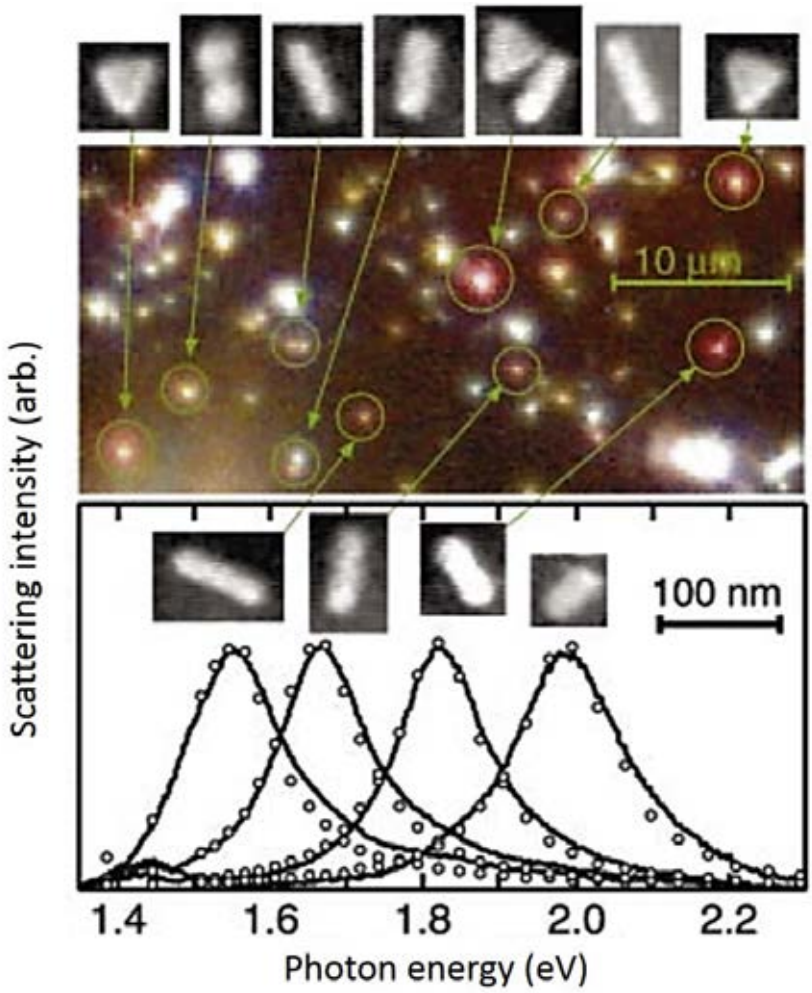

Figure 3.8: Dark-field image of different shapes and scattering spectra for different size of nanorods [68].

3.4 LSPR on a single sphere surface

3.4.1 Mie theory

In 1908, Gustav Mie developed the theory to explain the size dependent of the color of small colloidal gold particles suspended in water [69]. He obtained the general solutions for a plane electromagnetic wave scattering from and absorption by spherical particles. However, it was Ludvig Valentin Lorenz who was the first to analyze the problem of light scattered by a spherical particle in 1890 [70]. Therefore, the theory is also called Lorenz-Mie theory. However, the most common term is Mie theory and we will use this term to refer to it.

The theory is developed for the plane electromagnetic wave scattered by a homogeneous, isotropic sphere. Let us, now, consider the incident plane wave propagating in z direction scattered by a sphere of radius R and with (complex) refractive index n_s embedded in a nonabsorbing medium with refractive index n_0. According to Mie theory, the incident wave, scattered wave, and wave inside the particle can be expanded in vector spherical harmonics $\mathbf{N}_{omn}$,, $\mathbf{N}_{emn}$, $\mathbf{M}_{omn}$ and $\mathbf{M}_{emn}$ as the following expressions
incident wave:

$$\mathbf{E}_{\text{inc}} = E_0 \sum_{n=1}^{\infty} \frac{i^n(2n+1)}{n(n+1)} \left[\mathbf{M}_{on1}^{(1)}(k_0) - i\mathbf{N}_{en1}^{(1)}(k_0)\right], \tag{3.20a}$$

$$\mathbf{H}_{\text{inc}} = -\frac{k_0 E_0}{\omega\mu_0} \sum_{n=1}^{\infty} \frac{i^n(2n+1)}{n(n+1)} \left[\mathbf{M}_{en1}^{(1)}(k_0) + i\mathbf{N}_{on1}^{(1)}(k_0)\right], \tag{3.20b}$$

scattered wave:

$$\mathbf{E}_{\text{sca}} = -E_0 \sum_{n=1}^{\infty} \frac{i^n(2n+1)}{n(n+1)} \left[b_n\mathbf{M}_{on1}^{(1)}(k_0) - ia_n\mathbf{N}_{en1}^{(1)}(k_0)\right], \tag{3.21a}$$

$$\mathbf{H}_{\text{sca}} = \frac{k_0 E_0}{\omega\mu_0} \sum_{n=1}^{\infty} \frac{i^n(2n+1)}{n(n+1)} \left[a_n\mathbf{M}_{en1}^{(1)}(k_0) + ib_n\mathbf{N}_{on1}^{(1)}(k_0)\right], \tag{3.21b}$$

wave inside the particle:

$$\mathbf{E} = E_0 \sum_{n=1}^{\infty} \frac{i^n(2n+1)}{n(n+1)} \left[\beta_n\mathbf{M}_{on1}^{(1)}(k_0) - i\alpha_n\mathbf{N}_{en1}^{(1)}(k_0)\right], \tag{3.22a}$$

$$\mathbf{H} = -\frac{k_0 E_0}{\omega\mu_0} \sum_{n=1}^{\infty} \frac{i^n(2n+1)}{n(n+1)} \left[\alpha_n\mathbf{M}_{en1}^{(1)}(k_0) + i\beta_n\mathbf{N}_{on1}^{(1)}(k_0)\right], \tag{3.22b}$$

where a_n, b_n, α_n, and β_n are the expansion coefficients that are determined by the boundary conditions. k_0 and k are the wave numbers outside and inside the

sphere respectively. The details of the definition of the vector spherical harmonics are given in Ref. [56]. By applying the boundary conditions, i.e. the continuity of parallel components of **E** and **H**, the scattering coefficients are given by

$$a_n = \frac{\psi_n(x)\psi_n'(mx) - m\psi_n'(x)\psi_n(mx)}{\xi_n(x)\psi_n'(mx) - m\xi_n'(x)\psi(mx)}, \tag{3.23}$$

$$b_n = \frac{m\psi_n(x)\psi_n'(mx) - \psi_n'(x)\psi_n(mx)}{m\xi_n(x)\psi_n'(mx) - \xi_n'(x)\psi(mx)}, \tag{3.24}$$

where $\psi_n(x)$, $\xi_n(x)$, ψ_n', and $\xi_n'(x)$ are Riccati-Bessel functions and their derivatives with respect to the argument respectively. $m = \frac{n_s}{n_0}$ is the relative refractive index, and $x = k_0 R$. Note that the rigorous derivation of expansion coefficients can be found in Bohren and Huffman [56] text book. Even α_n and β_n are not expressed here. They have already been found simultaneously with a_n and b_n. Thus, the fields have completely been determined. One, then, can derive the expression for the extinction and scattering cross section as

$$\sigma_{\text{ext}} = \frac{2\pi}{k_0^2}\sum_{n=1}^{\infty}(2n+1)\text{Re}(a_n + b_n), \tag{3.25}$$

$$\sigma_{\text{sca}} = \frac{2\pi}{k_0^2}\sum_{n=1}^{\infty}(2n+1)(|a_n|^2 + |b_n|^2), \tag{3.26}$$

respectively. From Eq. 3.23 - Eq. 3.26, we obtain the resonance conditions for TM mode,

$$\frac{m\xi_n'(x)}{\xi_n(x)} = \frac{\psi_n'(mx)}{\psi_n(mx)}, \tag{3.27}$$

and for TE mode,

$$\frac{1}{m}\frac{\xi_n'(x)}{\xi_n(x)} = \frac{\psi_n'(mx)}{\psi_n(mx)}. \tag{3.28}$$

Eq. 3.27 and Eq. 3.28 valid for the sphere with any size and refractive index. But they are too complicated. We cannot analyze the resonant frequency from these equations analytically. Fortunately, in the limit $R \ll \lambda$ the Raccati-Bessel functions can be approximated by keeping only the first term of their series expansion. Consequently, the resonant conditions reduce to simple size-independent form as

$$\text{Re}[\varepsilon] = -\frac{n+1}{n}\varepsilon_0, \tag{3.29}$$

for TM mode, and

$$\text{Re}[\varepsilon] = \varepsilon_0, \tag{3.30}$$

for TE mode, where ε, ε_0 and n are dielectric function of the sphere, dielectric function of medium, and the multi pole under respectively, Obviously, Eq. 3.30 cannot be fullfilled. Hence, TE wave cannot couple to the LSPR in this limit.

Eq. 3.29 can also be derived by solving the Laplace equation (quasistatic approximation). Thus, the condition for the validity of the quasistatic approximation which will be discussed in the next section is provided by $R \ll \lambda$.

3.4.2 Quasistatic approximation

Mie theory is an exact electrodynamic solution for the absorption and scattering of light by a sphere. Nevertheless, in the limit $R \ll \lambda$ where R is the particle radius, the resonant conditions (Eq. 3.29 and Eq. 3.30) become particle size independent. This implies that the effect of field retardation over the particle can be neglected. More strictly speaking, the fields uniformly distribute over the particle and the distance not so far from the particle at an instance of time. This is the situation that can be described by the so called *quasistatic approximation*. There is an additional condition has to be fullfilled for the applicable of the quasistatic approximation. That is, the applying field frequency has to be much smaller than the conduction electron relaxation rate ($\omega \ll \frac{1}{\tau}$). The quasistatic approximation yields acceptable results in the range of frequencies from infrared to ultraviolet for typical metals with particle size approximately less than 100 nm. Additionally, more physical insight of the quasistatic approximation can be found in Landau and Lifshitz textbook [71]. The common way to achieve the quasistatic equations is by taking the limit $c \to \infty$ or equivalently $\frac{\partial \mathbf{B}}{\partial t} \to 0$ in the Maxwells equations. Hence, in quasistatic approximation, the problem reduces to solving Laplace equation. In addition, the alternative way for achieving the quasistatic equations by introducing electroquasistatic (EQS), magnetoquasstatic (MQS), and Darwin models have recent been discussed by Larsson [72]

Now, let us first investigate properties of quasistatic solution for a sphere with diectric function $\varepsilon(\omega)$ embedded in a nonabsorbing continuous medium with positive real dielectric constant ε_{m}. The system is placed in the uniform electric field $\mathbf{E}_0 = E_0\hat{z}$ as shown in Fig. 3.9.

In quasistatic approximation, we set $\frac{\partial B}{\partial t} = 0$. Consequently, $\nabla \times \mathbf{E} = 0$. We can define the scalar potential such that $\mathbf{E} = -\nabla\Phi$ and look for the solution of Laplace equation, $\nabla^2\Phi = 0$. The general solution of this problem is well-known and given in coordinates (r, θ), for azimuthal symmetry, by [73]

$$\Phi(r,\theta) = \sum_{l=0}^{\infty}[A_l r^l + B_l r^{-(l+1)}]P_l(\cos\theta), \tag{3.31}$$

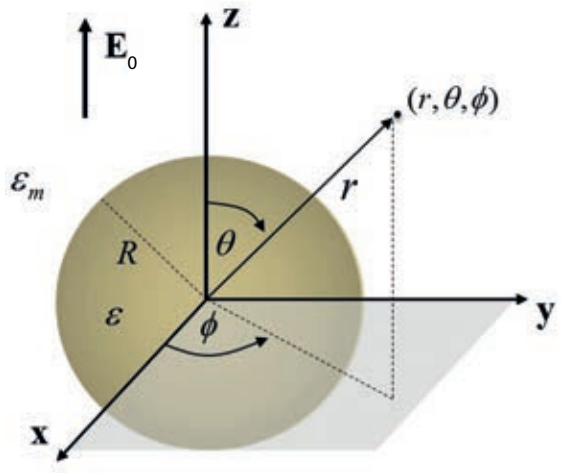

Figure 3.9: A system of the sphere with radius R and dielectric function ε embedded in the medium with dielectric constant $\varepsilon_{\rm m}$, and the applied field $\mathbf{E}_0$.

where $P_l(x)$ is Legrendre polynomial of integer order l. Note that Φ is ϕ-independent due to the azimuthal symmetry of the system. The solution is divided into two regions, i.e. inside and outside the sphere. Due to the finiteness of potential at the origin the potential inside the sphere is given by

$$\Phi_{\rm in}(r,\theta) = \sum_{l=0}^{\infty} A_l r^l P_l(\cos\theta), \tag{3.32}$$

whereas the potential outside the sphere is given by

$$\Phi_{\rm out}(r,\theta) = \sum_{l=0}^{\infty} [B_l r^l + C_l r^{-(l+1)}] P_l(\cos\theta). \tag{3.33}$$

By applying the following boundary conditions

$$(i) \qquad \Phi_{\rm out}(r,\theta) = -E_0 z, \quad \text{as} \quad r \to \infty,$$

$$(ii) \qquad \left.\frac{\partial \Phi_{\rm in}}{\partial \theta}\right|_{r=R} = \left.\frac{\partial \Phi_{\rm out}}{\partial \theta}\right|_{r=R}, \tag{3.34}$$

$$(iii) \qquad \varepsilon \left.\frac{\partial \Phi_{\rm in}}{\partial \theta}\right|_{r=R} = \varepsilon_{\rm m} \left.\frac{\partial \Phi_{\rm out}}{\partial \theta}\right|_{r=R}, \tag{3.35}$$

all arbitrary constants are fixed and the specific solutions are given by

$$\Phi_{\rm in}(r,\theta) = -\frac{3\varepsilon_{\rm m}}{\varepsilon + 2\varepsilon_{\rm m}} E_0 r\cos\theta, \tag{3.36}$$

$$\Phi_{\rm out}(r,\theta) = -E_0 r\cos\theta + \frac{\varepsilon - \varepsilon_{\rm m}}{\varepsilon + 2\varepsilon_{\rm m}} \frac{E_0 R^3 \cos\theta}{r^2}. \tag{3.37}$$

Furthermore, Eq. 3.37 can be rewritten in the following form

$$\Phi_{\rm out}(r,\theta) = -E_0 r\cos\theta + \frac{\mathbf{p}\cdot\mathbf{r}}{4\pi\varepsilon_0\varepsilon_{\rm m} r^3}. \tag{3.38}$$

Where $\mathbf{p} = 4\pi\varepsilon_0\varepsilon_\mathrm{m}R^3\frac{\varepsilon-\varepsilon_\mathrm{m}}{\varepsilon+2\varepsilon_\mathrm{m}}\mathbf{E}_0$ is the electric dipole moment. Hence, we can define the polarizability, α_e, such that

$$\mathbf{p} = 4\pi\varepsilon_0\varepsilon_\mathrm{m}\alpha_\mathrm{e}\mathbf{E}_0, \tag{3.39}$$

and

$$\alpha_\mathrm{e} = 4\pi R^3\frac{\varepsilon-\varepsilon_\mathrm{m}}{\varepsilon+2\varepsilon_\mathrm{m}}. \tag{3.40}$$

Now, we arrive at the resonant condition. That is,

$$\mathrm{Re}[\varepsilon] = -2\varepsilon_\mathrm{m}, \tag{3.41}$$

which is the Mie dipole ($n = 1$) resonance. From Eq. 3.36, Eq. 3.37, and $\mathbf{E} = -\nabla\Phi$, we can, now, evaluate the field enhancement factor at the particle surface as [55]

$$\left|\frac{E}{E_0}\right|_{r=R} \approx 3\frac{\mathrm{Re}[\varepsilon]}{\mathrm{Im}[\varepsilon]}. \tag{3.42}$$

By using the pointing-vector formulation, the scattering and absorption cross sections can be obtained as follows [59]

$$\sigma_\mathrm{sca} = \frac{8\pi}{3}k^4R^6\left|\frac{\varepsilon-\varepsilon_\mathrm{m}}{\varepsilon+2\varepsilon_\mathrm{m}}\right|^2, \tag{3.43}$$

$$\sigma_\mathrm{abs} = 4\pi kR^3\left|\frac{\varepsilon-\varepsilon_\mathrm{m}}{\varepsilon+2\varepsilon_\mathrm{m}}\right|, \tag{3.44}$$

where $k = \frac{\varepsilon_\mathrm{m}\omega}{c}$. As we have seen, the LSPR of the small metallic sphere is well described in a simple way. However, this treatment, uniform electronic field boundary condition, can only describe the dipole Mie LSPR. To investigate the resonance for all multipole order within quasistatic approximation, the uniform field boundary condition has to be replaced by the finiteness of field at infinity. Thus, the potentials inside and outside the sphere are given by

$$\Phi_\mathrm{in}(r,\theta,\phi) = \sum_{l=0}^{\infty}\sum_{m=-l}^{l}A_{l,m}r^lY_l^m(\theta,\phi), \tag{3.45}$$

$$\Phi_\mathrm{out}(r,\theta,\phi) = \sum_{l=0}^{\infty}\sum_{m=-l}^{l}B_{l,m}r^{-(l+1)}Y_l^m(\theta,\phi), \tag{3.46}$$

where $Y_l^m(\theta,\phi)$ is the spherical harmonic function. By applying the boundary conditions,

$$(i) \qquad \Phi_\mathrm{in}|_{r=R} = \Phi_\mathrm{out}|_{r=R}, \tag{3.47a}$$

$$(ii) \qquad \varepsilon\frac{\partial\Phi_\mathrm{in}}{\partial r}\bigg|_{r=R} = \varepsilon_\mathrm{m}\frac{\partial\Phi_\mathrm{out}}{\partial r}\bigg|_{r=R}, \tag{3.47b}$$

we obtain

$$\varepsilon = -\left(\frac{l+1}{l}\right)\varepsilon_{\mathrm{m}} \tag{3.48}$$

which is exactly the same as Mie result in the limit $\frac{R}{\lambda} \ll 1$. Hence, the LSPR dispersion relation for losses Drude Metal can be obtained by substituting Eq. 2.20 in to Eq. 3.48. That is,

$$\omega_{\mathrm{l}} = \omega_{\mathrm{p}}\sqrt{\frac{l}{l+(l+1)\varepsilon_{\mathrm{m}}}},$$

$\omega_{\infty} = \frac{\omega_{\mathrm{p}}}{\sqrt{2}} = \omega_{\mathrm{sp}}$ which is the surface frequency of the planar surface.

3.5 LSPR damping

There are two main processes that cause LSPRs decay in a definite life time. One is radiative damping. That releases the energy of coherent-collective electron oscillation into radiation. This process is dominant for large particle and causes the red shift of LSPR energy as the particle size increases. The another process is the non-radiative damping due to the electron-hole pair creations. The electron-hole pairs can be created from either the intraband transition within the conduction band or the interband transition from the d-bands (for nobel metal). This is responsible for the absorption and dominates for smaller particle size. The schematic interpretation of these two processes is shown in Fig. 3.10. For more details of

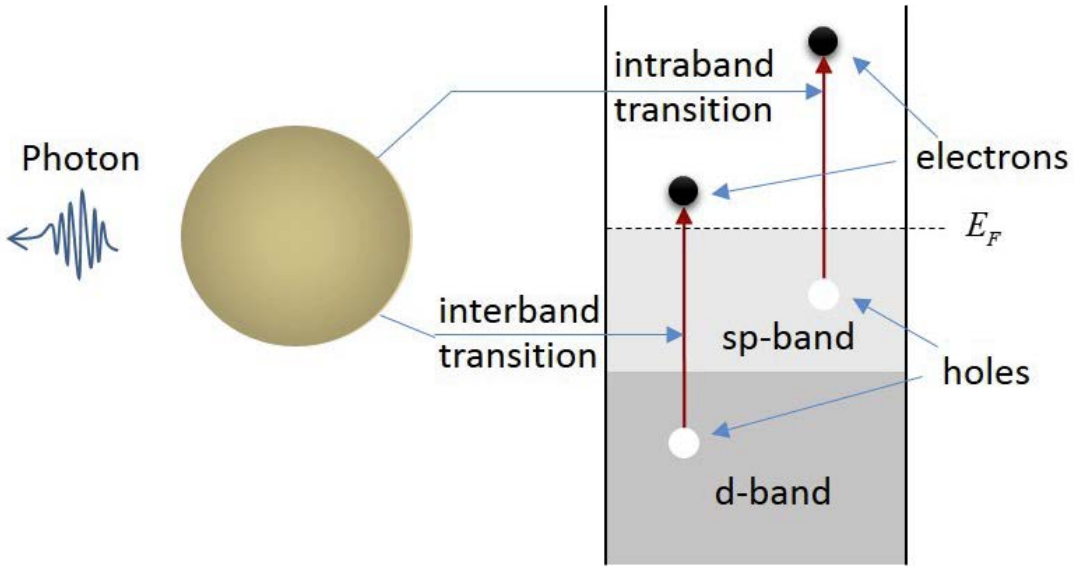

Figure 3.10: Schematic representation of decay processes. Left is the radiative decay and right is the non-radiative decay.

damping processes one can consult Ref.[74].

Chapter IV

Localized Surface Plasmon Resonance in Coupled Nanoparticles

In this chapter, we discuss the electromagnetic coupling between two Plasmon particles when they are in close proximity. If the interparticle distance is small enough, the individual plasmon particles start to interact with each other electromagnetically. This coupling can produce very large fields enhancement confined at the interparticle gap. Moreover, the coupling courses the shift of resonance frequency. The change in the resonance frequency, or in other word the LSPR energy, is a function of the particle separation distance and shape, size and material type of the constituent particles dependent. Fig.4.1 shows, for instance, the extinction spectra of dual gold nanodisks placed at various interparticle distances measured by Rechberger and co-workers [75]. Fig. 4.1(a) and Fig. 4.1(b) show extinction spectra when the polarization of the exciting field is parallel and perpendicular to the interparticles axis, respectively.

For the parallel polarization the resonant peaks shift to longer wavelength (red shift). For the parallel polarization, the peaks shift to shorter wavelength (blue shift). They described the shifts by the simple dipole model as shown in Fig.4.2. For the exciting field parallel to the interparticle axis, the opposite surface charges on the north pole of the bottom particle and on the south pole of the top particle experience the attractive interparticle force (Fig.4.2(a)). Thus, the internal restoring force of each particle is weakened resulting in the energy red shift. In contrast, for the perpendicular polarization, the surface charges on each particle act cooperative (Fig.4.2(b)) resulting in the enhancement of restoring force and energy blue shift.

This is a simple qualitative description of the interaction between the particles supporting LSPR.

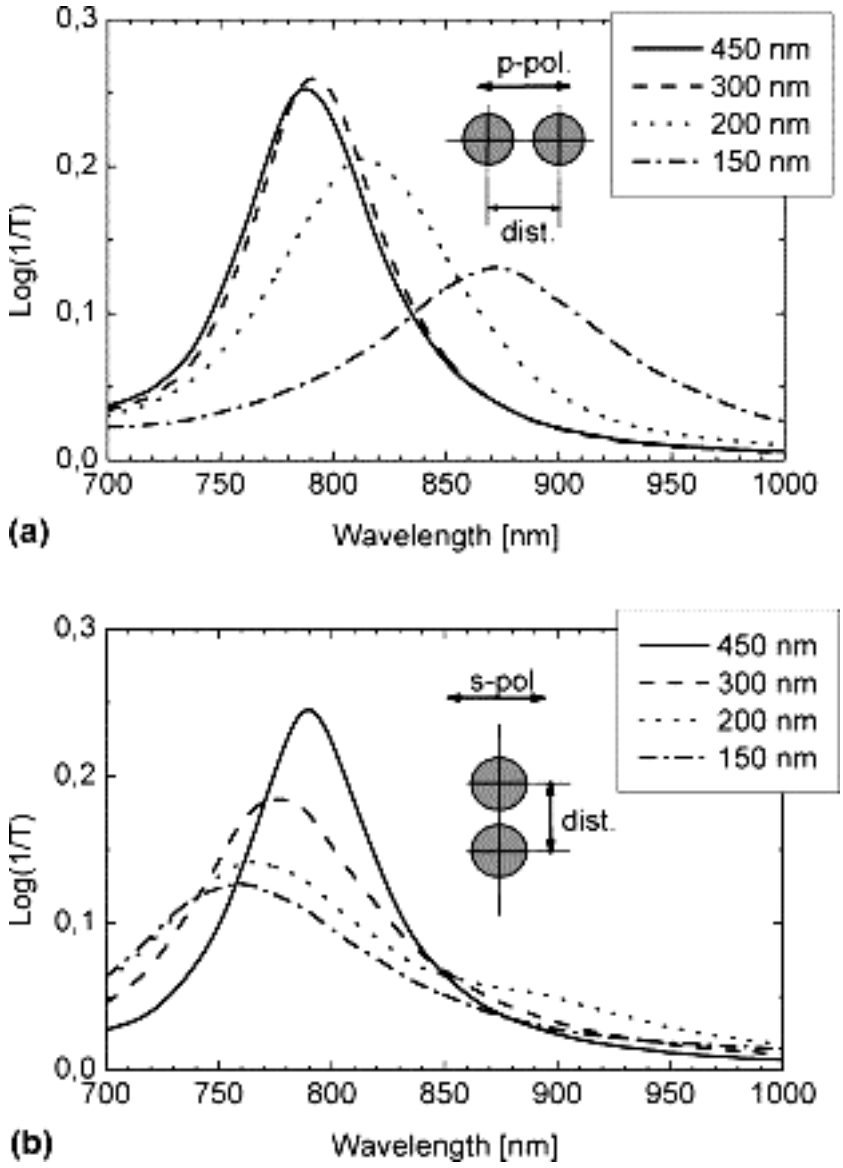

Figure 4.1: Experimental extinction ($\log(\frac{1}{T})$) spectra of gold nanodisk pair as a function of interparticle distance for the polarization of the exciting field (a) parallel, and (b) perpendicular to the interparticle axis [75].

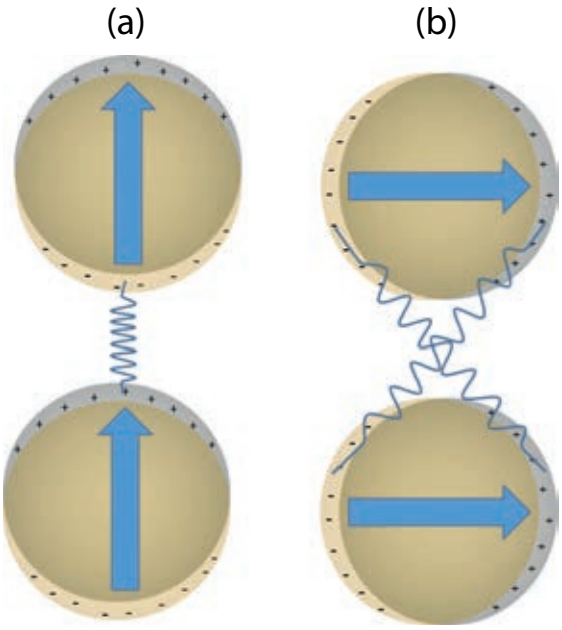

Figure 4.2: Simple dipole-dipole interaction model for exciting field polarization (a) parallel, and (b) perpendicular to interparticle axis.

4.1 LSPR hybridization

The quantitative model for description of the LSPR is hybridization model [37]. In this model, the LSPR frequencies of complex structure are the consequences of the hybridization of LSPR modes of each individual particle analogous to the hybridization of the molecular orbital. The hybridization results in two hybridization modes. One is the lower energy mode called *bonding* mode. The other is the higher energy mode called *antibonding* mode. The schematic representation of the hybridization of the single shell nanostructure is shown in Fig. 4.3. The LSPR modes of the nanoshell are resulting from the hybridization of the sphere surface plasmons and cavity surface plasmons. Similar, the hybridization of a more complex nanoshell structure associated with its hybridization modes is schematically shown in Fig. 4.4. Here, we briefly discuss this model. The detail of calculation can be found elsewhere [37, 38, 39].

4.2 Coupled LSPR in a nanosphere pair : quasistatic approximation

In this dissertation we focus on the effects of symmetry breaking to LSPR energy within the quasistatic regime. That is, the particle size is approximately be-

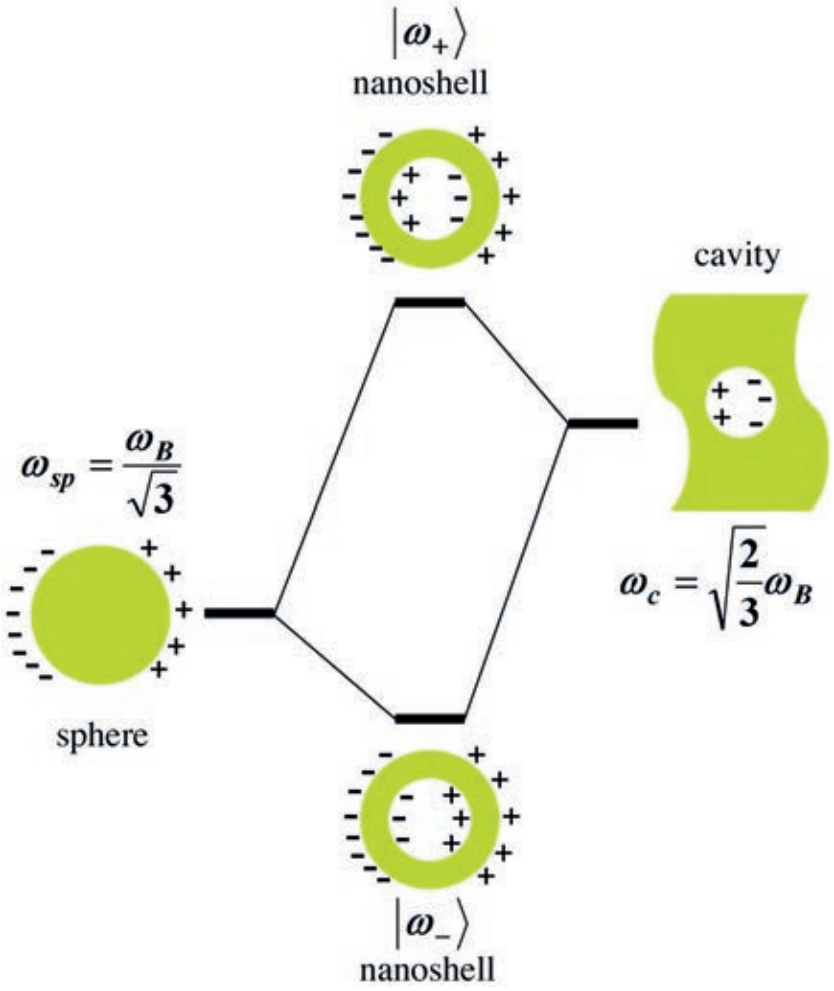

Figure 4.3: The hybridization of sphere surface plasmons and cavity surface plasmons results in the LSPR modes of the shell [37].

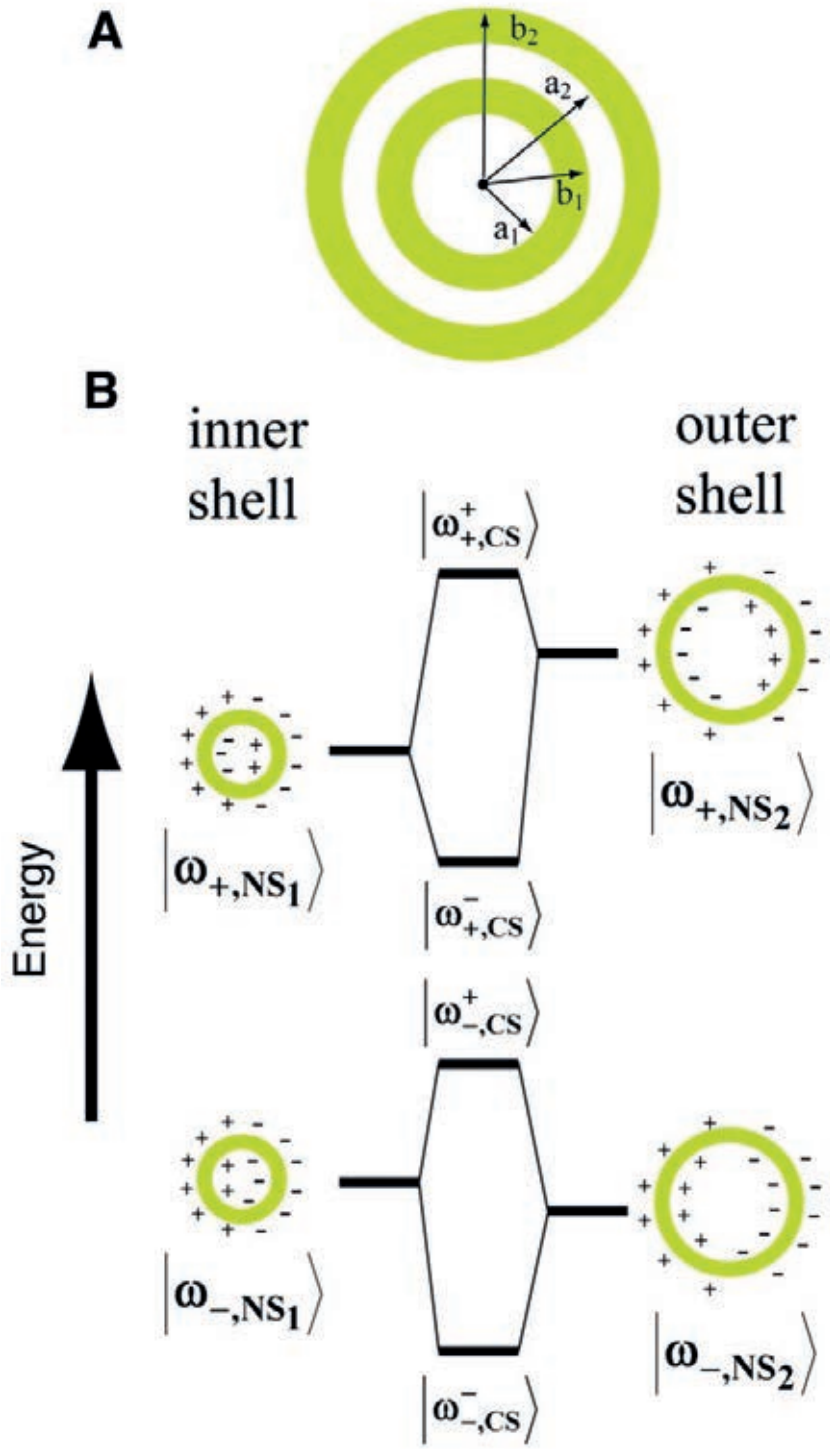

Figure 4.4: The hybridization modes of two concentric shell nanostructure [37].

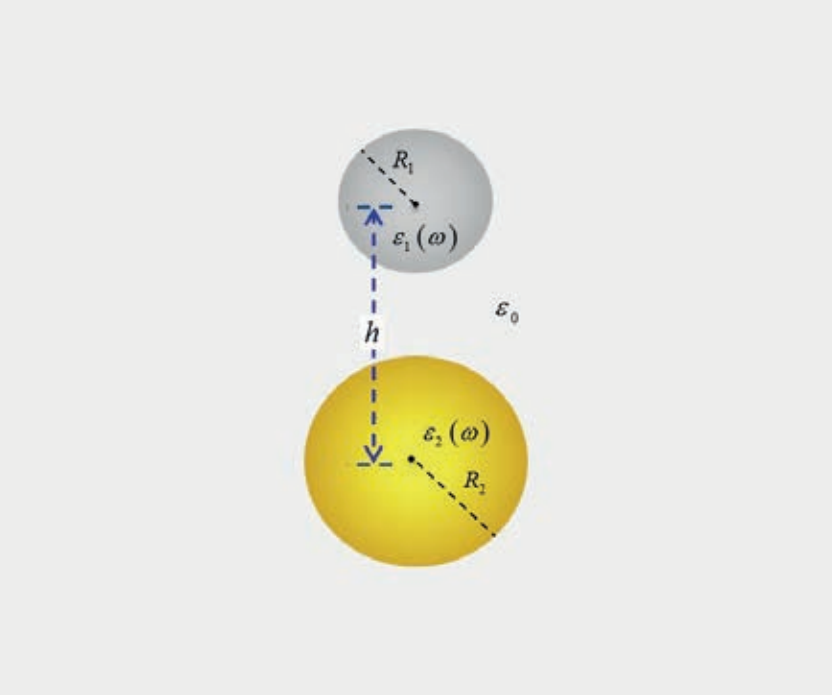

Figure 4.5: The sphere with radius R_1 and dielectric function ε_1 placed at the center-to-center distance h from there with R_2 and dielectric function ε_2. The pair of spheres is immersed in the continuous medium with positive dielectric constant ε_0.

tween 10 nm to 100 nm. To investigate the resonant frequency at a given system configuration, we start with the description of the system configuration, system parameters and the coordinate system used in the calculation. Then, we look for the solution of Laplace equation in this coordinate system and apply the boundary conditions at the sphere surfaces. Next, by introducing the matrix formulation, we derive the general resonant condition. Finally we calculate the resonant frequencies for two identical lossless Drude spheres. The effect of symmetry breaking will be discussed in the next chapter.

4.2.1 System parameters

The system under consideration composes of a pair of spheres with radius R_1, R_2 and dielectric function ε_1, ε_2, respectively. The pair is immersed in a nonabsorbing continuous medium with dielectric function ε_0 at a center-to-center distance h. We assume that ε_0 is a positive constant.The illustration of the system is shown in Fig. 4.5. There are the additional conditions on the separation distance for validity of quasistatic theory in our case. The separation distance must be (i) substantially larger than interatomic distance, and (ii) smaller than optical wavelength. In the

case that the separation distance is comparable to the interatomic distance the effect of quantum nonlocality has to be taken into account [76, 77]. In the case that the separation distance is comparable to or larger than the optical wavelength the retardation effect becomes important. Next, let us introduce the coordinate system used for solving the Laplace equation. From the geometry of the system, it is convenient to use the bispherical coordinates (γ, η, ϕ) defined by following expressions:

$$x = \frac{a\sin(\eta)\cos(\phi)}{\cosh(\gamma) - \cos(\eta)}, \tag{4.1a}$$

$$y = \frac{a\sin(\eta)\sin(\phi)}{\cosh(\gamma) - \cos(\eta)}, \tag{4.1b}$$

$$z = \frac{a\sinh(\gamma)}{\cosh(\gamma) - \cos(\eta)}, \tag{4.1c}$$

(see appendix A for more details). In this coordinate system a sphere surface is the surface of constant γ, i.e. $\gamma =$ constant. The surface of sphere i can be expressed in terms of the system parameters as follows:

$$\gamma_i = \ln(\tilde{a}_i + \sqrt{\tilde{a}_i^2 + 1}), \tag{4.2}$$

and

$$\tilde{a}_i = \frac{1 + \alpha^{3-2i}}{2\xi}\sqrt{(\xi^2 - 1)\left[\xi^2 - \left(\frac{\alpha - 1}{\alpha + 1}\right)^2\right]}, \tag{4.3}$$

for $i = 1, 2$, where dimensionless parameters $\alpha = \frac{R_2}{R_1}$, and $\xi = \frac{h}{R_1 + R_2}$ are a particle size ratio and a scaled separation distance respectively. Note that $\gamma_i > 0$.

4.2.2 Surface mode resonance

As mentioned that in quasistatic regime the surface mode resonant condition can be obtained by solving the Laplace equation, $\nabla^2\Phi = 0$, for scalar potential and then applying the appropriate boundary conditions. By using the separation of variable technique, the general solution of Laplace equation in bispherical coordinates is given by [78, 79]

$$\Phi(\mathbf{r}) \propto \sqrt{\cosh\gamma - \cos\eta}\, e^{\pm(n+\frac{1}{2})\gamma} P_n^m(\cos\eta) e^{\pm im\phi}, \tag{4.4}$$

where $P_n^m(x)$ is the associated Legrendre polynomial. Since there are two boundary surfaces, then the whole space can be divided into three regions as shown in Fig. 4.6. The potential in each region is given by the following expressions:

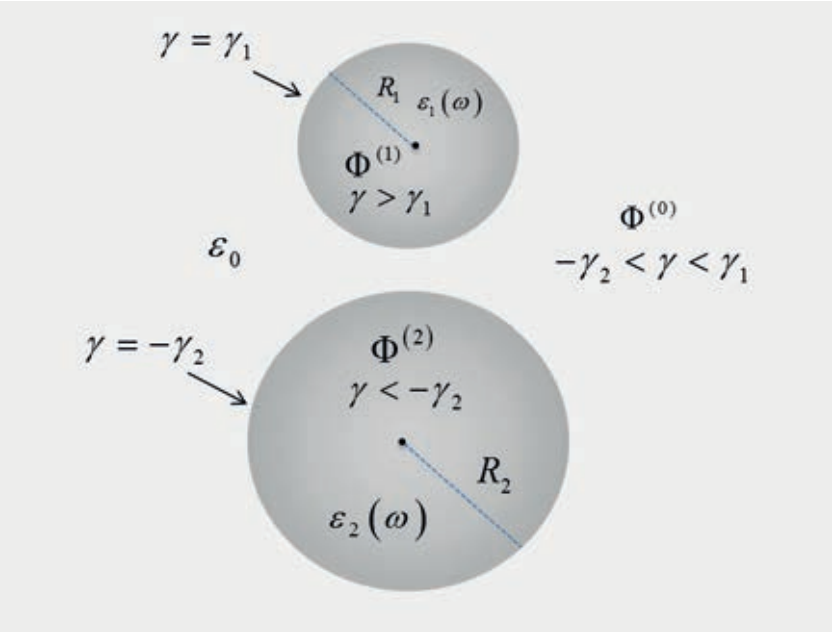

Figure 4.6: Three regions of space, boundary surfaces and potential associated with each region.

(i) In sphere 1 ($\gamma > \gamma_1$),

$$\Phi^{(1)}(\mathbf{r}) = \sqrt{\cosh\gamma - \cos\eta}\sum_{n,m} A_{nm} e^{-\left(n+\frac{1}{2}\right)\gamma} P_n^m\left(\cos(\eta)\right) e^{im\phi}, \tag{4.5}$$

(ii) In the medium ($-\gamma_2 < \gamma < \gamma_1$)

$$\Phi^{(0)}(\mathbf{r}) = \sqrt{\cosh\gamma - \cos\eta}\sum_{n,m}\left[C_{nm} e^{\left(n+\frac{1}{2}\right)\gamma} + D_{nm} e^{-\left(n+\frac{1}{2}\right)\gamma}\right] P_n^m\left(\cos(\eta)\right) e^{im\phi}, \tag{4.6}$$

(iii) In sphere 2 ($\gamma < -\gamma_2$)

$$\Phi^{(2)}(\mathbf{r}) = \sqrt{\cosh\gamma - \cos\eta}\sum_{n,m} B_{nm} e^{\left(n+\frac{1}{2}\right)\gamma} P_n^m\left(\cos(\eta)\right) e^{im\phi}. \tag{4.7}$$

The mode $\pm m$ are degenerate due to the azimuthal symmetry of the system. We need not concern with the negative m mode since the negative order associated Legendre polynomial can be related to the positive one by the relation [80]

$$P_n^{-m}(x) = (-1)^m \frac{(n+m)!}{(n-m)!} P_n^m(x). \tag{4.8}$$

We then apply the following boundary conditions

$$\Phi^{(1)}(\mathbf{r})\big|_{\gamma=\gamma_1} = \Phi^{(0)}(\mathbf{r})\big|_{\gamma=\gamma_1}, \Phi^{(2)}(\mathbf{r})\big|_{\gamma=-\gamma_2} = \Phi^{(0)}(\mathbf{r})\big|_{\gamma=-\gamma_2}, \tag{4.9}$$

and

$$\varepsilon_1 \frac{\partial \Phi^{(1)}(\mathbf{r})}{\partial \gamma}\bigg|_{\gamma=\gamma_1} = \varepsilon_0 \frac{\partial \Phi^{(0)}(\mathbf{r})}{\partial \gamma}\bigg|_{\gamma=\gamma_1}, \varepsilon_2 \frac{\partial \Phi^{(2)}(\mathbf{r})}{\partial \gamma}\bigg|_{\gamma=-\gamma_2} = \varepsilon_0 \frac{\partial \Phi^{(0)}(\mathbf{r})}{\partial \gamma}\bigg|_{\gamma=-\gamma_2}. \tag{4.10}$$

By performing a lengthy algebraic manipulation, we obtain two recurrence equations for the expansion coefficients as

$$\begin{aligned}
&\varepsilon_1 \Big((n-m)c^{(1)}_{n-1,m} + [\sinh(\gamma_1) - (2n+1)\cosh(\gamma_1)]c^{(1)}_{n,m} + (n+m+1)c^{(1)}_{n+1,m} \\
&\quad +(n-m)d^{(1)}_{n-1,m} + [\sinh(\gamma_1) - (2n+1)\cosh(\gamma_1)]d^{(1)}_{n,m} + (n+m+1)d^{(1)}_{n+1,m}\Big) \\
&= \varepsilon_0 \Big(-(n-m)c^{(1)}_{n-1,m} + [\sinh(\gamma_1) + (2n+1)\cosh(\gamma_1)]c^{(1)}_{n,m} - (n+m+1)c^{(1)}_{n+1,m} \\
&\quad +(n-m)d^{(1)}_{n-1,m} + [\sinh(\gamma_1) - (2n+1)\cosh(\gamma_1)]d^{(1)}_{n,m} + (n+m+1)d^{(1)}_{n+1,m}\Big),
\end{aligned} \tag{4.11}$$

and

$$\begin{aligned}
&\varepsilon_2 \Big((n-m)c^{(2)}_{n-1,m} + [\sinh(\gamma_2) - (2n+1)\cosh(\gamma_2)]c^{(2)}_{n,m} + (n+m+1)c^{(2)}_{n+1,m} \\
&\quad +(n-m)d^{(2)}_{n-1,m} + [\sinh(\gamma_2) - (2n+1)\cosh(\gamma_2)]d^{(2)}_{n,m} + (n+m+1)d^{(2)}_{n+1,m}\Big) \\
&= \varepsilon_0 \Big((n-m)c^{(2)}_{n-1,m} + [\sinh(\gamma_2) - (2n+1)\cosh(\gamma_2)]c^{(2)}_{n,m} + (n+m+1)c^{(2)}_{n+1,m} \\
&\quad -(n-m)d^{(2)}_{n-1,m} + [\sinh(\gamma_2) + (2n+1)\cosh(\gamma_2)]d^{(2)}_{n,m} - (n+m+1)d^{(2)}_{n+1,m}\Big),
\end{aligned} \tag{4.12}$$

where

$$c^{(i)}_{n,m} = C_{n,m} e^{(-1)^{i+1}(n+\frac{1}{2})\gamma_i}, \tag{4.13}$$

and

$$d^{(i)}_{n,m} = D_{n,m} e^{(-1)^{i}(n+\frac{1}{2})\gamma_i}, \tag{4.14}$$

for $i = 1, 2$. The coefficient $c^{(i)}_{n,m}$ and $d^{(i)}_{n,m}$ are related to the coefficients of the potential inside the spheres by

$$A_{n,m} e^{-\left(n+\frac{1}{2}\right)\gamma_1} = c^{(1)}_{n,m} + d^{(1)}_{n,m}, \tag{4.15}$$

and

$$B_{n,m} e^{-\left(n+\frac{1}{2}\right)\gamma_2} = c^{(2)}_{n,m} + d^{(2)}_{n,m}. \tag{4.16}$$

It is important to note that in the algebraic calculation step we employ the recurrence relation for derivative of the associated Legendre polynomials (see appendix B). One can see that Eq. 4.11 and Eq. 4.12 form a system of infinite coupled linear equations. However, in practice, the number of equations is truncated at a specific value, N, depending on the convergence of the solution. It is appropriate to deal with the system of linear equation by using the matrix formulation as will be discussed in the next section.

4.2.3 Matrix calculation

We introduce, here, the vector and matrix notations. We define the vector notations as

$$\mathbf{c}_i = \begin{pmatrix} c_1^{(i)} \\ c_2^{(i)} \\ c_3^{(i)} \\ \vdots \end{pmatrix} \quad \text{and} \quad \mathbf{d}_i = \begin{pmatrix} d_1^{(i)} \\ d_2^{(i)} \\ d_3^{(i)} \\ \vdots \end{pmatrix} \quad \text{for } i = 1, 2. \tag{4.17}$$

and the relevant matrices are defined by their elements as follows:

$$[\mathbf{\Lambda}]_{ij} = e^{-(m+i-\frac{1}{2})(\gamma_1+\gamma_2)}\delta_{i,j}, \tag{4.18}$$

$$\left[\mathbf{\Lambda^{-1}}\right]_{ij} = e^{(m+i-\frac{1}{2})(\gamma_1+\gamma_2)}\delta_{i,j}, \tag{4.19}$$

$$(\mathbf{\Sigma}_k)_{ij} = (i-1)\delta_{i,j+1} - [2(m+i)-1]\cosh(\gamma_k)\delta_{i,j} + (2m+i)\delta_{i,j-1}, \tag{4.20}$$

and

$$\mathbf{\Gamma}_i = \sinh(\gamma_i)\mathbb{1} + \mathbf{\Sigma}_i \qquad \text{for} \qquad i = 1, 2, \tag{4.21}$$

By using these matrices and vectors, Eq. 4.11 and Eq. 4.12 can be rewritten in the matrix form as

$$(\lambda_1\mathbf{\Gamma}_1 + 2\mathbf{\Sigma}_1)\cdot\mathbf{c}_1 + \lambda_1\Gamma_1\cdot\mathbf{d}_1 = 0, \tag{4.22a}$$

$$\lambda_2\mathbf{\Gamma}_2\cdot\mathbf{c}_2 + (\lambda_2\mathbf{\Gamma}_2 + 2\mathbf{\Sigma}_2)\cdot\mathbf{d}_2 = 0, \tag{4.22b}$$

where

$$\lambda_i = \frac{\varepsilon_i}{\varepsilon_0} - 1. \tag{4.23}$$

One can see from Eq. 4.13 and Eq. 4.14 that the coefficient $c_{n,m}^{(1)}(d_{n,m}^{(1)})$ and $c_{n,m}^{(2)}(d_{n,m}^{(2)})$ are not linearly independent. They are related to each other by

$$c_{n,m}^{(2)} = e^{-(n+\frac{1}{2})(\gamma_1+\gamma_2)}c_{n,m}^{(1)} \text{ and } d_{n,m}^{(2)} =^{(n+\frac{1}{2})(\gamma_1+\gamma_2)} d_{n,m}^{(1)}, \tag{4.24}$$

or in vector forms as

$$\mathbf{c}_2 = \mathbf{\Lambda}\cdot\mathbf{c}_1 \text{ and } \mathbf{d}_2 = \mathbf{\Lambda}^{-1}\cdot\mathbf{d}_1. \tag{4.25}$$

Substituting Eq. 4.25 into Eq. 4.22b yields

$$(\lambda_1\mathbf{\Gamma}_1 + 2\mathbf{\Sigma}_1)\cdot\mathbf{c}_1 + \lambda_1\mathbf{\Gamma}_1\cdot\mathbf{d}_1 = 0, \tag{4.26a}$$

$$\lambda_2\mathbf{\Gamma}_2\mathbf{\Lambda}\cdot\mathbf{c}_1 + (\lambda_2\mathbf{\Gamma}_2 + 2\mathbf{\Sigma}_2)\mathbf{\Lambda}^{-1}\cdot\mathbf{d}_1 = 0, \tag{4.26b}$$

By multiplying Eq. 4.26b by λ_1 and substituting $\mathbf{d}_1$ from Eq. 4.26a into Eq. 4.26b, we obtain

$$[(\lambda_2\mathbf{\Gamma}_2 + 2\mathbf{\Sigma}_2)\mathbf{\Lambda}^{-1}(\lambda_1\mathbf{\Gamma}_1 + 2\mathbf{\Sigma}_1) - \lambda_1\lambda_2\mathbf{\Gamma}_2\mathbf{\Lambda}\mathbf{\Gamma}_1]\cdot\tilde{\mathbf{c}}_1 = 0, \tag{4.27}$$

where $\tilde{\mathbf{c}} = \mathbf{\Gamma}_1^{-1} \cdot \mathbf{c}_1$. Eq. 4.27 is the nonlinear eigenvalue problem (NLEVP) (see appendix C for definition). The nontrivial solutions exist for only a set of discrete frequencies, i.e. resonant frequencies, which are eigenvalues of Eq. 4.27. By performing some algebra, the condition for resonant frequency is given by

$$\Big|\mathbf{H}(\omega) + \delta\mathbf{H}(\omega),\Big| = 0, \tag{4.28}$$

where

$$\mathbf{H} = [\lambda_2(\omega)\mathbf{\Gamma}_2(\mathbb{1} \pm \mathbf{\Lambda}) + 2\mathbf{\Sigma}_2][\lambda_1(\omega)(\mathbb{1} \mp \mathbf{\Lambda})\tilde{\mathbf{\Gamma}}_1 + 2\tilde{\mathbf{\Sigma}}_1], \tag{4.29a}$$

$$\delta\mathbf{H} = \pm 2[\lambda_1(\omega)\mathbf{\Sigma}_2\mathbf{\Lambda}\tilde{\mathbf{\Gamma}}_\mathbf{1} - \lambda_2(\omega)\mathbf{\Gamma}_2\mathbf{\Lambda}\tilde{\mathbf{\Sigma}}_\mathbf{1}]. \tag{4.29b}$$

Note that the commutation relation $[\mathbf{\Gamma}_i, \mathbf{\Sigma}_j] = 0$ if $\gamma_i = \gamma_j$, and $\tilde{\mathbf{A}} = \mathbf{\Lambda}^{-1}\mathbf{A}\mathbf{\Lambda}$. Alternatively, Eq. 4.28 can be obtained by writing Eq. 4.26 in the block form as [81]

$$\begin{bmatrix} \lambda_1\mathbf{\Gamma}_\mathbf{1} + 2\mathbf{\Sigma}_\mathbf{1} & \lambda_1\mathbf{\Gamma}_\mathbf{1} \\ \lambda_2\mathbf{\Gamma}_\mathbf{2}\lambda & \lambda_2\mathbf{\Gamma}_\mathbf{2} + 2\mathbf{\Sigma}_\mathbf{2} \end{bmatrix} \begin{bmatrix} \mathbf{c}_\mathbf{1} \\ \mathbf{d}_\mathbf{1} \end{bmatrix} = 0, \tag{4.30}$$

which exactly yields Eq. 4.28.

The main result is Eq. 4.28 which is the general condition for the surface mode resonant of two spheres system. The class of matrix polynomial in Eq. 4.27 depends on the form of dielectric function. Therefore, this condition can be applied for any material with spherical shape that the dielectric function is known. For simplicity, we used the Drude model with the assumption that $\omega\tau \ll 1$ to calculate the LSPR energy. For Drude metallic spheres in vacuum, $\lambda_i = -\frac{\omega_{\mathrm{p}_i}^2}{\omega^2}$ when ω_{p_i} is plasma frequency of sphere i.

4.2.4 LSPR coupling in a symmetric pair

In this chapter we discuss the LSPR coupling in symmetric sphere pair only. The effects of symmetry breaking will be discussed in chapter V. In case of a symmetric pair, $\delta H(\omega) = 0$. Thus, the NLEVP reduces to the generalized eigenvalue problem (GEP) with the resonant condition given by

$$|\lambda\mathbf{\Gamma}(\mathbb{1} \pm \mathbf{\Lambda}) + 2\mathbf{\Sigma}| = 0. \tag{4.31}$$

Obviously, from Eq. 4.31, there are two families of solutions. One is a set of the solutions of $|\lambda\mathbf{\Gamma}(\mathbb{1} - \mathbf{\Lambda}) + 2\mathbf{\Sigma}| = 0$. The LSPR energies of this mode

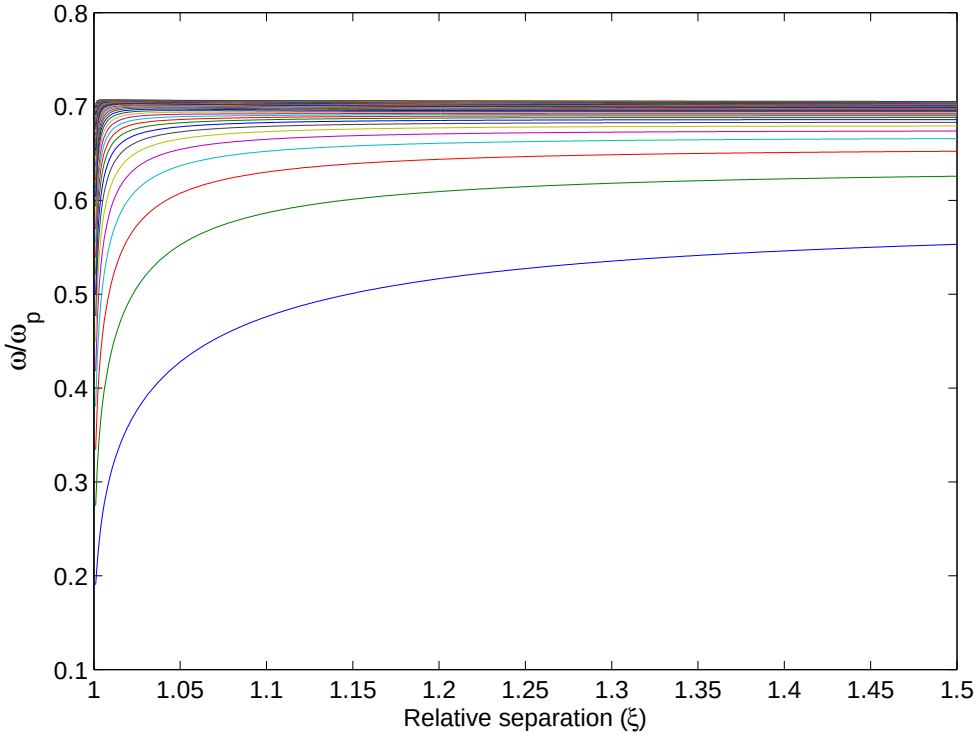

Figure 4.7: Normalized LSPR energies as a function of scaled separation distance. These are all eigenvalues of $|\lambda\mathbf{\Gamma}(\mathbb{1}-\mathbf{\Lambda})+2\mathbf{\Sigma}|=0$ which decrease with decreasing ξ (bonding mode).

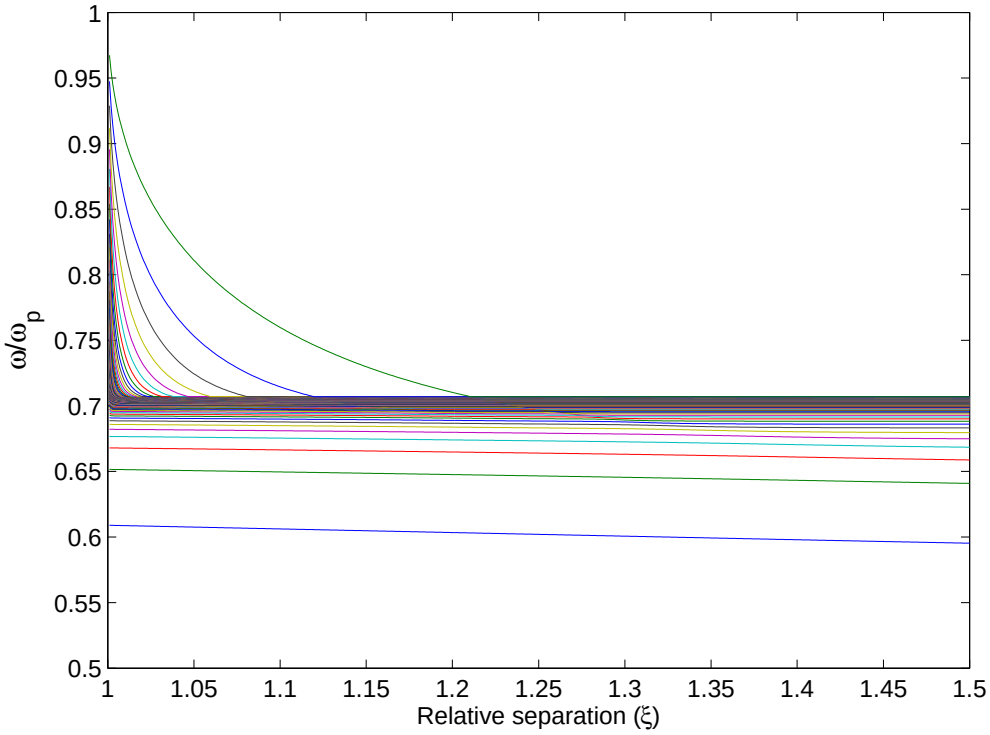

Figure 4.8: Normalized LSPR energies as a function of scaled separation distance. These are all eigenvalues of $|\lambda\mathbf{\Gamma}(\mathbb{1}+\mathbf{\Lambda})+2\mathbf{\Sigma}|=0$ which increase with decreasing ξ (antibonding mode).

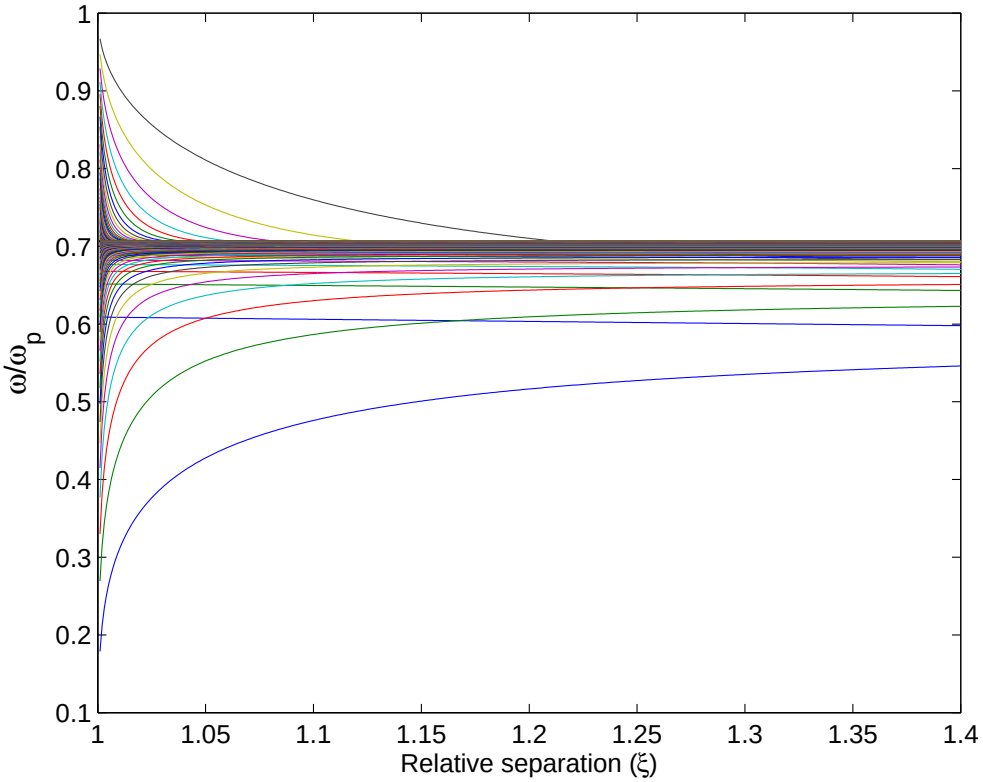

Figure 4.9: Combined bonding and antibonding modes.

decrease as the separation distance decrease as shown in Fig. 4.7. The other set of solutions corresponds to the condition $|\lambda\mathbf{\Gamma}(\mathbb{1}+\mathbf{\Lambda})+2\mathbf{\Sigma}|=0$. The LSPR energies of this mode increase as the separation distance decreases as shown in Fig. 4.8. To characterize these two modes, we follow the physical meaning of the mode given by Ng et al [27] that mode with *positive(negative) slope* is a *bonding (antibonding)* mode since it induces the attractive (repulsive) optical force. By this meaning the first solutions are the bonding modes and the latter are the antibonding modes. This mode characterization is consistent with the plasmon hybridization model [38]. To compare the energies of these two modes, Fig. 4.7 and 4.8 are combined. The combined figure is shown in Fig. 4.9. In this figure, one can see that at large separation distance both bonding and antibonding converge to particular constants. These values are the single sphere LSPR energies, $\omega_l = \omega_{\mathrm{p}}\sqrt{\frac{l}{2l+1}}$. To make this clearer, we extract the lowest and highest energies of both bonding and antibonding modes as shown in Fig. 4.10. Obviously, when the particles get close enough the interaction is turned on resulting in the energy splitting into two branches, i.e. bonding and antibonding. As we can see in Fig. 4.10, the low energy bonding and high energy antibonding modes have stronger interaction and more

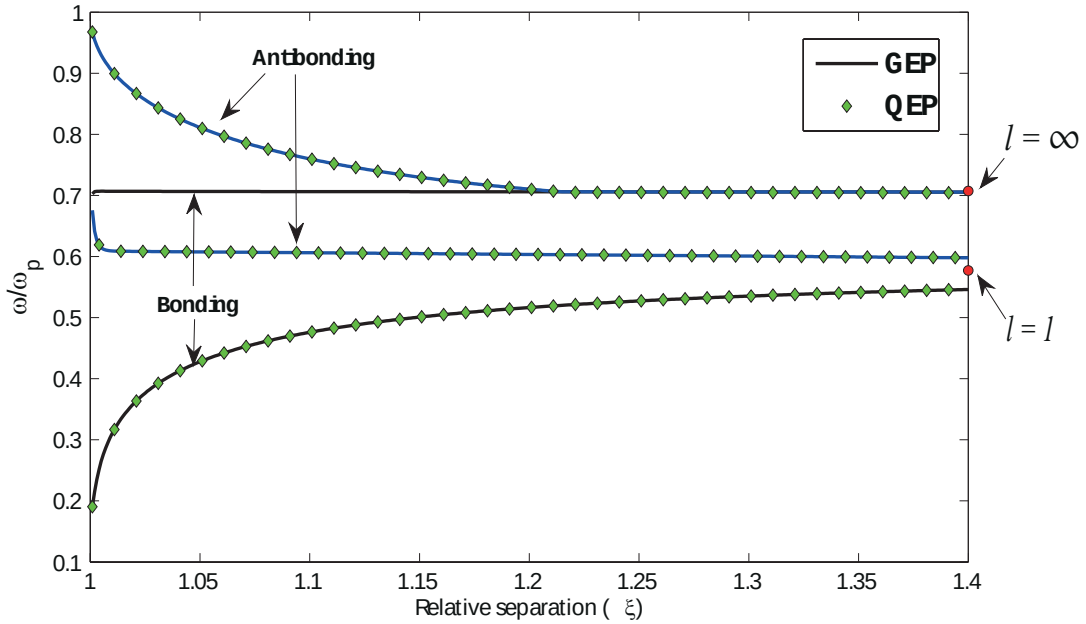

Figure 4.10: Lowest and highest LSPR energy of bonding (black) and antibonding (blue) modes. The red dots indicate the lowest ($l = 1$) and higest ($l = \infty$) LSPR energies of the single sphere. The green diamonds indicate the LSPR energies obtained from QEP method.

sensitive to the change of separation distance than the high energy bonding and low energy antibonding modes. Additionally, we also solve this problem by means of the NLEVP. In this sample case, the NLEVP reduces to the so called quadratic eigenvalue problem (QEP)(see appendix C) in the form $Q(\omega)\tilde{\mathbf{c}} = 0$ where

$$Q(\omega) = (2\omega^2)^2\boldsymbol{\Sigma_2}\tilde{\boldsymbol{\Sigma}}_\mathbf{1} - 2\omega^2)(\omega_{\mathrm{p}_1}^2\boldsymbol{\Sigma_2}\tilde{\boldsymbol{\Gamma}}_\mathbf{1} + \omega_{\mathrm{p}_2}^2\boldsymbol{\Gamma_2}\tilde{\boldsymbol{\Gamma}}_\mathbf{1}) + \boldsymbol{\Gamma_2}(\mathbf{1} - \boldsymbol{\Lambda}^2)\tilde{\boldsymbol{\Gamma}}_\mathbf{1}. \qquad (4.32)$$

The QEP is solved by the linearization method [85] and the results are indicated by the green diamonds in Fig. 4.10. From the figure, the results of QEP which is used for the case of an asymmetric pair, completely agree with those of GEP method.

Chapter V

Symmetry breaking in coupled-localized surface plasmon resonance

In the preceding chapter, we have discussed the LSPR energy of the symmetric sphere pair. In such system the coupling causes the energy splitting into two branches, the bonding and antibonding mode. In this chapter, we discuss the effects of symmetry breaking to these two energy modes. These effects can be analysed from Eq. 4.28 and Eq. 4.29. We can see that when symmetry of the system is broken either by material type (ω_p for Drude metal) or size (γ), $\delta H \neq 0$. This causes the additional coupling between bonding/antibonding mode of the symmetric pair of its constituents as schematically shown, for instance, in Fig. 5.1. In the figure, the LSPR coupling of an asymmetric Au-Ag pair can be

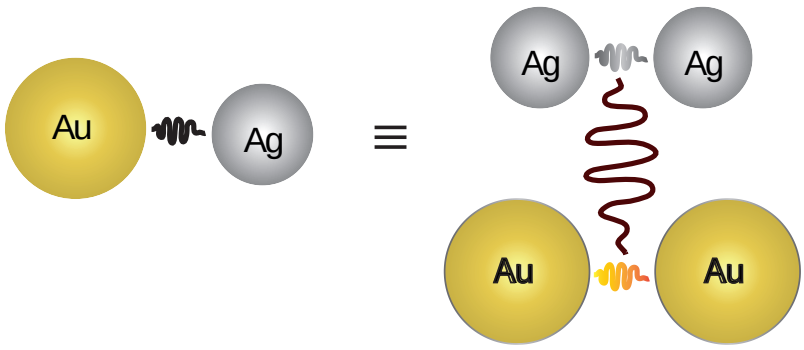

Figure 5.1: The schematically representation of the LSPR coupling in the asymmetric Au-Ag pair as coupling between symmetric Ag-Ag and Au-Au pairs image states.

interpreted as a result of the coupling between the individual symmetric Ag-Ag and Au-Au pairs. This two image states are implied by Eq. 4.29a. This coupling results in the change of mode characters as will be seen in the calculation results.

Before looking at the results, let us now introduce the notations which will be used in future discussion. We use the Greek alphabets σ (σ^*) and π (π^*) for bonding (antibonding) $m = 0$ and $m = 1$, respectively. Furthermore, we define the *mode switching* point as the point where the slope of the energy curve changes sign, and denoted by κ_i where $i = \sigma, \pi$ for $m = 0$, and $m = 1$, respectively. We also define a *mode crossing* point as the point that the σ and π modes cross each other, and denoted by χ. The results obtained in this chapter are calculated from Eq. 4.28 using the QEP method.

5.1 Internal property effects

Firstly, we study the effect of symmetry breaking due to the internal property (material type). Fig. 5.2 shows two lowest LSPR energy curves of the same size Ag-Au pair compared with the bonding (black) and antibonding (red) of the symmetric Ag-Ag (dashed) and Au-Au (dotted) pairs for $m = 0$, Fig. 5.2(a), and $m = 1$, Fig. 5.2(b), modes. Fig. 5.3 shows the same quantities as Fig. 5.2 but, instead, for the Ag-Cu pair. Now let us discuss the results shown in these figures, the first lowest energy of those asymmetric pairs are shifted to higher (lower) energy compared with the lowest energy of the bonding mode of the lower (higher) energy symmetric pair. In other words, they are shifted and bounded by the lowest energy of the symmetric pairs bonding mode. In contrast, the second lowest energy curve has different characters in two separation distance regimes separated by κ_i. On the right of κ_i, the curve has bonding mode character and becomes bounded by the second lowest energy of the symmetric pair bonding mode at the separation distance slightly far from κ_i as one can see in the figure. The values of mode switching points are $\kappa_\sigma^{\text{Ag-Au}} = 1.267$, $\kappa_\pi^{\text{Ag-Au}} = 1.204$, $\kappa_\sigma^{\text{Ag-Cu}} = 1.445$, and $\kappa_\pi^{\text{Ag-Cu}} = 1.478$ as shown in the inset panels of the figures. Fig. 5.4 is the comparison of two lowest energy of $m = 0$ and $m = 1$ modes for the Ag-Au pair (Fig. 5.4(a)) and for Ag-Cu pair (Fig. 5.4(b)). The mode crossing points for these pairs are $\chi^{\text{Ag-Au}} = 1.127$ and $\chi^{\text{Ag-Cu}} = 1.149$. From the results, one can observe that $\kappa_i^{\text{Ag-Cu}} > \kappa_i^{\text{Ag-Au}}$ which mean that the Ag-Cu second lowest energy curve is modified more slowly than that of Ag-Au due to its larger antibonding gap.

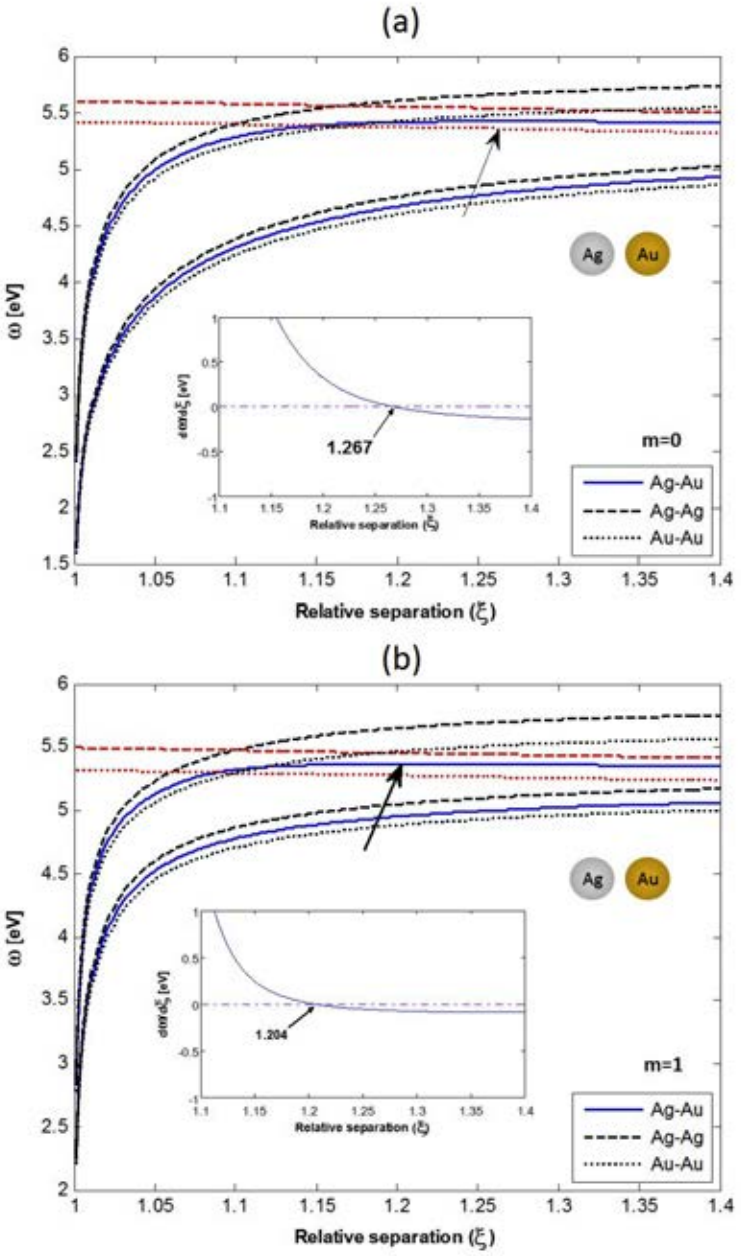

Figure 5.2: Two lowest LSPR energy of a pair of same Ag-Au for (a) $m = 0$, and (b) $m = 1$ modes. The black (red) dashed lines are the bonding (antibonding) LSPR energy of the symmetric Ag-Ag pair. Similarly, the dotted lines are for symmetric Au-Au pair.

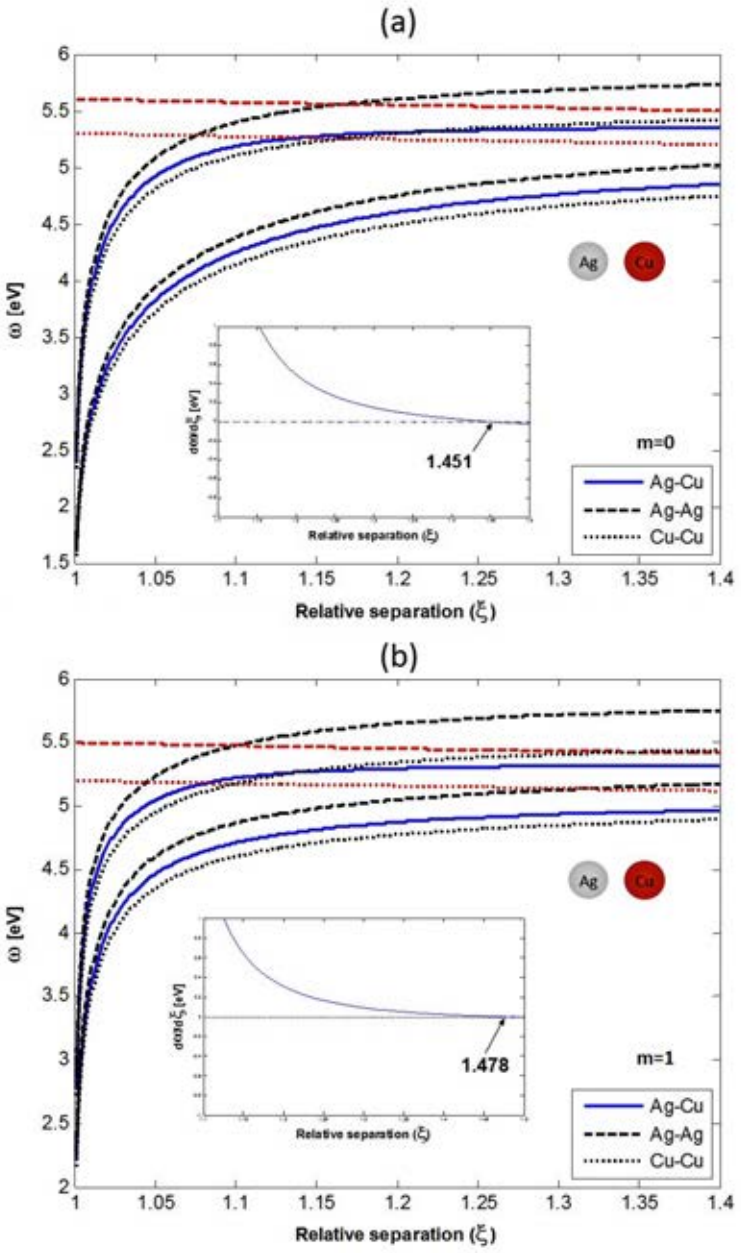

Figure 5.3: Two lowest LSPR energy of a pair of same Ag-Cu for (a) $m = 0$, and (b) $m = 1$ modes. The black (red) dashed lines are the bonding (antibonding) LSPR energy of the symmetric Ag-Ag pair. Similarly, the dotted lines are for symmetric Cu-Cu pair.

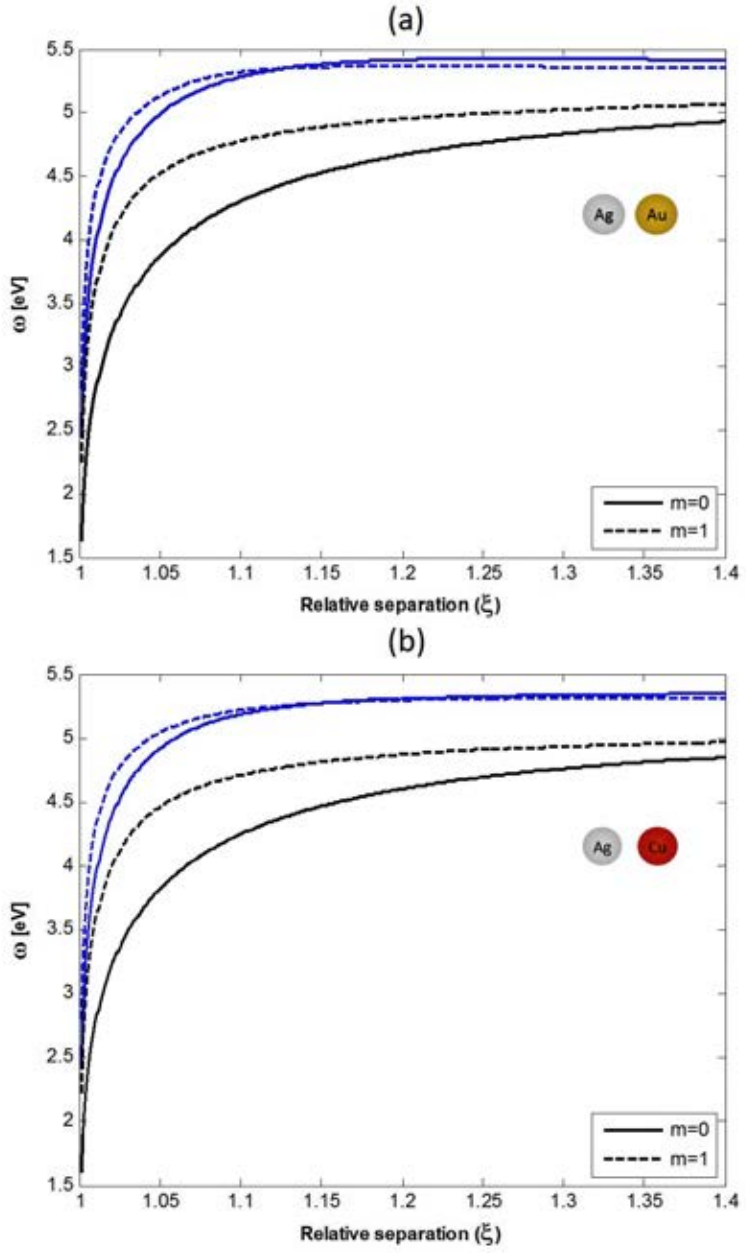

Figure 5.4: The comparison of two lowest LSPR energy of $m = 0$ (solid) and $m = 1$ (dashed) modes for (a) the Ag-Au pair, and (b) the Ag-Cu pair. The values of mode crossing points are $\chi^{\text{Ag-Au}} = 1.127$, and $\chi^{\text{Ag-Cu}} = 1.149$.

5.2 Geometrical property effects

Next, we investigate the effect of symmetry breaking due to the particle geometry (size). The plots of normalized lowest energy as a function of scaled separation distance for a number of size ratio are shown in Fig. 5.5 (a) for $m = 0$ mode and (b) for $m = 1$ mode. By increasing the size ratio (α), the LSPR energy increases be compared with the lowest energy of the symmetric pair bonding mode (dashed line). Moreover, it never changes the mode character and is bounded by the lowest energy of the single sphere LSPR ($l = 1$) marked by the red dot in the figures. The plots of the second lowest energy as a function of scaled separation distance are shown in Fig. 5.5 (a) for $m = 0$ mode and (b) for $m = 1$ mode. At large separation distance, the energy is redshift compared with the lowest energy of the symmetric pair antibonding mode (dashed line), with increasing α, and bounded by the lowest energy ($l = 1$) of the single sphere LSPR. More precisely, the curvature of the energy curve decreases with increasing α. This implies that the change of force with respect to the separation distance decreases with increasing α. The values of mode switching points are shown in the inset panels of the figure. The mode switching point shifts to the right with increasing α. Finally, we investigate the case that both effect of internal material property (ω_p) and geometrical property (size) play the role in LSPR coupling. Fig. 5.7 shows the plots of lowest LSPR energy of Au-Ag pairs with $\alpha = 1$, 3, and 5 as a function of scaled separation distance (a) for $m = 0$ mode and (b) for $m = 1$ mode. As it would be expected from the size effect, the lowest LSPR energy of the pair acquires the additional blue shift as α increases. Fig. 5.8 shows the energy curves of the second lowest energy (a) for $m = 0$ mode and (b) for $m = 1$ mode. The role of the symmetry breaking due to particle size can be seen from the decrease of the energy curve curvature as α increases. While the symmetry breaking due to material type tends to bound the energy curve within the antibonding gap at large separation distance. These effects surprisingly induce the shift of mode switching points to the left compared with that of the pair with $\alpha = 1$. This left shift is in contrast to the case that only the sizes of particles are different.

5.3 Excited mode order

At this stage, we have discussed two fundamental effects of symmetry breaking in LSPR coupling. We have defined the three fundamental points which are κ_σ, κ_π

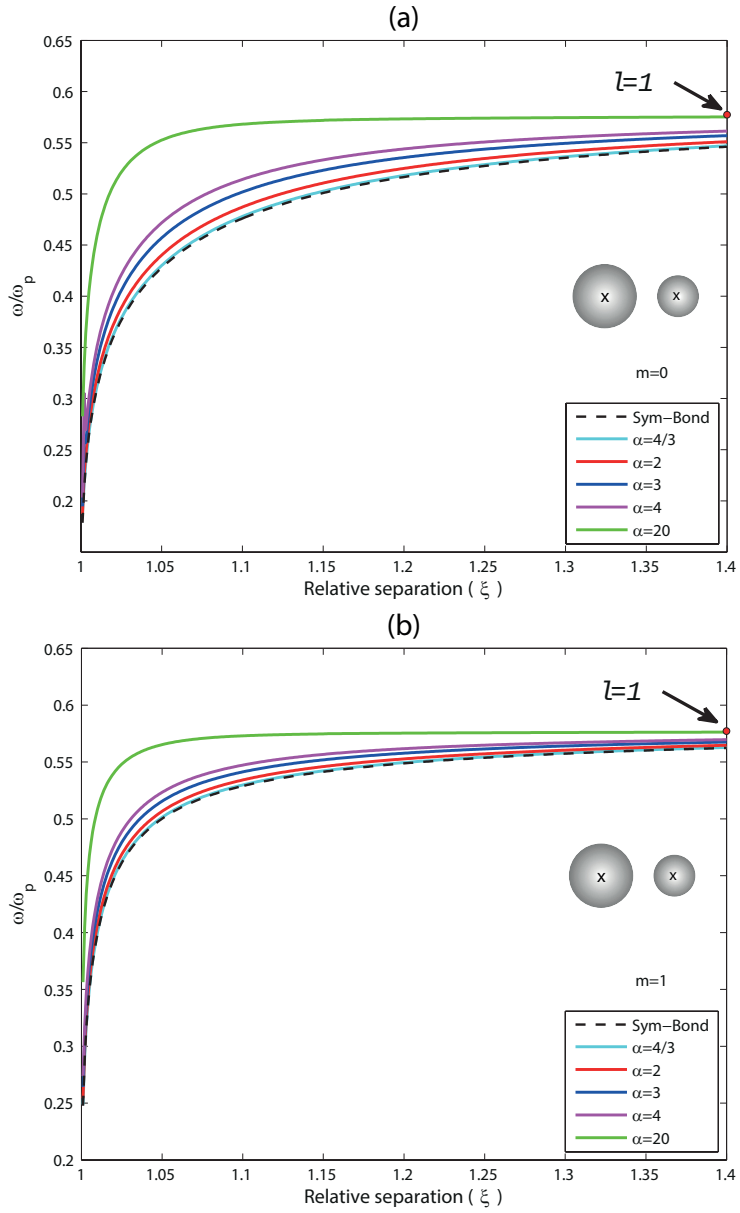

Figure 5.5: The lowest LSPR energy of a pair of same material with different sizes for (a) $m = 0$, and (b) $m = 1$ modes. The red dots indicate the lowest LSPR energy ($l = 1$) of the isolated single sphere.

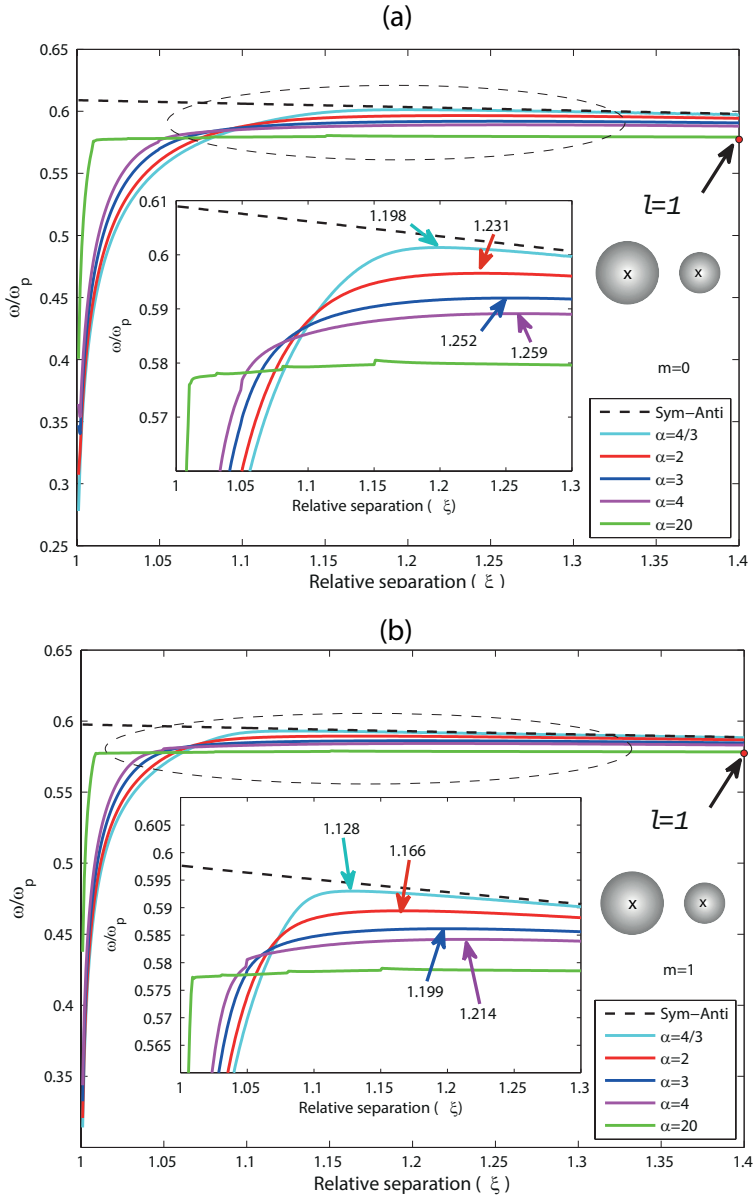

Figure 5.6: The second lowest LSPR energy of a pair of same material with different sizes for (a) $m = 0$, and (b) $m = 1$ modes. The red dots indicate the lowest LSPR energy ($l = 1$) of the isolated single sphere. The inset figures show plots in the area enclosed by the dashed oval. The arrows in the inset figures indicate the positions of κ_σ (a), κ_π) (b).

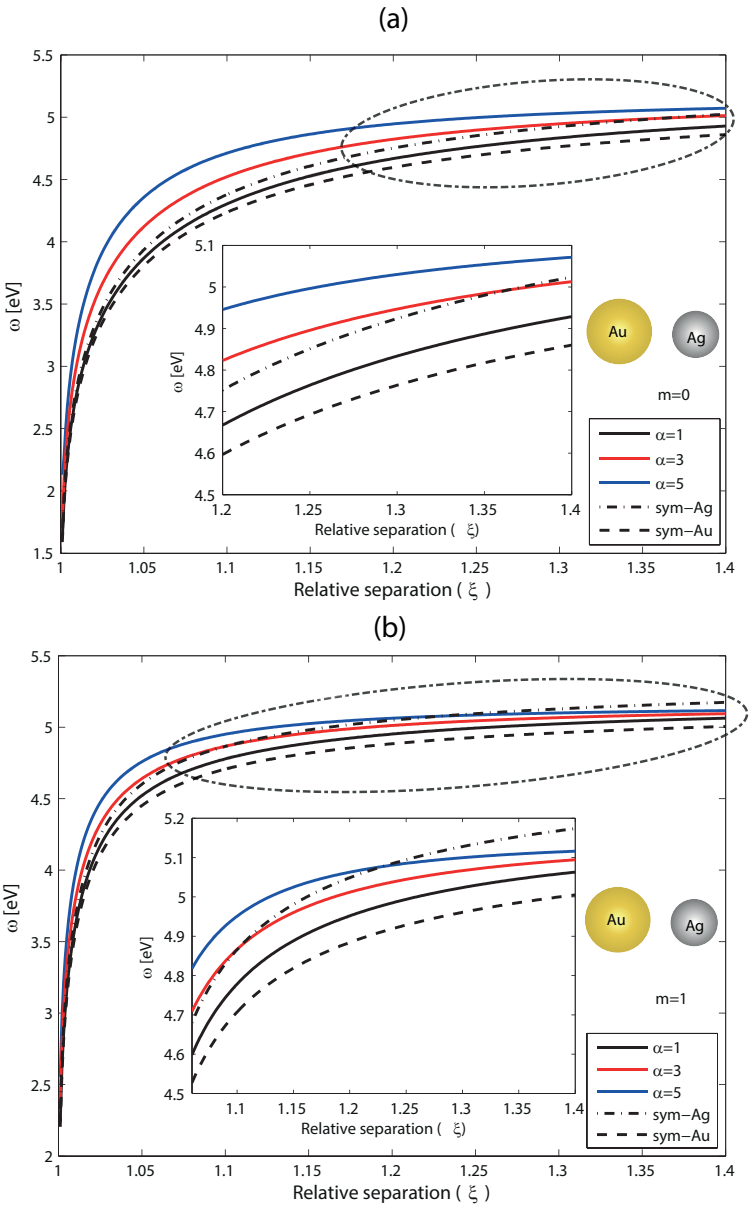

Figure 5.7: The lowest LSPR energy of a Ag-Au pair with different sizes for (a) $m = 0$, and (b) $m = 1$ modes. The red dots indicate the lowest LSPR energy ($l = 1$) of the isolated single sphere. The inset figures show plots in the area enclosed by the dashed oval.

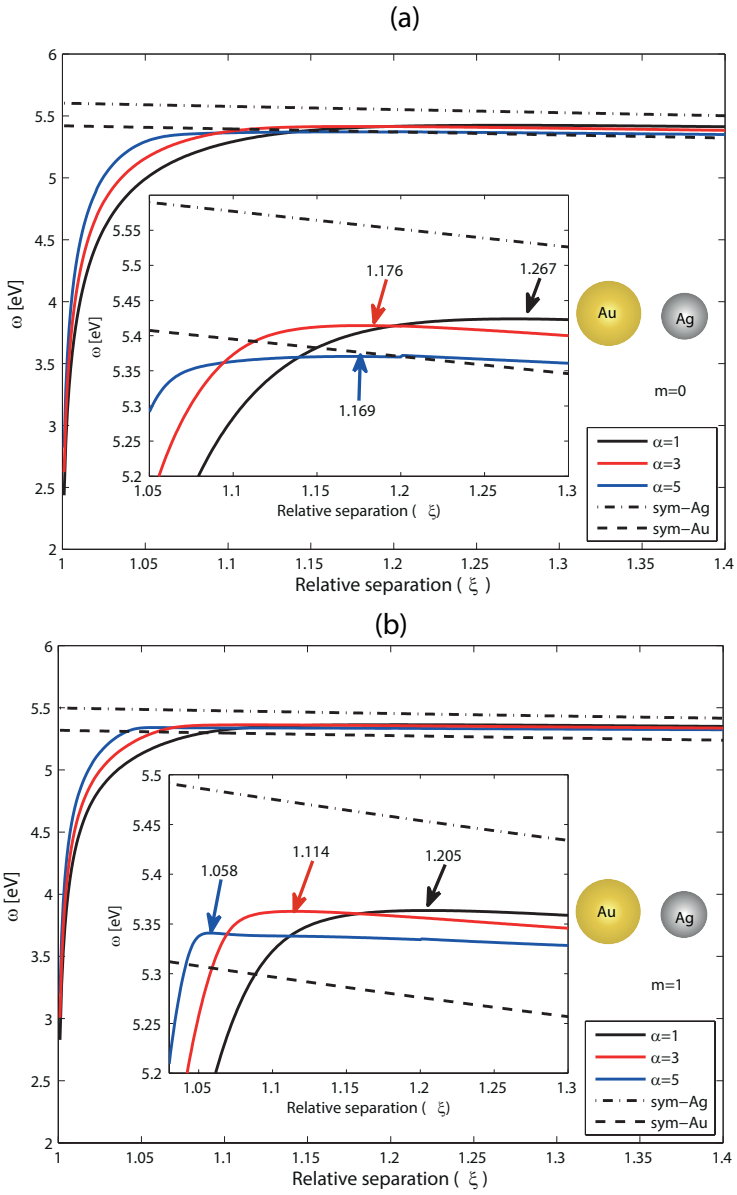

Figure 5.8: The second lowest LSPR energy of a Ag-Au pair with different sizes for (a) $m = 0$, and (b) $m = 1$ modes. The dashed (dotted) line is the lowest antibonding LSPR energy of a symmetric Ag-Ag (Au-Au) pair. The inset figures show plots in the area enclosed by the dashed oval. The arrows in the inset figures indicate the positions of κ_σ (a), κ_π) (b).

and χ. These points can be used to establish four physically distinct separation distance domain depending on the permutation of them. In order to describe which mode will be excited in the optical measurement (absorption or scattering spectra) if the polarization axis is not exactly known. However the excited mode could be the combination of two fundamental polarizations $m = 0$ and $m = 1$ modes. It is the reason for establishing a method for excited mode order for two cases: (a) a pair of the same material spheres with $\alpha = 2$ as shown in Fig. 5.9 and (b) a Au-Ag pair with $\alpha = 4/3$ as shown in Fig. 5.10. In case (a), the four regimes are separated by the ordered triplet (χ, κ_π, κ_σ). The excited mode order corresponding to their energy in the ascending order in each region is given by

$$\text{(i)}\ \ \sigma_1 \rightarrow \pi_1 \rightarrow \sigma_2 \rightarrow \pi_2 \ \text{ for } \ \xi_1 \in (1, \chi), \tag{5.1}$$

$$\text{(ii)}\ \ \sigma_1 \rightarrow \pi_1 \rightarrow \pi_2 \rightarrow \sigma_2 \ \text{ for } \ \xi_2 \in (\chi, \kappa_\pi), \tag{5.2}$$

$$\text{(iii)}\ \ \sigma_1 \rightarrow \pi_1 \rightarrow \pi_1^* \rightarrow \sigma_2 \ \text{ for } \ \xi_3 \in (\kappa_\pi, \kappa_\sigma), \tag{5.3}$$

$$\text{(iv)}\ \ \sigma_1 \rightarrow \pi_1 \rightarrow \pi_1^* \rightarrow \sigma_1^* \ \text{ for } \ \xi_4 \in (\kappa_\sigma, 1.4), \tag{5.4}$$

where $\chi = 1.101$, $\kappa_\pi = 1.166$ and $\kappa_\sigma = 1.231$. In case (b), the triplet is (κ_π, χ, κ_σ). The excited mode order in each region is given by

$$\text{(i)}\ \ \sigma_1 \rightarrow \pi_1 \rightarrow \sigma_2 \rightarrow \pi_2 \ \text{ for } \ \xi_1 \in (1, \kappa_\pi), \tag{5.5}$$

$$\text{(ii)}\ \ \sigma_1 \rightarrow \pi_1 \rightarrow \sigma_2 \rightarrow \pi_1^* \ \text{ for } \ \xi_2 \in (\kappa_\pi, \chi), \tag{5.6}$$

$$\text{(iii)}\ \ \sigma_1 \rightarrow \pi_1 \rightarrow \pi_1^* \rightarrow \sigma_2 \ \text{ for } \ \xi_3 \in (\chi, \kappa_\sigma), \tag{5.7}$$

$$\text{(iv)}\ \ \sigma_1 \rightarrow \pi_1 \rightarrow \pi_1^* \rightarrow \sigma_1^* \ \text{ for } \ \xi_4 \in (\kappa_\sigma, 1.4), \tag{5.8}$$

where $\chi = 1.129$, $\kappa_\pi = 1.114$ and $\kappa_\sigma = 1.176$.

We now compare these analyses with the experimental results of Sheikholeslami *et al* [34]. In their work, they measured the scattering spectra of the individual pair of particles in three cases: (i) symmetric Ag-Ag, (ii) asymmetric Ag-Ag with radii $R_1 = 40$ nm and $R_2 = 20$ nm and (iii) asymmetric Au-Ag with Au radius = 40 nm and Ag radius = 30 nm. The TEM images of the particle pairs are shown in Fig. 5.11 and the corresponding scattering spectra are shown in Fig. 5.12 and Fig. 5.13. By comparing our analysis in case (a) with the experimental results case (ii), we found that the experimental result is in qualitative agreement with our analysis in region ξ_4. In case (b), interestingly, our analysis in region ξ_2 is in good agreement with the experimental result (case (iii)). Furthermore, we argue that the mode σ^* in Fig. 5.13(b) should be σ_2, the quadrupole bonding mode, instead of σ^*, dipole antibonding mode. This is reasonable for the strong scattering mode due to the cancellation of dipole moment as mentioned by the authors of Ref. [34].

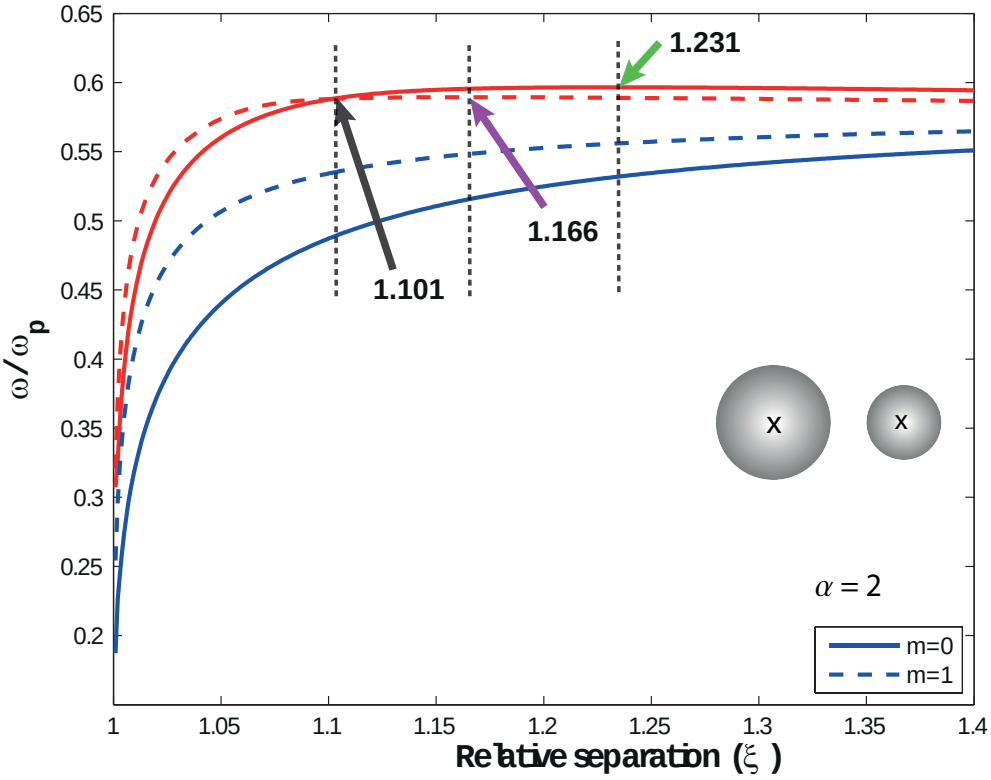

Figure 5.9: The comparison of two lowest LSPR energy of $m = 0$ (solid) and $m = 1$ (dashed) modes for the Ag-Ag pair with $\alpha = 2$. The arrows indicate the positions of the triplet (χ, κ_π, κ_σ), i.e. $\chi = 1.101$, $\kappa_\pi = 1.166$, and $\kappa_\sigma = 1.231$.

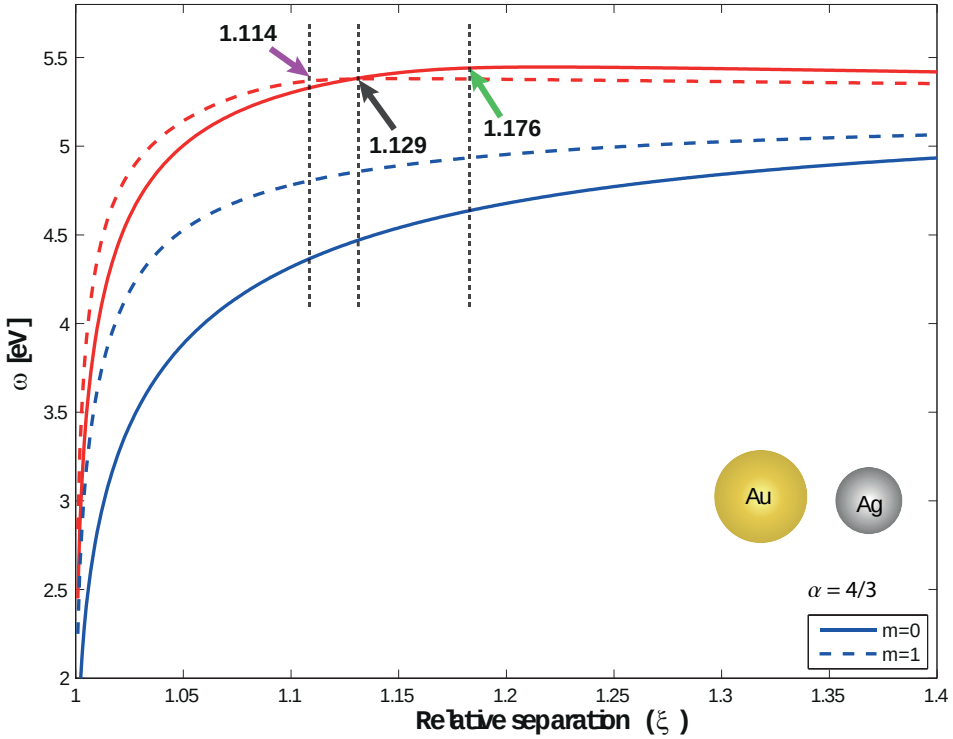

Figure 5.10: The comparison of two lowest LSPR energy of $m = 0$ (solid) and $m = 1$ (dashed) modes for the Au-Ag pair with $\alpha = 4/3$. The arrows indicate the positions of the triplet (κ_π, χ, κ_σ), i.e. $\kappa_\pi = 1.114$, $\chi = 1.129$, and $\kappa_\sigma = 1.176$.

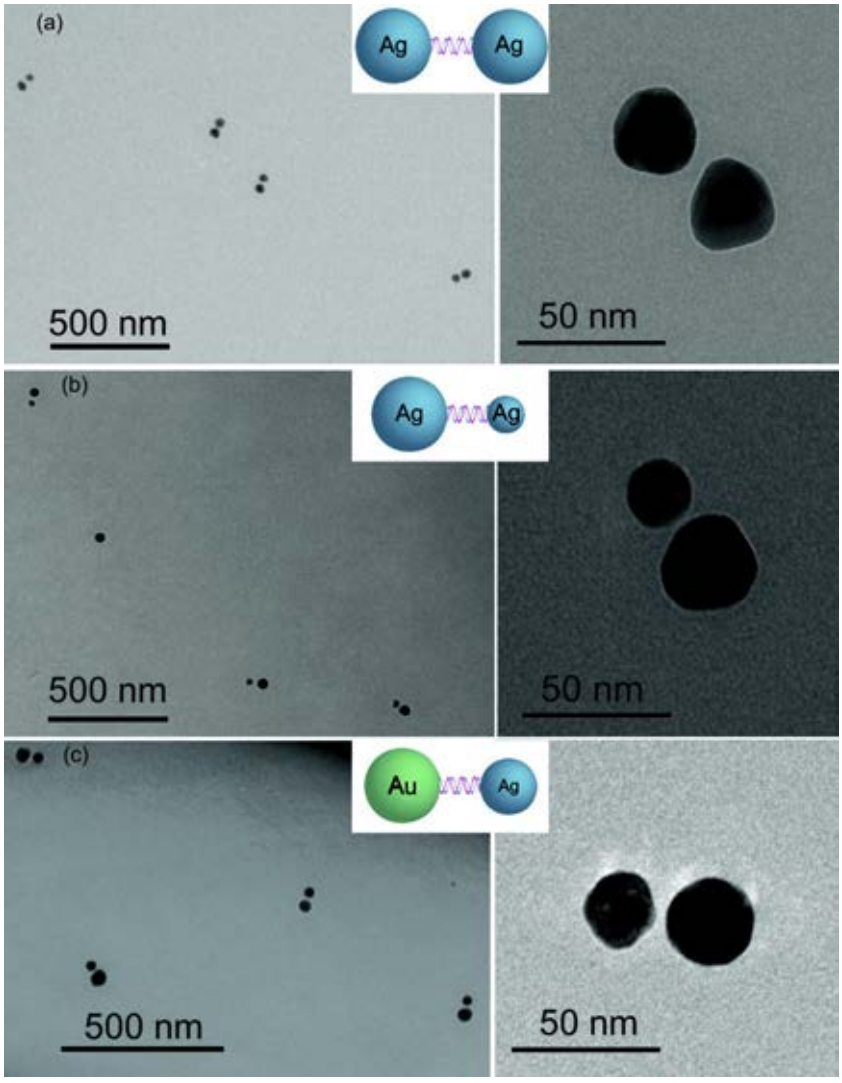

Figure 5.11: The TEM images of (a) symmetric Ag-Ag with readii $R_1 = R_2 = 40$ nm, (b) asymmetric Ag-Ag with radii $R_1 = 40$ nm, $R_2 = 20$ nm and (c) asymmetric Au-Ag with radii $R_{Au} = 40$ nm, $R_{Ag} = 30$ nm [34].

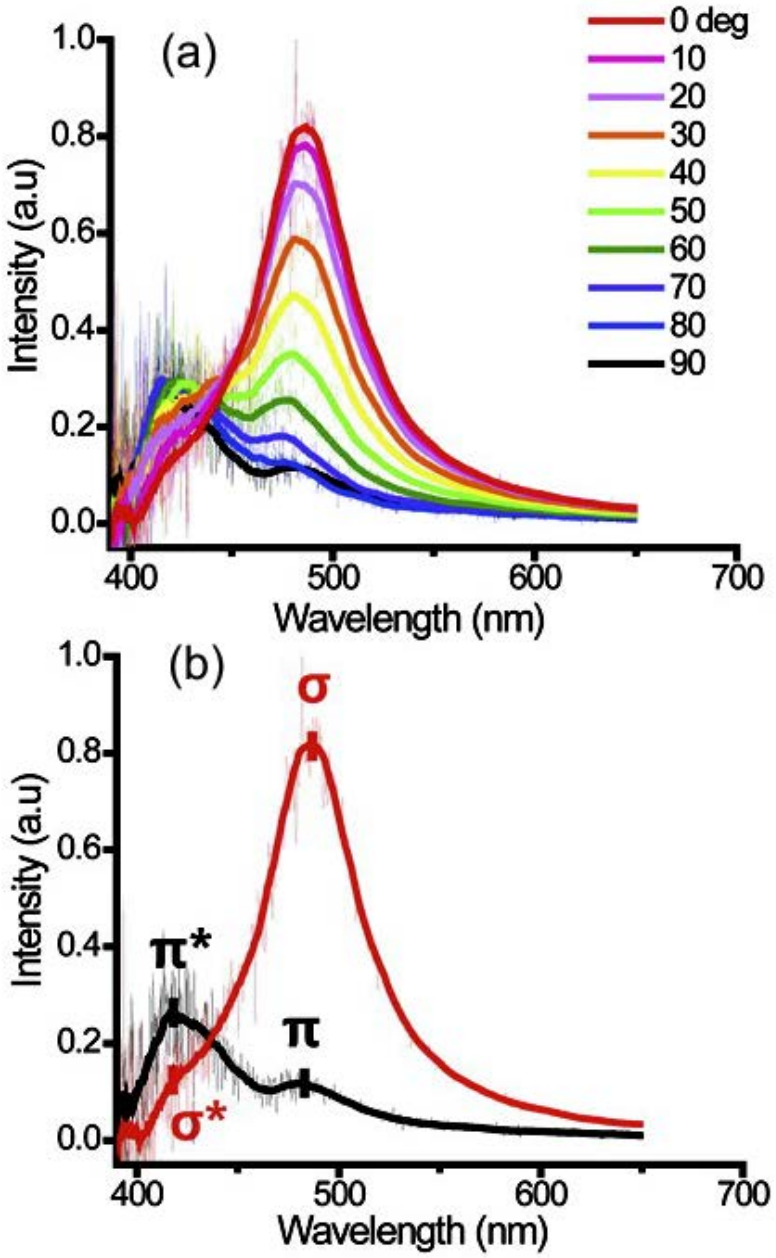

Figure 5.12: The scattering spectra of the asymmetric Ag-Ag pair with $R_1 = 40$ nm, $R_2 = 20$ nm. (a) The spectra at a number of polarize angles, (b) the spectra at the polarize angle $\theta = 0°$ (red) and $\theta = 90°$ (black). The peak positions are $\sigma = 486$ nm, $\pi = 481$ nm, $\pi^* = 422$ nm, and $\sigma^* = 420$ nm [34].

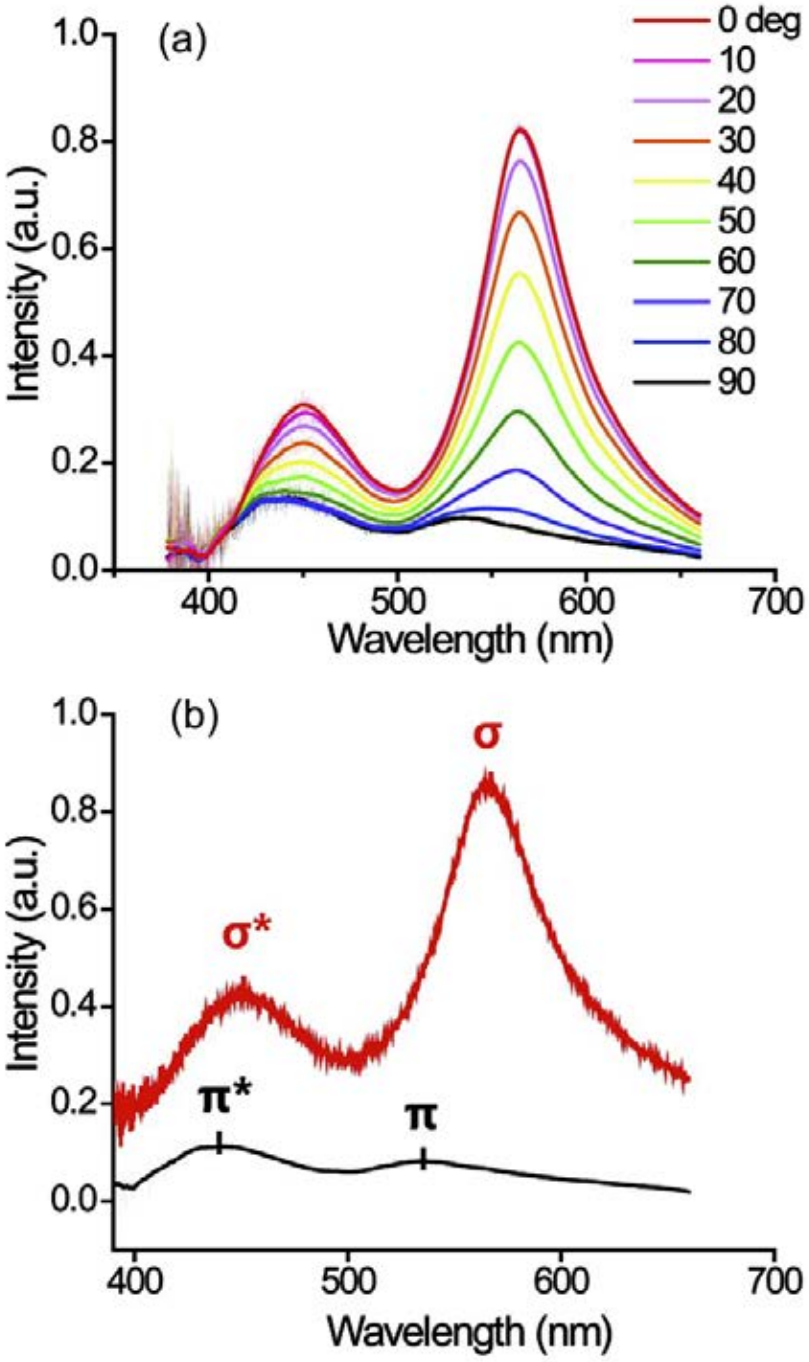

Figure 5.13: The scattering spectra of the asymmetric Au-Ag pair with $R_{Au} = 40$ nm, $R_{Ag} = 30$ nm. (a) The spectra at a number of polarize angles, (b) the spectra at the polarize angle $\theta = 0°$ (red) and $\theta = 90°$ (black). The peak positions are $\sigma = 565$ nm, $\pi = 536$ nm, $\sigma^* = 437$ nm, and $\pi^* = 450$ nm [34].

Chapter VI

Conclusion

In this dissertation, we investigate the effects of symmetry breaking to the LSPR coupling. For simplicity, without losing any physical significant, we restrict the derivation within the quasi static regime and considering the spherical particle pair. Within this limit, we solve for the solution of Laplace equation and then apply the boundary conditions at the sphere surfaces. These procedures allow us to derive the recursion relations, Eq. 4.11 and Eq. 4.12, for the expansion coefficient of the Laplace equation solutions. These recursion relations form a system of infinite coupled linear equations. Hence, we introduce the vector and matrix notations and solve the problem using the matrix formulation. This leads to the nonlinear eigenvalue problem (NLEVP). The general expression for surface mode resonant is derived as Eq. 4.28. The expression allows us to interpret the LSPR energy of the asymmetric pair as a consequence of the coupling between two image states of the symmetric pair of the constituent particles as schematically shown in Fig.5.1

In order to investigate the effects of symmetry breaking, we apply the resonant condition to calculate, for instance, the LSPR energy of the negligible damping Drude metallic sphere pairs. First, we study the effect of symmetry breaking due to the matrial type. We found that the lowest LSPR energy shifts and is bounded by the lowest energies of the bonding image states of its constituents. For the second lowest energy, the energy curve is bounded by the second lowest energy of the bounding image states at small separation distance and is bounded by the lowest energy of the antibonding symmetric pair at large separation distance. The antibonding gap is the gap between the lowest energy of the antibonding image states. The antibonding gap influences to the position of the mode switching point (κ_i). The larger gap leads to the larger κ_i so that $\kappa_i^{\text{Ag-Cu}} > \kappa_i^{\text{Ag-Au}}$ for $i = \sigma, \pi$. Second, the effects of symmetry breaking due to the particle size are investigated. We found that for the lowest LSPR energy, the energy is blue shifted as the particle size ratio (α) increases and has the lowest LSPR energy of the single particle ($l = 1$) as the upper bound. For the second lowest energy, the

energy curve's curvature decreases as α increases which leads to the shift of κ_i to the right as α increases. Finally, the effects of symmetry breaking due to both of internal property (material type) and geometrical property (size) are investigated by calculating the LSPR energy of the asymmetric Au-Ag pair. We found that for the lowest LSPR energy, the energy curve is not bounded by the lowest energy curve of the bonding image states of Au-Au and Ag-Ag pairs since it acquires the additional blueshift from the effect of size difference. For the second lowest energy, there are two effects cooperate in the change of LSPR energy. The first one is decreases of energy curve's curvature due to the asymmetry in size and the second one is the presence of antibonding gap bounding due to the asymmetry of material type. These lead to the shift of κ_i to the left as α increases. Furthermore, we establish the methods for excited mode order analysis. This analysis provide the way for identifying the mode character, for example bonding dipole mode, antibonding dipole mode, bonding quadrupole mode, etc., at the peak position of the scattering (or absorption) spectra. Our analysis is in qualitatively agreement with the recent experimental results [34].

Briefly, the derived surface mode resonant condition is general for a pair of spherical particles of which the dielectric functions are known. Using a more realistic dielectric function could improve the calculation accuracy but can lead to complex form of NLEVP. Advances in NLEVP could improve the applicability of the theory. We shall expect the extension for more complicated structure such as the asymmetric core-shell as well.

REFERENCES

[1] Wiesnar Group. Plasmonics [Internet]. 2014 [cited 2014 Jul 1]. Available from; *http : //wiesner.mse.cornell.edu/res_optics.htm*

[2] Sharmaa P, Browna S, Walterc G, Santrad S and Moudgil B. Nanoparticles for bioimaging. **Advances in Colloid and Interface Science.** 123-126 (2006) : 471-485.

[3] Huang X, El-Sayed I H, Qian W and El-Sayed M A. Cancer Cell Imaging and Photothermal Therapy in the Near-Infrared Region by Using Gold Nanorods. **J. Am. Chem. Soc.** 128 (2006) : 2115-2120.

[4] Liao H, Nehl C L and Hafner J H. Biomedical applications of plasmon resonant metal nanoparticles. **Nanomedicine-UK** 1 (2006) : 201-208.

[5] Svedberg F, Li Z, Xu H and Kll M. Creating Hot Nanoparticle Pairs for Surface-Enhanced Raman Spectroscopy through Optical Manipulation. **Nano Lett.** 6 (2006) : 2639-2641.

[6] Westphalen M, Kreibig U, Rostalski J, Lukth H and Meissner D. Metal cluster enhanced organic solar cells. **Sol. Energy Mater. Sol. Cells** 61 (2000) : 97-105.

[7] Kawawaki T, Takahashi Y and Tatsuma T. Enhancement of Dye-Sensitized Photocurrents by Gold Nanoparticles: Effects of Plasmon Coupling. **J. Phys. Chem. C.** 117 (2013) : 5901-5907.

[8] Giannini V, Fernandez-Dominguez A L, Heck S C and Maier S A. **Chem. Rev.** 111 (2011) : 3888-3912.

[9] Hutter E and Fendler J H. Exploitation of Localized Surface Plasmon Resonance. **Ad. Mat.** 16 (2004) : 1685-1706.

[10] Mayer K M and Hafner J H. Localized Surface Plasmon Resonance Sensors. **Chem. Rev.** 111 (2011) : 3828-3857.

[11] Lopatynskyi A M, Lopatynska Q G, Guo L J and Chegel V I. **IEEE Sens. J.** 11 (2011) : 361-369.

[12] Haes A J and Duyne R P V. A Nanoscale Optical Biosensor Sensitivity and Selectivity of an Approach Based on the Localized Surface Plasmon Resonance Spectroscopy of Triangular Silver Nanoparticles. **J. Am. Chem. Soc**. 124 (2002) : 10596-10604.

[13] Anker J N, Hall W P, Lyandres O, Shah N C, Zhao J and Duyne R P V. Biosensing with plasmonic nanosensors. **Nat. Mater**. 7 (2008) : 442-453.

[14] Reinhard B M, Sheikholeslami S, Mastroianni A, Alivisatos A P and Liphardt J. Creating Hot Nanoparticle Pairs for Surface-Enhanced Raman Spectroscopy through Optical Manipulation. **PNAS.** 104 (2007) : 2667–2672.

[15] Alvarez M M, Khoury J T, Schaaff T G, Shafigullin M N, Vezmar I and Whetten R L. Optical Absorption Spectra of Nanocrystal Gold Molecules. J. Phys. Chem. B. 101 (1997) : 3706-3712.

[16] Lyon L A, Pea D J and Natan M J. Surface Plasmon Resonance of Au Colloid-Modified Au Films: Particle Size Dependence. **J. Phys. Chem. B.** 103 (1999) :5826-5831.

[17] Link S and El-Sayed M A. Spectral Properties and Relaxation Dynamics of Surface Plasmon Electronic Oscillations in Gold and Silver Nanodots and Nanorods. **J. Phys. Chem. B.** 103 (1999) : 8410-8426.

[18] Sheng X, Hu J, Michel J and Kimerling L C. Light trapping limits in plasmonic solar cells: an analytical investigation. **OPTICS EXPRESS** 20 (2012) : A496-A501.

[19] Jia B, Chen X, Saha J K, Qiao Q, Wang Y, Shi Z and Gu M. Concept to devices: from plasmonic light trapping to upscaled plasmonic solar modules. **Photon. Res.** 1 (2013) : 22-27.

[20] Hsiao Y S, Charan S, Wu F Y, Chien F C, Chu C W, Chen P and Chen F C. Improving the Light Trapping Efficiency of Plasmonic Polymer Solar Cells through Photon Management. **J. Phys. Chem. C** 116 (2012) : 20731-20737.

[21] Schuller J A, Barnard E S, Cai W, Jun Y C, White JS and Brongersma ML Plasmonics for extreme light concentration and manipulation. **Nature materials** 9 (2010): 193-204.

[22] Batson P E. Surface Plasmon Coupling in Clusters of Small Spheres. **Phys. Rev. Lett.** 49 (1982) : 936.

[23] Ruppin R.Surface modes of two spheres. **Phys. Rev. B**. 26 (1982) : 3440.

[24] Chu P and Mills D L. Electromagnetic response of nanosphere pairs: Collective plasmon resonances, enhanced fields, and laser-induced forces. **Phys. Rev. B** 77 (2008) : 045416.

[25] Chu P and Mills D L. Laser-Induced Forces in Metallic Nanosystems: The Role of Plasmon Resonances. **Phys. Rev. Lett.** 99 (2007) : 127401.

[26] Xu H and Käll M. Surface-Plasmon-Enhanced Optical Forces in Silver Nanoaggregates. **Phys. Rev. Lett.** 89 (2002) 246802.

[27] Ng J, Tang R and Chan C. Electrodynamics study of plasmonic bonding and antibonding forces in a bisphere. Phys. Rev. B. 77 (2008) :195407.

[28] Klimov V V and Guzatov D V. Strongly localized plasmon oscillations in a cluster of two metallic nanospheres and their influence on spontaneous emission of an atom. **Phys. Rev. B.** 75 (2007) : 024303.

[29] Encina E R and Coronado E A. Plasmon Coupling in Silver Nanosphere Pairs. **J. Phys. Chem. C.** 114 (2010) : 3918-3923.

[30] Encina E R and Coronado E A. Near Field Enhancement in Ag Au Nanospheres Heterodimer. **J. Phys. Chem. C.** 89 (2011) : 15908-15914.

[31] Shegai T, Chen S, Miljković V D, Zengin G, Johansson P and Käll M. A bimetallic nanoantenna for directional colour routing. **Nature Communications.** 2 (2011) : 4190.

[32] Chu Y, Schonbrun E, Yang T and Crozier KB. Experimental observation of narrow surface plasmon resonances in gold nanoparticle arrays. **Appl. Phys. Lett.** 93 (2008) : 181108.

[33] Cunningham A, Mühlig S, Rockstuhl C and Bürgi T. Exciting Bright and Dark Eigenmodes in Strongly Coupled Asymmetric Metallic Nanoparticle Arrays. textbfJ. Phys. Chem. C. 116 (2012) : 17746-17752.

[34] Sheikholeslami S, Jun Y, Jain P K and Alivisatos A P. Coupling of Optical Resonances in a Compositionally Asymmetric Plasmonic Nanoparticle Dimer. **Nano Lett.** 10 (2010) : 2655-2660.

[35] Bachelier G, Russier-Antoine I, Benichou E, Jonin C, Fatti N D, Valle F, Brevet P F. Fano Profiles Induced by Near-Field Coupling in Heterogeneous Dimers of Gold and Silver Nanoparticles. **Phys. Rev. Lett.** 101 (2008) : 197401.

[36] Peña-Rodríguez O, Pal U, Campoy-Quiles M, Rodrguez-Fernández L, Garriga M and Alonso M I. Enhanced Fano Resonance in Asymmetrical Au:Ag Heterodimers. **J. Phys. Chem. C** 115 (2011) : 6410- 6414.

[37] Prodan E, Radloff C, Halas NJ and Nordlander P. A Hybridization Model for the Plasmon Response of Complex Nanostructures. **Science** 302 (2003) : 419-422.

[38] Nordlander P, Oubre C, Prodan E, Li K and Stockman MI. Plasmon Hybridization in Nanoparticle Dimers. **Nano Lett.** 4 (2004) : 899-903

[39] Nordlander P and Prodan E. Plasmon Hybridization in Nanoparticles near Metallic Surface. **Nano Lett.** 4 (2004) : 2209-2213.

[40] Brandl D W, Oubre C and Nordlander P. Plasmon hybridization in nanoshell dimers. **J.Chem. Phys.** 123 (2005) : 024701.

[41] Brandl D W, Mirin N A and Nordlander P. Plasmon Modes of Nanosphere Trimers and Quadrumers. **J. Phys. Chem. B.** 110 (2006) : 12302-12310.

[42] Quinten M. **Optical Properties of Nanoparticle Systems**. Wiley-VCH, 2011.

[43] Fox M. **Optical Properties of Solids**. Oxford University Press, 2001.

[44] Drude P. Zur Elektronentheorie der metalle. **Ann. Phys.** 306 (1900) : 566-613.

[45] Drude P. Zur Elektronentheorie der Metalle; II. Teil. Galvanomagnetische und thermomagnetische Effecte. **Ann. Phys.** 308 (1900) : 369-402.

[46] Ashcroft NW and Mermin DN. **Solid State Physics**. Harcourt College Publishers, 1976.

[47] Giuliani G and Vignale Giovanni. **Quantum Theory of the Electron Liquid**. Cambridge University Press, 2005.

[48] Madelung O. **Introduction to Solid-State Theory**. Springer-Verlag Berlin Heidelberg, 1978.

[49] Marder M P. **Condensed Matter Physics**. John Wiley & Son Inc., 2000.

[50] Kittel C. **Introduction to Solid State Physics 6th edition**. John Wiley & Son Inc., 1986.

[51] West P R, Ishii S, Naik1 G V, Emani N K, Shalaev V M and Boltasseva A. Searching for better plasmonic materials. **Laser Photonics Rev.** 4 (2010) : 795-808.

[52] Pines D and Bohm D. A collective description of electron interaction : II Collective vs individual particle aspects of the interaction. **Phys. Rev.** 85 (1952) : 338.

[53] Ritchie R H and Wilems R E. Photon-Plasmon Interaction in a Nonuniform Electron Gas. **Phys. Rev.** 178 (1969) : 372.

[54] Stern E A and Ferrell R A. Surface Plasma Oscillations of a Degenerate Electron Gas. **Phys. Rev.** 120 (1980) : 130.

[55] Sarid D and Challener W. **Surface Plasmons: Theory, Mathematica Modeling, and Applications**. Cambridge University Press, New York, 2010.

[56] Bohren C F and Huffman D R. **Absorption and Scattering of Light by Small Particles**. John Wiley & Sons, New York, 1983.

[57] Benson O. Assembly of hybrid photonic architectures from nanophotonic constituents. **Nature** 480 (2011) 193.

[58] Pitarke J M, Silkin V M, Chulkov E V and Echenique P M. Theory of surface plasmons and surface-plasmon polaritons. **Rep. Prog. Phys.** 70 (2007) : 1-87.

[59] Maier S A. **Plasmonics Fundamental and applications**. Springer, 2007.

[60] Elson J M and Ritchie R H. Photon interactions at a Rough Metal Surface. **Phys. Rev. B.** 4 (1971) : 4129.

[61] McFarland AD and Van Duyne RP. Single nanoparticles as real-time optical sensors with zeptomole sensitivity. **Nano Lett.** 3 (2003) : 1057.

[62] Derkachova A and Kolwas K. Size dependence of multipolar plasmon resonance frequencies and damping rates in simple metal spherical nanoparticles. **Eur. Phys. J. Special Topics** 144 (2007): 93-99.

[63] Cottancin E, Celep G, Lermé J, Pellarin M, Huntzinger J R ,Vialle J L and Broyer M. Optical properties of noble metal cluster as a function of the size comparison between experiments and a semi-quantal theory. **Theor Chem Acc** 116 (2006) : 514-523.

[64] Noguez C. Surface Plasmons on Metal Nanoparticles: The Influence of Shape and Physical Environment. **J. Phys. Chem. C** 111 (2007) : 3806-3819.

[65] Lerme J, Baida H, Bonet C, Broyer M, Cottancin E, Crut A, Maioli P, Del Fatti N, Vallee F and Pellarin M. Size Dependence of the Surface Plasmon Resonance Damping in Metal Nanospheres. **J. Phys. Chem. Lett.** 1 (2010) : 2922-2928.

[66] Kelly K L, Coronado E, Zhao L L and Schatz G C. The Optical Properties of Metal Nanoparticles The Influence of Size, Shape, and Dielectric Environment. **J. Phys. Chem. B** 107 (2003) : 668-677.

[67] Mock J J, Barbic M, Smith D R, Schultz D A and Schultz S. Shape effects in plasmon resonance of individual colloidal silver nanoparticles. **J. Chem. Phys.** 116 (2002) : 6755.

[68] Kuwata H, Tamaru H, Esumi K and Miyano K. Resonant light scattering from metal nanoparticles: Practical analysis beyond Rayleigh approximation. **Appl. Phys. Lett.** 83 (2003) : 4625.

[69] Mie G. Beiträge zur optik trüber medien, speziell kolloidaler metallösugen. **Ann. d. Physik** 25 (1908) : 377.

[70] Lorenz L. Lysbevaegelsen i og uden for en af plane Lysbolger belyst Kugle. **Det Kongelige Danske Videnskabernes Selskabs Skrifter.** 6(1890) : 162.

[71] Landau L D and Lifshitz E M. **Electrodynamics of Continuous Media**. Pergemon Press, New York, 1960.

[72] Larsson J. Electromagnetics from a quasistatic perspective. **Am. J. Phys.** 75 (2007) : 230-239.

[73] Jackson J D. **Classical Electrodynamics 2nd edition**. John Wiley, New York, 1975.

[74] Link S and EI-Sayed M A. Shape and size dependent of radiative, non-radiative and photothermal properties of gold nanoparticles. **International Reviews in Physical Chemistry** 19 (2000) : 409-453.

[75] Rechberger W, Hohenau A, Leitner A, Aussenegg F R, Krenn J R and Lamprecht B. Optical properties of two interacting gold nanoparticles. **Optics Communications.** 220 (2003) : 137141.

[76] Esteban R, Borisov A G, Nordlander P and Aizpurua J. Bridging quantum and classical plasmonics with a quantum-corrected model. **Nature Communications.** 3 (2011) : 825-829.

[77] García AFJ. Nonlocal Effects in the Plasmons of Strongly Interacting Nanoparticles, Dimers, and Waveguides. **J. Phys. Chem. C.** 112 (2008) : 17983-17987.

[78] Moon P and Spencer D E. **J. Franklin Inst.** 253 (1952) : 585.

[79] Morse P M and Feshbach H. **Methods of Theoretical Physics Part II**. McGRAW-HILL, 1953.

[80] Abramowitz M and Stegun I A, (ed.). **Handbook of Mathematical Functions with Formulas, Graphs, and Mathematical Tables**, New York, Dover Publications, 1972.

[81] Lucas A A, Ronveaux A, Schmeits M, and Delanaye F. **Phys. Rev. B** 12 (1975) : 5372.

[82] Chaumet P C and Dufour J P. Electric potential and field between two different spheres. **Journal of electrostatics** 43 (1998) : 145-159.

[83] GÓNGORA-T A and LEY-Koo E. On the evaluation of the capacitance of bispherical capacitors. **Revist Mexicana de Phisica.** 42 (1996) : 663-674.

[84] Betcke T, Higham N J, Mehrmann V, Schröder C and Tisseur F. NLEVP: A collection of nonlinear eigenvalue problems. **ACM Trans. Math. Softw.** 39 (2013) : 7.

[85] Hammarling S, Munro C J and Tisseur F. An algorithm for the complete solution of quadratic eigenvalue problems. **ACM Trans. Math. Softw.** 39 (2013) : 18.

[86] Mehrmann V and Voss H. Nonlinear eigenvalue problems: A challenge for modern eigenvalue methods. **GAMM-Reports** 27 (2004) : 121-152.

[87] Betcke T, Higham N J, Mehrmann V, Schröder C, and Tisseur F. **NLEVP: A Collection of Nonlinear Eigenvalue Problems. Users' Guide.** MIMS EPrint 2011.117, Manchester Institute for Mathematical Sciences, The University of Manchester, UK, Dec 2011. avialable from : *http* : *//www.manchester.ac.uk/mims/eprints*

[88] Gaubert S and Sharify M. Tropical Scaling of Polynomial Matrices. **Lecture Notes in Control and Information Sciences** 389 (2009) : 291-303.

[89] Higham N J, Li R C and Tisseur F. Backward Error of Polynomial Eigenproblems Solved by Linearization. **SIAM Journal on Matrix Analysis and Applications** 29 (2008) : 1218-1241.

[90] Higham N J, Mackey D S, Tisseur F. and Garvey S D. Scaling, sensitivity and stability in the numerical solution of quadratic eigenvalue problems. **International journal for numerical methods in engineering**. 73 (2008) : 344-360.

[91] Higham N J, Mackey D S and Tisseur F. The Conditioning of Linearizations of Matrix Polynomials. **SIAM Journal on Matrix Analysis and Applications**. 28 (2006) : 1005-1028.

[92] Hung-Yuan F, Wen-Wei L and Paul Van D. Normwise Scaling of Second Order Polynomial Matrices. **SIAM Journal on Matrix Analysis and Applications**. 26 (2004) : 252-256.

[93] Tisseur F and Meerbergen K. The quadratic eigenvalue problem. **SIAM Review**. 43 (2001) : 235-286.

[94] Sleijpen G LG, Van der Vorst HA and Van Gijzen M. Quadratic eigenproblems are no problem. **SIAM News** 29 (1996) : 8-9.

APPENDICES

Appendix A

Bispherical coordinate system

Bispherical coordinates (γ, η, φ) are defined as (see Fig.A.1)

$$x = \frac{a \sin\eta \cos\varphi}{\cosh\gamma - \cos\eta}, \tag{A.1}$$

$$y = \frac{a \sin\eta \sin\varphi}{\cosh\gamma - \cos\eta}, \tag{A.2}$$

$$z = \frac{a \sinh\gamma}{\cosh\gamma - \cos\eta}, \tag{A.3}$$

where γ goes from $-\infty$ to ∞, η goes from 0 to π, and φ goes from 0 to 2π, h is

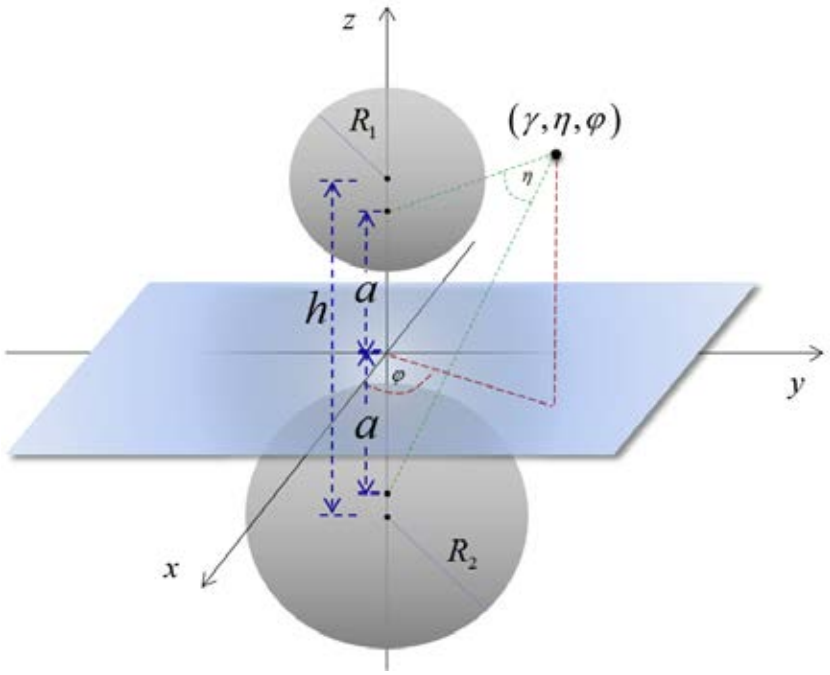

Figure A.1: The bispherical coordinate system.

center-to-center interparticle distance, and a is a coordinate parameter defined as

half distance between two poles of spheres as shown in Fig. A.1. x, y and z are cartesian coordinates (See Ref. [82, 83] for more informations). Consider

$$x^2+y^2+z^2=\left(\frac{a\sin\eta\cos\varphi}{\cosh\gamma-\cos\eta}\right)^2+\left(\frac{a\sin\eta\sin\varphi}{\cosh\gamma-\cos\eta}\right)^2+\left(\frac{a\sinh\gamma}{\cosh\gamma-\cos\eta}\right)^2$$
$$a^2\cosh^2\gamma=x^2+y^2+(z-a\coth\gamma)^2. \tag{A.4}$$

Eq. A.4 is an equation of spherical surface with radius $a\cosh\gamma$ centered at $(0,0,a\coth\gamma)$. Thus, $\gamma=$ constant is the spherical surface.

A.1 Scale factors and unit vectors

The scale factors are given by

$$h_\gamma=h_\eta=\frac{a}{\cosh(\gamma)-\cos(\eta)},\qquad h_\varphi=\frac{a\sin(\eta)}{\cosh(\gamma)-\cos(\eta)}, \tag{A.5}$$

and the unit vectors of each component in terms of unit vectors of Cartesian coordinates are given by

$$\hat{e}_\gamma=\frac{1}{\cosh\gamma-\cos\eta}[-\sinh\gamma\sin\eta(\cos\varphi\hat{i}+\sin\varphi\hat{j})+(1-\cosh\gamma\cos\eta)\hat{k}], \tag{A.6}$$
$$\hat{e}_\eta=\frac{1}{\cosh\gamma-\cos\eta}[(\cosh\gamma\cos\eta-1)(\cos\varphi\hat{i}+\sin\varphi\hat{j})+\sinh\gamma\sin\eta\hat{k}], \tag{A.7}$$
$$\hat{e}_\varphi=-\sin\varphi\hat{i}+\cos\varphi\hat{j}. \tag{A.8}$$

A.2 Laplacian and separation of variables

The Laplacian in general curvilinear coordinate system is defined by

$$\nabla^2=\frac{1}{h_1h_2h_3}\left\{\frac{\partial}{\partial q_1}\frac{h_2h_3}{h_1}\frac{\partial}{\partial q_1}+\frac{\partial}{\partial q_2}\frac{h_3h_1}{h_2}\frac{\partial}{\partial q_2}+\frac{\partial}{\partial q_3}\frac{h_1h_2}{h_3}\frac{\partial}{\partial q_3}\right\}. \tag{A.9}$$

Thus, by substituting the expressions A.5, the Laplacian becomes

$$\nabla^2=\frac{(\cosh\gamma-\cos\eta)^3}{a^2\sin\eta}\left\{\sin\eta\left(\frac{\partial}{\partial\gamma}\frac{1}{\cosh\gamma-\cos\eta}\frac{\partial}{\partial\gamma}\right)+\left(\frac{\partial}{\partial\eta}\frac{\sin\eta}{\cosh\gamma-\cos\eta}\frac{\partial}{\partial\eta}\right)\right\}$$
$$+\frac{(\cosh\gamma-\cos\eta)^2}{a^2\sin^2\eta}\frac{\partial^2}{\partial\varphi^2}. \tag{A.10}$$

The solution of Laplace equation $\nabla^2\Psi(\gamma,\eta,\varphi)=0$ can be achieved by separation of variables technique by setting

$$\Psi(\gamma,\eta,\varphi)=\sqrt{\cosh(\gamma)-\cos(\eta)}\Gamma(\gamma)\Pi(\eta)\Phi(\varphi) \tag{A.11}$$

A.3 System parameter

Two spherical surfaces can be specified by two surfaces of constant γ_1 and $-\gamma_2$ such that

$$\frac{a}{\sinh\gamma_1} = R_1, \tag{A.12}$$

$$\frac{a}{\sinh\gamma_2} = R_2, \tag{A.13}$$

$$a\coth\gamma_1 + a\coth\gamma_2 = h. \tag{A.14}$$

We need to solve A.12-A.14 to get γ_1 and γ_2. From A.12 and A.13, we have

$$\sinh\gamma_1 = \frac{a}{R_1} \quad \Rightarrow \quad \cosh\gamma_1 = \sqrt{1+\frac{a^2}{R_1^2}}, \tag{A.15}$$

$$\sinh\gamma_2 = \frac{a}{R_2} \quad \Rightarrow \quad \cosh\gamma_2 = \sqrt{1+\frac{a^2}{R_2^2}}. \tag{A.16}$$

Substituting A.15 and A.16 we obtain

$$a = \left\{\frac{[h^2-(R_1+R_2)^2][h^2-(R_1-R_2)^2]}{4h^2}\right\}^{1/2}. \tag{A.17}$$

Appendix B

Useful recursion relation of Legendre polynomials

From the boundary condition Eq. 4.9, we read

$$a_{nm} = c_{nm}^{(1)} + d_{nm}^{(1)}, \tag{B.1}$$

$$\text{and} \qquad b_{nm} = c_{nm}^{(2)} + d_{nm}^{(2)}, \tag{B.2}$$

where $a_{nm} = A_{nm}e^{-(n+\frac{1}{2})\gamma_1}$ and $b_{nm} = B_{nm}e^{-(n+\frac{1}{2})\gamma_2}$. $c_{nm}^{(1)}$, $d_{nm}^{(1)}$, $c_{nm}^{(2)}$, $d_{nm}^{(2)}$ are defined in Eq. 4.13 - Eq. 4.16. The boundary conditions Eq. 4.10 yield

$$\begin{aligned}\varepsilon_1 \Sigma P_n^m(\cos\eta)e^{im\phi}\left[\sinh\gamma_1(2n+1)(\cosh\gamma_1-\cos\eta)\right]a_{nm} \\ = \varepsilon_0 \Sigma P_n^m(\cos\eta)e^{im\phi}\left[\left(\sinh\gamma_1+(2n+1)(\cosh\gamma_1-\cos\eta)\right)c_{nm}^{(1)}\right. \\ \left.+\left(\sinh\gamma_1(2n+1)(\cosh\gamma_1-\cos\eta)\right)d_{nm}^{(1)}\right],\end{aligned} \tag{B.3}$$

and

$$\begin{aligned}\varepsilon_2 \Sigma P_n^m(\cos\eta)e^{im\phi}\left[\sinh\gamma_2(2n+1)(\cosh\gamma_2-\cos\eta)\right]a_{nm} \\ = \varepsilon_0 \Sigma P_n^m(\cos\eta)e^{im\phi}\left[\left(\sinh\gamma_2-(2n+1)(\cosh\gamma_2-\cos\eta)\right)c_{nm}^{(2)}\right. \\ \left.+\left(\sinh\gamma_1+(2n+1)(\cosh\gamma_1-\cos\eta)\right)d_{nm}^{(2)}\right],\end{aligned} \tag{B.4}$$

The terms on the left hand side of Eq. B.3 and Eq. B.4 are in the form (for a given m)

$$\sum_n P_n^m(x)\left[f(n,m)+(2n+1)xg(n,m)\right]\alpha_{nm}. \tag{B.5}$$

By applying the recursion relation of associated Legendre polynomial [80],

$$(2n+1)xP_n^m(x) = (n-m+1)P_{n+1}^m(x) + (n+m)P_{n-1}^m(x). \tag{B.6}$$

to the expression B.5, it can be proven that

$$\begin{aligned}&\sum_n P_n^m(x)\left[f(n,m)+(2n+1)xg(n,m)\right]\alpha_{nm} \\ &= \sum_n P_n^m(x)\left[f(n,m)\alpha_{nm}+(n-m)g(n-1,m)\alpha_{n-1m}+(n+m+1)g(n+1,m)\alpha_{n+1m}\right].\end{aligned} \tag{B.7}$$

Applying B.7 to B.3 and B.4 results in Eq. 4.11 and 4.12.

Appendix C

Nonlinear eigenvalue problem: a brief introduction

The nonlinear eigenvalue problem (NLEVP) is the problem of solving for a pair of scalars λ and nonzero vectors $\mathbf{u}$ and $\mathbf{v}$ satisfying

$$F(\lambda)\mathbf{u} = 0, \tag{C.1a}$$

$$\mathbf{v}^\dagger F(\lambda) = 0, \tag{C.1b}$$

where F: $\mathbb{C} \to \mathbb{C}^{m\times n}$ defined by

$$F(\lambda) = \sum_{i=0}^{k} f_i(\lambda)\mathbf{A}_i, \tag{C.2}$$

where f: $\mathbb{C} \to \mathbb{C}$ and $\mathbf{A}_i \in \mathbb{C}^{m\times n}$. λ, $\mathbf{u}$ and $\mathbf{v}$ obeying Eq. C.1 are called eigenvalue, right eigenvector and left eigenvector, respectively. Eq. C.1a can be rewritten in the form

$$P(\lambda)\mathbf{u} = 0, \tag{C.3}$$

where

$$P(\lambda) = \sum_{i=0}^{k} \lambda^i \mathbf{A}_i, \tag{C.4}$$

which is called *polynomial eigenvalue problem* (PEP). Note that this also hold for Eq. C.1b. In the special cases such as

(i) $k = 1$, $\mathbf{A_0} = \mathbf{A}$ and $\mathbf{A_1} = -\mathbf{I}$, the PEP reduces to, the most familiar problem in physics, the standard eigenvalue problem is given by

$$\mathbf{A}\cdot\mathbf{u} = \lambda\mathbf{u}, \tag{C.5}$$

(ii) $k = 1$, $\mathbf{A_0} = \mathbf{A}$ and $\mathbf{A_1} = \mathbf{B} \neq \mathbf{I}$, Eq. C.3 reduces to

$$\mathbf{A}\cdot\mathbf{u} = \lambda\mathbf{B}\cdot\mathbf{u}, \tag{C.6}$$

which is termed *generalized eigenvalue problem* (GEP),

(iii) $k = 2$, all $\mathbf{A_0}$, $\mathbf{A_1}$, and $\mathbf{A_2}$ are nonzero matrices, Eq. C.3 is in the quadratic form

$$Q(\lambda)\mathbf{u} = (\lambda^2\mathbf{A_2} + \lambda\mathbf{A_1} + \mathbf{A_0}) \cdot \mathbf{u} = 0, \tag{C.7}$$

which is called *quadratic eigenvalue problem* (QEP). Here, we only give a brief introduction to the NELPV. The details of classification of NELVP, the collection of the problems, and the numerical techniques are provided in Ref.[84, 85, 86, 87, 88, 89, 90, 91, 92, 93, 94].

VITAE

Mr. Rakchat Klinkla was born on 9 March 1980. He received his Bachelor's degree (with second class honours) in physics (B.Sc. physics) from Ubon Ratchathani Rajabhat University in 2003. His senior project in B.Sc. is on the Aharonov Bohm effect on interference pattern of double slit electron diffraction experiment using the Feynman path integral approach. Afterwards, he worked as a physics teacher at Phuhungphatthanawit High school in Kalasin province, thailand. Then he continued his study for his Degree of Doctor at Chulalongkorn University in 2006.

Journal Publication:

1. R. Klinkla, Sutee Boonchui and U. Pinsook. Role of symmetry in coupled localized surface plasmon resonance of a nanosphere pair. Submitted.

Conference Presentations:

1. R. Klinkla, and U. Pinsook. (13-15 December 2010).Surface plasmon oscillations in a cluster of two different metallic nanospheres. The 6^{th} Siam Physics Congress 2011. Chonburi, Thailand (21-23 Oct 2013)
2. R. Klinkla, and U. Pinsook. (23-26 March 2011). Van der Waals Interaction between Two Spherical Nanoclusters. The 6^{th} Mathematics and Physical Sciences Grauate Congress 2010. University of Malaya, Malasia.